**Naval Research Laboratory**

Washington, DC 20375-5000

NRL Memorandum Report 6098

# Models for Electromagnetic Scattering from the Sea at Extremely Low Grazing Angles

L. B. WETZEL

*Senior Scientist and Propagation Staff*
*Radar Division*



December 31, 1987

SECURITY CLASSIFICATION OF THIS PAGE

## REPORT DOCUMENTATION PAGE

Form Approved
OMB No 0704-0188

AD-A190 472

| | |
|---|---|
| 1a REPORT SECURITY CLASSIFICATION<br>UNCLASSIFIED | 1b RESTRICTIVE MARKINGS |
| 2a SECURITY CLASSIFICATION AUTHORITY | 3 DISTRIBUTION/AVAILABILITY OF REPORT<br>Approved for public release; distribution unlimited. |
| 2b DECLASSIFICATION/DOWNGRADING SCHEDULE | |
| 4 PERFORMING ORGANIZATION REPORT NUMBER(S)<br>NRL Memorandum Report 6098 | 5 MONITORING ORGANIZATION REPORT NUMBER(S) |
| 6a NAME OF PERFORMING ORGANIZATION<br>Naval Research Laboratory<br>6b OFFICE SYMBOL (If applicable)<br>Code 5303 | 7a NAME OF MONITORING ORGANIZATION<br>Office of Naval Research |
| 6c ADDRESS (City, State, and ZIP Code)<br>Washington, DC 20375-5000 | 7b ADDRESS (City, State, and ZIP Code)<br>Arlington, VA 22217 |
| 8a NAME OF FUNDING/SPONSORING ORGANIZATION<br>Office of Naval Research<br>8b OFFICE SYMBOL (If applicable)<br>ONR | 9 PROCUREMENT INSTRUMENT IDENTIFICATION NUMBER |
| 8c ADDRESS (City, State, and ZIP Code)<br>Arlington, VA 22217 | 10 SOURCE OF FUNDING NUMBERS<br>PROGRAM ELEMENT NO: 61153N; PROJECT NO: RR021-05-43; TASK NO: ; WORK UNIT ACCESSION NO: DN280-045 |

11 TITLE (Include Security Classification)
Models for Electromagnetic Scattering from the Sea at Extremely Low Grazing Angles

12 PERSONAL AUTHOR(S)
Wetzel, Lewis B.

| 13a TYPE OF REPORT | 13b TIME COVERED | 14 DATE OF REPORT (Year, Month, Day) | 15 PAGE COUNT |
|---|---|---|---|
| Interim | FROM _____ TO _____ | 1987 December 31 | 83 |

16 SUPPLEMENTARY NOTATION

| 17 COSATI CODES | | | 18 SUBJECT TERMS (Continue on reverse if necessary and identify by block number) | | |
|---|---|---|---|---|---|
| FIELD | GROUP | SUB-GROUP | Sea scatter | Low angle clutter | Shadowing |
| | | | Rough surface | Scatter | Radar clutter |
| | | | Sea spikes | | |

19 ABSTRACT (Continue on reverse if necessary and identify by block number)

The present state of understanding in the field of low-grazing-angle sea scatter is reviewed and extended. The important concept of shadowing is approached from the point of view of diffraction theory, and limits in wind speed and radar frequency are found for the application of shadowing theories based on geometrical optics. The implications of a shadowing function based on "illumination thresholding" are shown to compare favorably with a variety of experimental results. Scattering from the exposed surface peaks is treated by a composite-surface Bragg model, and by wedge models using both physical optics and the method of equivalent currents. Curiously, the scattering levels predicted by these widely different approximations are all in fairly good agreement with experimental values for moderately low grazing angles (about 5°), with the physical optics wedge model being superior at 1°. A new scattering feature, the "slosh," is introduced, with scattering behavior that resembles the temporal and polarization dependence of observed low angle returns from "calm"

(Continues)

| 20 DISTRIBUTION/AVAILABILITY OF ABSTRACT | 21 ABSTRACT SECURITY CLASSIFICATION |
|---|---|
| ☒ UNCLASSIFIED/UNLIMITED ☐ SAME AS RPT ☐ DTIC USERS | UNCLASSIFIED |
| 22a NAME OF RESPONSIBLE INDIVIDUAL<br>Lewis B. Wetzel | 22b TELEPHONE (Include Area Code)<br>(202) 767-3417 |
| | 22c OFFICE SYMBOL<br>Code 5303 |

DD Form 1473, JUN 86 Previous editions are obsolete SECURITY CLASSIFICATION OF THIS PAGE

S/N 0102-LF-014-6603

19. ABSTRACT (Continued)

water. The "plume" model of scattering from breaking waves (from earlier work) is discussed as a source of high-intensity Sea Spikes. It is emphasized that the prediction of low angle scattering from the sea will require considerably more information about the shape, size, and distribution of the actual scattering features.

| Accession For | |
|---|---|
| NTIS GRA&I | ☒ |
| DTIC TAB | ☐ |
| Unannounced | ☐ |
| Justification | |
| By | |
| Distribution/ | |
| Availability Codes | |
| Dist | Avail and/or Special |
| A-1 | |



DD Form 1473, JUN 86

## CONTENTS

# MODELS FOR ELECTROMAGNETIC SCATTERING FROM THE SEA AT EXTREMELY LOW GRAZING ANGLES

## I. INTRODUCTION

Navy radars operating from ships, shore installations, and low-flying aircraft inevitably view the sea at extremely low grazing angles ($< 1°$). Under these conditions one might expect the surface to be deeply shadowed, yet the experimental evidence is unclear, sometimes even contradictory. It is obvious that this is a very special scattering regime, in which our normal ideas of sea scatter are quite possibly of little use. Our approach to understanding this regime will be guided by two basic questions:

1. How much, and what part, of the sea surface is actually illuminated and observed simultaneously in a scattering interaction?

2. What are the special structural characteristics of the scattering elements in such regions, and what theoretical models are to be used.

Attempts to answer these questions run into severe problems in conceptualization (visualizing the physical processes involved), and modeling (finding useful predictive analytical descriptions of these processes.) While shadowing of some sort must certainly take place at extreme grazing angles, radars operate at finite wavelengths, so the effects of diffraction cannot be ignored. Unfortunately, a diffraction-corrected shadowing theory does not exist, and the task of constructing one appears formidable. The modulation of the surface illumination by shadowing will preferentially highlight special regions of the surface - the raised wave peaks - whose morphology cannot be described with any confidence, and whose scattering properties are largely unexplored and imperfectly understood. In this area, modeling consists mainly of analogical guesswork and uncritical application of models that appear to work in other angular regimes.

The purpose of this report will be to define these problems with greater precision, see how far existing knowledge can carry us, develop some new models and new approaches, and identify those topics requiring further work.

## II. SHADOWING

There are two ways to approach the problem of surface illumination at low angles: as a diffraction problem for which the usual geometrical optics shadowing theory is considered a limiting case, or as a statistical exercise in geometrical optics in which there might be need for some diffraction corrections. It is the second approach that has attracted all the attention [Bass and Fuks, 1963; Beckmann, 1965; Wagner, 1967; Smith, 1967; Sancer, 1969; Lynch and Wagner,1970; etc.). The reason, of course, is because it is doable, albeit under certain severe assumptions: two-dimensional geometry, uncorrelated Gaussian surface, geometrical optics transition across the shadow line. Many useful statistical expressions are derived during the course of these treatments, but the end result is usually a

Manuscript approved August 27, 1987.

"Shadowing Function," which is essentially the percentage of surface area, on the average, that will be illuminated at a given grazing angle, and for small angles is just a linear function of the angle. It is this crude shadowing function that is invoked whenever a shadowing theory is called for, yet there is little evidence that these results are of any value when applied to a real sea at low grazing angles.

At extreme grazing angles the standard geometrical shadowing theory referred to above develops some interesting implications, which were explored heuristically by Wetzel [1977]. It was found that at grazing angles below about 1 degree, the sea should begin to resemble a "dark" plane, populated by illuminated "islands," whose size and spacing are determined by the mean grazing angle and the wind speed. This conceptual model has a strong intuitive appeal, and bears a closer relation to visual observation and radar events such as "sea spikes" than does the diffuse "vanishing scatter" picture suggested by the "shadowing function." Nevertheless, this is still a geometrical theory, and we must take a close look at the diffraction problem in order to find when, if ever, such models may be used.

## A. Diffraction Effects at Wave Peaks

The simplest surface model for encorporating diffraction effects into sea scatter is one containing two sharp peaks separated by a broad smooth trough. The cycloid provides such a curve, and is often related to the shape of ocean waves both formally [Kinsman,1965], and informally [ask anyone to sketch an "ocean wave"]. It is given by the parametric equations:

$$x = x' - a \sin(Kx') \tag{1}$$

$$z = z' + a \cos(Kx')$$

where $a$ controls the shape of the curve ($a = 1$ gives peaks with sharp points, while $a < 1$ gives rounded peaks.) In Fig. 1 we show the case for $a = 1$ (trochoid), with the shadow line indicated for illumination at a grazing angle $\psi$. The axes are normalized so that the abscissa is given in fractions of a wavelength (distance between peaks), $s = x/\Lambda$, while the ordinate is the fraction of the peak-to-trough wave height H. We should note that Fig. 1 represents a two-dimensional model in which the wave crests are infinitely long in the direction perpendicular to the paper. Such models can therefore be applied only in situations where the sea actually is long-crested, and the illumination is normal to the crests. Unfortunately, these conditions are seldom encountered. Real wind-driven seas tend to be relatively short-crested, with the water piled in heaps. Whether a real surface can be modeled in any practical way is open to question, although we will make a few comments about this problem a little later. For now, we continue to seek insight into the shadowing problem from the simple two-dimensional model, in which we will find enough to occupy our attention.

Under the assumptions of geometrical optics, the wave surface would be fully illuminated to the right of the intersection of the shadow line with the surface, and totally dark to the left. The effect of diffraction in smoothing this transition may be approached as follows.

### *1. Physical Optics*

Imagine a vertical plane erected perpendicular to the wave peak at the point of tangency with the shadow line. The field to the right of the plane is found from the Helmholtz integral over the plane using the field values appropriate to the unperturbed incident wave. The result is the familiar Fresnel diffraction pattern for a straightedge, and it is independent of the actual shape of the diffracting wave peak. That is, the physical optics expression for the field in the region between the peaks in Fig. 1 is given in normalized form by

$$E_{PO}(R,\theta) = |F(w) - F(-\infty)|/\sqrt{2} \tag{2}$$

where $F(w)$ is the Fresnel integral

$$F(w) = \int_0^w e^{i\frac{\pi}{2}u^2} du; \quad w = \sqrt{kR/\pi\theta} \tag{3}$$

and $\theta$ is the angle relative to the shadow line (negative below, positive above).

This is the simplest approximation to diffraction effects, yet it quite dramatically illustrates the importance of including such effects in scattering calculations. In Fig. 2 we have plotted the illumination field intensity ( $|E|^2$) over the trochoidal surface of Fig. 1 as derived from Eqns. (2) and (3) for a 3 cm. wavelength (X-band), a 3° grazing angle, and a 15 knot wind speed. (In this, and the following examples, peak wave height is taken as $H = .015W^2$(m) and $L = .64W^2$(m) is the surface "wavelength," where W is in m/sec.) Since the shadow line for a 3° grazing angle encounters the trochoidal surface at 0.47, the corresponding geometrical optics illumination profile is shown as a vertical line at that point, separating light (intensity = 1, to the right) from dark (intensity = 0, to the left). For the Fresnel diffraction pattern, the diffracted field is always equal to 0.5 at the shadow line, so the relative intensity at that point is always 0.25. The gradual transition from light to shadow produced by diffraction can be characterized by a "transition fraction," F, defined by the interval along the trough over which the field changes from 0 to 1 by the steepest tangent to the diffraction curve. This is illustrated in Fig. 2. It is of interest to note that in this example, F is measured between the intersection of the shadow line with the trough, at s = 0.47, and the point at which the diffraction profile crosses 1. This seems generally to be the case.

*2. Polarization Effects*

Scattering from the sea often shows strong polarization effects, and we should be concerned whether the shadowing and diffraction processes we have been discussing display any polarization dependence. In the trochoidal model we are using to investigate shadowing and diffraction, the wave peak itself is essentially a knife-edge (examine the implications of Eqn.(1) at $x' = 0$), so since we have already used the physical optics solution to find the diffracted field, it is an easy matter to append to this solution the so-called "edge waves" of Ufimtsev's Physical Theory of Diffraction [1957]. In this theory, the Physical Optics field given by Eqns. (2) and (3) is "corrected" by adding an "edge wave" field:

$$E_{EW} = \frac{e^{i(kR + \pi/4)}}{\sqrt{2\pi kR}} D_{V,H}(\theta_1, \theta_0) \tag{4}$$

$$D_{V,H} = -0.5\{[1 - \sin((\theta - \theta_0)/2)]/\cos((\theta - \theta_0)/2)$$

$$+ P^*[1 - \sin((\theta + \theta_0)/2]/\cos((\theta + \theta_0)/2)\}$$

where $\theta_0$ and $\theta$ are respectively the incident and scattering angles relative to the front face of the wave peak, and $P = +1$ for vertical, $P = -1$ for horizontal polarization. It turns out that in the low grazing angle, forward scatter case, the coefficient D is of order unity for both polarizations (although of opposite sign.) Thus the importance of polarization effects is determined entirely by the magnitude of the cylindrical spreading factor in the first equation above. In virtually all cases of any practical interest, this factor is sufficiently small over the entire wave trough that we may ignore polarization effects in diffraction by wave peaks. These effects can be seen only at long illuminating wavelengths, at low wind speeds, and close behind the diffracting peak.

For the skeptic, we show in Fig. 3 the full diffracted field, obtained from Eqns. (2), (3) and (4) for L-band illumination (30cm), horizontal polarization (vertical looks the same, only the peaks and valleys are exchanged), a grazing angle of 3° and wind speeds of 5, 15 and 25 knots. Clearly, the polarization-dependent wiggles seen in the 5 kt curve (which are due to the exponential phase term in Eqn. (4)) vanish at the higher wind speeds. However, we will find below that the 5kt curve lies outside the limits of validity of Physical Optics, so we conclude that to the extent that edge-based diffraction theory is valid, polarization effects are unimportant.

If we had chosen a different surface model, say the cycloid of equations (1) with $a < 1$ so the peak would be rounded instead of sharp, then the polarization correction would take the form given by Wait and Conda [1959] for the field behind an obstacle with a rounded edge having a radius of curvature r:

$$E_{WC} = \frac{(kr/2)^{1/3}}{\sqrt{kR/2}} G_{V,H}\left((kr/2)^{1/3}\theta\right) \tag{5}$$

where the function $G_{V,H}$ is an integral over Airy functions and is given in graphical form. Its amplitude ranges between 0 and 1. For broad smooth peaks, this correction could be considerably larger than the sharp-peak correction given in Eqn.(4), but for curvatures of the order of a few wavelengths we may ignore these corrections as well.

In summary, then, polarization will give at most small corrections to the diffracted field, and thus may safely be ignored when estimating the effects of diffraction on shadowing.

*3. When Can Geometrical Optics Be Used?*

Figures 2 and 3 show how diffraction spreads the illumination field over the trough region behind the wave peaks. If the "transition fraction" F, defined in section II.A.1, were to be zero, then geometrical optics would apply exactly. It can never be zero, of course, but if it were sufficiently small, we might expect geometrical optics to provide a reasonable model for estimating shadowing effects at low grazing angles. The criterion for "sufficiently small" must be arbitrary, but most would agree that values of $F<0.1$ would provide a transition approaching optics-like sharpness, while for values of $F>0.3$ the illumination profile is clearly controlled by diffraction. The basic data to which these criteria are to be applied may be found in Figs. 4a-4t, where we have plotted the diffracted field intensity profiles from (2) for five grazing angles for each of five wavelengths and four wind speeds.

It is clear in Figs.4 that for a given wavelength and wind speed, the shapes of the diffraction profiles, hence the fractions F, are relatively insensitive to the grazing angle. Thus we may plot lines of equal F against wavelength/windspeed axes and thereby roughly separate the regions defined by the criteria discussed above. The results are shown in Fig. 5, where the labels "YES," "MAYBE," and "NO" are used to indicate the confidence to be placed in the use of the geometrical optics assumption in various domains of the wavelength/windspeed plane. As might be expected, the most popular radar wavelength (3cm), at the mean global windspeed (15kts), falls squarely in the middle of the ambiguous "MAYBE" domain. Nevertheless, this figure gives some useful perspective when trying to decide how seriously to take the predictions of shadowing theories.

The "YES" domain in Fig. 5 is disappointingly small, indicating that for the most popular radar frequencies, geometrical optics provides a good approximation to the illumination profile only in the presence of gale force winds. We might expect geometrical optics to provide at least some useful trends for points in the "MAYBE" domain, but a good part of microwave radar operations in the Navy takes place in the "NO" domain, where diffraction dominates and no satisfactory theory exists.

*4. Limitations and Extensions of Diffraction Theory*

We must not be misled into believing that the diffraction curves for the longer wavelengths and lower windspeeds and grazing angles are to be taken seriously. Consider the dimensions of the surface features associated with a windspeed of 5 kts. The peak-to-trough height for our trochoidal model would be about 10cm, so the distance of the diffracting peak above the trough is one wavelength at 10cm (S-band), 1/3 wavelength at 30cm (L-band), and 1/10 wavelength at 100cm (UHF). The Physical Optics approximation underlying the diffraction theory expressed in Eqns.(2) and (3) can not be expected to be valid under these conditions - in fact, for the extreme UHF case, the Rayleigh perturbation theory would seem more appropriate. This validity limit is expressed in Fig.5 by the dashed curve labeled "Physical Optics Limit," which corresponds to wind speeds for which the radar wavelength is just equal to the peak-to-trough wave height. Looking back at the calculated diffraction profiles in Fig. 4, we see that Figs. 4i,m,n,q,r,s lie at or below this limit - which is comforting, since these illumination profiles certainly defy credibility.

Although we are most interested in the range of extremely small grazing angles, between 0 and 1 degree, it is in this range that diffraction theory seems least informative. About all that can be said from examining this angular regime for the legitimate examples in Figs. 4, is that at very low grazing angles the illumination in most of the trough will always be low, and will rise fairly sharply close to the opposite peak. In a real sea, the second peak would be higher or lower than the first, and the trough length between peaks would be different for different pairs, leading to fluctuations in the illumination intensity at the peak which would be described by some statistical distribution of sea surface parameters. But there is no statistical theory of diffraction for a rough sea, so if we wish to treat the real sea in any sense at all, we will have to trade the deterministic clarity of classical diffraction theory for the ambiguity and limited applicability of conventional, geometrical optical, shadowing theory. However, before leaving diffraction theory, let us take a quick look at a particular statistical extension of the standard diffraction problem that can add a bit of three-dimensional realism.

When we introduced the trochoidal wave model at the beginning of this section, we noted that it was a two-dimensional model, appropriate only to infinitely long-crested waves. However, in connection with the problem of radio propagation over hills and ridges, Furutsu [1965] considered the case in which the ridges contained statistical height variations along their crests. A sketch of such a ridge is shown in Fig. 6, where R is the distance behind the ridge, H is its mean height, and $\psi$ is the grazing angle of the incident wave. The irregular crest height has a Gaussian distribution with variance $< |h^2| >$, and an arbitrary correlation function. We won't go into the details of the analysis other than to remark that the basic theoretical assumption is that the physical optics integration plane can be divided into narrow strips of width $dy$ above the crest height $h(y)$, and the integral done as usual over the $y-z$ plane above the crest. Certainly the irregular structure in Fig. 6 is a better model of a shadowing wave crest than the infinite two-dimensional model we used earlier.

Here, as in most propagation problems involving irregularities, the "Fresnel length," $l_F = (\lambda R)^{1/2}$, can be expected to play a role. In Fig. 6, we have added the first Fresnel Zone at the diffracting obstacle as seen looking back from the observation point. The effects of fluctuations in crest height at the tangent point, and statistical variations in crest height along the crest, can both be discussed in terms of their relation to the Fresnel length (or radius of the first Fresnel zone). If we let $h_0$ be the rms height fluctuation about the mean height H, and $l_c$ the correlation length of the height variations along the crest, then we would expect the diffraction patterns to look much like those for a fixed, infinite crest provided

$$h_0 << l_F \text{ and } l_c >> l_F . \tag{6}$$

Otherwise, surface statistics can have a significant effect on the diffraction pattern. Consider, for example, the illumination of the forward face of the right-hand crest in Fig.1. In this case R will be the wavelength of the longest waves on a wind-driven sea, namely $R=0.64W^2$. The Fresnel lengths $l_F$ (in meters) as seen looking back to the left hand, diffracting, crest for our five radar wavelengths (in cm.) are given in the table below:

Fresnel Lengths versus wavelength and wind speed

| Wavelength = | 1 cm | 3 cm | 10 cm | 30 cm | 100 cm | H/2 (m) |
|---|---|---|---|---|---|---|
| 5 kts | .2 | .4 | .6 | 1.1 | 2 | .05 |
| 15 kts | .6 | 1.0 | 1.9 | 3.3 | 6 | .45 |
| 25 kts | 1 | 1.7 | 3.2 | 5.5 | 10 | 1.25 |

The last column is 1/2 the peak-to-trough wave height for the indicated wind speed, and gives a measure of the maximum rms crest height fluctuation $h_0$ that could occur. We see that the first condition given in Eqn. (6) is pretty well satisfied for all frequencies above K-band (1 cm). On the other hand, if seas are usually short crested and "piled in heaps," we would expect the second condition to be satisfied primarily at the shorter radar wavelengths, and for intermediate seas. From these considerations, then, it is possible to conclude that there is at least a small range of frequencies and wind speeds, centered about the X and S bands for about 15 knots of wind, in which deterministic diffraction theory based on the average wave heights should provide a reasonable estimate of surface illumination.

For readers curious about the effect of crest fluctuations on diffraction patterns, we include in Fig. 7 a plot from the paper by Furutsu [loc.cit.]. Clearly, our simple Fresnel-length arguments describe the situation quite well.

### B. Some Basic Shadowing Probabilities

Associated with the illumination and observation of points on a surface, there are several probabilities that can be discussed without reference to the details of any particular shadowing theory. In Fig. 8 we consider the most general case of bistatic scattering from an element of the surface. The plane of incidence contains the illumination path at grazing angle $\psi_I$, while observation takes place at grazing angle $\psi_O$ in the plane of observation, which is rotated from the plane of incidence through the azimuthal angle $\phi_O$. These planes intersect at a point P on the surface, whose scattering properties are left unspecified.

Monostatic backscatter is defined by setting $\psi_O = \psi_I$, and $\phi_O = \pi$; bistatic scattering takes place for any other values of $\psi_O$ and $\phi_O$. The several probabilities associated with the shadowing process may be related symbolically as follows:

$$P(I, O) = P(I)P(I \mid O) \tag{7}$$

where P(I,O) is the joint probability that the surface element is both Illuminated (I) and Observed (O), P(I) is the probability that the element is illuminated, and P(I | O) is the conditional probability that if illuminated, the element is also observed. In the monostatic case, illumination and observation take place over the same path, so *if* I, then O, and P(I | O) = 1. Thus we may write

$$\text{Monostatic Case:} \quad P_M(I, O) = P(I) \tag{8}$$

The bistatic case contains several possibilities. For example, if $\psi_O > \psi_I$ with $\phi_O = \pi$ (observation over the same surface as illumination, but at a greater angle), then once again P(I | O) = 1, since if the incident ray has escaped encounter with the surface peaks, then *certainly* a ray at a higher angle has escaped. In this case the bistatic P(I,O) is the same as the monostatic. If the observation angle $\psi_O < \psi_I$, then we simply exchange I and O and obtain P(I,O) = P(O) by the same reasoning; that is, the joint probability is always the single-path probability for the path with the smallest grazing angle.

However, when $\phi_0 \neq \pi$, the illumination and observation paths lie over different regions of the sea surface, and to the extent that the surface features in these regions are uncorrelated, the conditional probability P(I | O) is *independent* of the path I and simply equal to P(O), the probability of observing the element of interest. Under most sea conditions correlation distances for the larger-scale surface features responsible for shadowing are of the order of the primary sea wavelength, so decorrelation will be the rule, and we can be confident in writing for the

Bistatic Case:

$$P_B(I,O) = P(I)P(O), \quad \phi_O \neq \pi \tag{9a}$$

$$P_B(I,O) = P(I) \qquad \phi_O = \pi, \ \psi_O > \psi_I \tag{9b}$$

$$P_B(I,O) = P(O) \qquad , \quad \phi_O = \pi, \ \psi_O < \psi_I \tag{9c}$$

It should be noted that the first expression applies to the special case of forward scatter in the specular direction: $\phi_0 = 0$, $\psi_O = \psi_I$.

The purpose of a shadowing theory is to give analytical expression to the basic path probability P( ) in terms of grazing angle and surface parameters. These probabilities are then used in the relations given above.

## C. Shadowing Theory Based on Geometrical Optics

Although Fig. 5 shows the domain of confidence in geometrical optics to be rather small, all existing theories of shadowing are based on this assumption, so we must seek what guidance we can from the body of existing work. The assumption appears in slightly different forms in the various treatments. If the theory is developed from a Physical Optics scattering integral, as in Bass and Fuks or Sancer [*loci cit*], then the integrand will contain an "illumination factor," I(*r*), which is unity if *r* is illuminated, zero if it is not. The purely statistical treatments by Smith or Wagner [*loci cit*] directly calculate P(z,s), "the probability that an element of surface at height z with slope s is not shadowed by the intervening surface along the incident ray," and then integrate it in various ways to find the "shadowing function" mentioned at the beginning of this Section. Multivariate statistics and correlation functions are sometimes brought in to provide an aura of generality, but they are never really taken seriously, and in the end the problem is simplified to one in which the surface heights and slopes are uncorrelated, and have independent Gaussian distributions. Under these conditions, the Probability of Illumination P(I) (refer to Eqn. (7)) of a surface element at height *z* and slope s, on a Gaussian surface of rms displacement $\sigma$ and mean slope $s_0$, when viewed at a mean grazing angle $\psi$ (relative to the horizontal), is given by [see Smith, *loc cit*]:

$$P(I) = P(\eta; \xi, q) = (1 - .5\,erfc\,(\xi))^{\Lambda(\eta)}\, U(q + \psi) \tag{10}$$

where

$$\Lambda(\eta) = \frac{1}{2}\left[\left(\frac{2}{\pi}\right)^{1/2}\frac{e^{-\eta^2/2}}{\eta} - erfc(\eta)\right] \tag{11}$$

with the definitions $\eta = \psi/s_0$, $\xi = z/\sqrt{2}\sigma$, q=arctan(s), and U(x)=unit step function, which is simply a *local* shadowing function (i.e., it ensures that an element on the back side of a wave peak will not be illuminated.) These expressions can be further simplified by taking into account the special conditions encountered over the sea: namely, the mean slope, $s_0$, of the sea surface is about 0.1, and the grazing angles of major interest here will generally be less than 1°. Under these conditions, $\eta < 0.17$, so the complicated function (11) can be approximated in the simple form:

$$\Lambda(\eta) \approx \frac{1}{2}\left[\frac{0.8}{\eta} - 1\right]. \tag{11'}$$

The illumination probability given in (10) is based on a one-dimensional Gaussian process, but bistatic scattering generally takes place in a two-dimensional geometry, so that two-dimensional aspects of the surface must be taken into account. Illumination and observation take place in two vertical planes intersecting the surface at the common point P, thereby defining two local slopes, $q_I$ and $q_O$. The joint probability in (9a) is thus written as the product of two expressions of the form of (10), each containing the angles appropriate to its plane of definition. That is,

$$P_B(I, O) = (1 - .5\ erfc\ (\xi))^{\Lambda(\eta_I)+\Lambda(\eta_O)} U(q_I + \psi_I)\, U(q_O + \psi_O) \tag{12}$$

*1. The Threshold Model*

In order to get a clearer idea of the implications of these expressions, let us consider first the behavior of the factor in (10) that depends only on surface height and mean grazing angle:

$$P^0(I) = (1 - .5\ erfc\ (\xi))^{\Lambda(\eta_I)} \tag{13}$$

This expression is easily calculated, and is shown in Fig. 9 for values of $\eta$ between 0.3 and 0.003, corresponding to mean grazing angles between about 2° and 0.02° for a sea having a mean slope $s_0 = 0.1$. We see that the probability of illumination changes rapidly over a rather narrow range of surface heights, leading to the idea of "illumination thresholding" mentioned earlier. The "threshold" is taken as the value of $\xi_0$ that makes $P^0 = 0.5$. Points on the surface for which $\xi > \xi_0$ are assumed to be totally illuminated, while those for which $\xi < \xi_0$ totally shadowed. For bistatic scattering, the threshold is determined by the product of two such factors: $P^0(\xi_0, \eta_I)\ P^0(\xi_0, \eta_0) = 0.5$. If the grazing angles over the I and O paths are the same, as the evaporative layer often forces them to be at extended ranges (Wetzel, *loc cit*), then for $\psi < 1°$ the approximation (11') for $\Lambda(\eta)$ indicates that

$$P^0(\xi, \eta) P^0(\xi, \eta) \approx P^0(\xi, \eta/2) \tag{14}$$

or that the bistatic height factor is closely approximated by the monostatic height factor at half the grazing angle.

islands on a two-dimensional sea surface (and to do this we must ignore the mutterings of purists), then the average number of peaks per unit area becomes

$$n = L_{SH}^{-2} \quad \text{peaks/m}^2 \tag{18}$$

For a monostatic radar, the area $A_F$ of the illumination footprint is given by $\beta Rc\,\tau/2$, where $\beta$ is the beamwidth, R is the range, c is the speed of light, and $\tau$ is the pulse length. For bistatic radar, $A_F$ is determined by the intersection of the transmitter and receiver beams, and the pulse length (under pulse limited conditions). In either case, the average number of surface peaks appearing in the radar footprint is

$$N = nA_F = A_F/L_{SH}^2 \quad \text{peaks in } A_F \tag{19}$$

Because of its effect on the statistics of the scattered signal, this number may be called an "intermittency index." It was originally introduced to describe the behavior of the clutter return as seen by a monostatic radar on an A-scope, or a PPI. For $N >> 1$, the instantaneous clutter signal is made up of returns from many peaks, so would display fluctuations about some mean value. For $N << 1$, the radar receiver will be looking at receiver noise most of the time, interrupted occasionally by a sharp spike from an isolated island. Similarly, a sequence of samples collected from a fixed range cell (or beam-intersection cell) will display different temporal statistics according as N is greater or less than unity.

### D. Summary Comments on Shadowing

Little more can be said at present about shadowing of the sea surface at low grazing angles. We have examined the effects of diffraction in a deterministic one-dimensional model, and shown some of the implications of statistical fluctuations in a truer, two-dimensional geometry. The domain of frequency vs windspeed in which geometrical optics provides a reasonable representation of surface illumination was found to be small, yet radar operations do occur in this domain, so the conventional geometrical optics shadowing theories are not totally without value. Besides, they are the only shadowing theories that presently exist.

While the isolation of scattering "islands" by illumination thresholding at low grazing angles is intuitively obvious, it is important to have quantified this process through the lengths $L_f$ and $L_{SH}$ so that we may determine how the size and distribution of these scattering regions depend on operational and environmental parameters.

## III. SCATTERING

The second Basic Question raised in the Introduction concerns the kinds of scattering processes that can be expected to occur at the exposed wave peaks. A real wave peak could have almost any form. In a long greasy swell with no wind, it might even resemble the top of the sinusoid so beloved by the deterministic scattering theorists. But usually the surface is complex, covered by small-scale structure in the form of cusps, wedges, microbreakers, hydraulic shocks, patches of turbulence and gravity/capillary waves, both wind-driven and parasitic. It might contain a sharp crest on the verge of breaking, or, having broken, a cascade of plumes falling down its face, and there could be a cloud of spray droplets above it. Clearly, in the face of all of this real-world complexity, the selection of a convincing, and manageable, scattering model poses some difficulties.

In discussing scattering, however, it is necessary to be somewhat specific about the nature of the scattering obstacle. While the topography of the "scattering island" could take a variety of forms, we should not go too far wrong — at least for any reasonably energetic wind-driven sea — by taking

In Fig. 10 we illustrate illumination thresholding for one realization of a random sea surface. The surface was obtained from a random phase expansion in which the coefficients were defined by a Phillips spectrum for a wind speed of 15 knots; the length of the record is three dominant wavelengths (110 m). The threshold heights were obtained from Fig. 9 by setting $P^0(\xi_0, \eta) = .5$, and using the relation $z = \sqrt{2}\,\xi_0(\eta)\sigma$, where $\sigma$ is the rms wave height of the surface ($\sigma = 0.28$m for this wind speed). Although one should not draw general conclusions from a single example, even this simple exercise displays some of the basic features of illumination thresholding. For the given grazing angles, only the largest peaks on the surface have a chance of being seen: for angles in the range $1° - 2°$, there will be one peak per dominant wavelength (36m); for angles $0.6° - 0.3°$, two peaks are visible over 3 wavelengths; for $0.3° - 0.1°$, only one peak is visible, and for smaller angles no peaks are visible, which means, simply, that the probability per wavelength is less than 1/3.

This behavior was put on a semi-quantitative basis by Wetzel [*loc cit*], who showed that in this regime of grazing angles, the definition of thresholding given above leads to a surface on which isolated scattering "islands" of mean length $L_I$ are separated in a dark plane by a mean distance $L_{SH}$, where

$$L_I = Le^{\xi_0^2}\,[1 - erf\,(\xi_0)], \tag{15}$$

$$L_{SH} = Le^{\xi_0^2}\,[1 + erf\,(\xi_0)], \tag{16}$$

with the characteristic length $L$ defined by

$$L = \pi(\sigma/s_0). \tag{17}$$

It is interesting to compare the predictions of these expressions with the pictorial results in Fig. 10. The behavior of $L_I$ and $L_{SH}$ with normalized grazing angle is plotted with solid lines in Fig. 11 for W = 15 kts, $\sigma = 0.28$m, $s_0 = 0.1$. As the grazing angle decreases, the spacing $L_{SH}$ between islands increases rapidly (from 14m to 190m), while the size of the exposed islands $L_I$ decreases very slowly (from 6m to 3m). The reader will note that the lengths scaled from Fig. 10 for a single realization of the sea surface are, give or take a few inches in wave height, quite consistent with the corresponding numerical values Fig. 11; e.g., for $\psi = 0.4°$, $L_I \sim 3$m and $L_{SH} \sim 30$m.

These statistical results can further be used to explore the effects of mean sea slope $s_0$. The curves in Fig. 9, thus the threshold parameter $\xi_0$ which they select, depend only on $\eta = \psi/s_0$, the ratio of grazing angle to mean slope. Thus if the grazing angle and slope are changed by the same factor, then $\xi_0$ and all of the results depending on it, will remain the same. The only other slope-dependent parameter is the scale length $L$ defined in (17). If we were to make the sea more "choppy" by doubling $s_0$ from 0.1 to 0.2, the effect on the lengths plotted in Fig. 11 would be to halve all of them, and displace them by twice the grazing angle (via redefinition of $\eta$), thereby producing the dashed curves. It is seen that the shadow length $L_{SH}$ remains much the same, while the lengths of the exposed peaks are reduced by about a half; e.g., for $s_0 = 0.2$, $L_{SH}$ goes from 58m to 53m, while $L_I$ is reduced from 3.7m to 1.6m. Thus for a given grazing angle, as the sea becomes choppier, the separation between scattering islands remains much the same, but the areas of the exposed peaks get smaller.

*2. Clutter Intermittency*

The clutter scene presented to a radar in the deep shadowing regime will be strongly structured by the size and spacing of the scattering islands relative to the size of the radar footprint. This topic was discussed at length by Wetzel in the cited reference, where details may be found. If we now assume that the one-dimensional length parameter $L_{SH}$ represents an average spacing between scattering

the basic underlying structure to be wedge-like, with a surface slope of about 30°, corresponding to the surface stability criterion for the onset of wave breaking. In order to avoid having to deal with a full three-dimensional sea, we will initially simplify the problem by assuming this wave-wedge to be sufficiently long crested to extend across the width of the island. Without such restrictive assumptions, it would be discouragingly difficult to obtain any useful information about the deterministic scattering processes that ultimately lie behind the statistical scattering behavior.

We will first examine the neighborhood of the peak, concentrating on possible sources of distributed scatter produced by small features amenable to modeling by perturbation theories. Next we evaluate the wedge as a scattering element on the exposed crest, and finally consider some of the more powerful plume and corner-reflector scatterers that could produce scattering returns consistent with the observed "sea spikes." Throughout this discussion, the importance of shadowing in structuring the scattered field at very low grazing angles will be continually emphasized.

## A. Distributed Scatter: The Bragg Hypothesis

Any small-amplitude approximation for scattering from a statistically rough surface leads to a scattering cross section proportional to the Fourier transform of the surface correlation function evaluated at twice the incident wavenumber; i.e., the surface spectrum evaluated at the "Bragg" wavenumber. The same result is obtained in the theory of scattering from weak turbulence. Having done this essentially trivial mathematical exercise, one is left with two non-trivial questions: (1) Does the surface actually satisfy the conditions of the approximation? (2) What "spectrum" should be used in the formalism? Considering real seas at microwave frequencies, the answer to the first question must be No, since the conditions of the approximation are that the maximum surface displacement be very much smaller than the illuminating wavelength (less than one-tenth). Nevertheless, there are those who attempt to "save the hypothesis" by arguing, for example, that the sea is really "locally flat" when taken in small enough sections. In regard to the second question, if the surface is viewed as a generalized "sea" it is commonly answered by selecting the Phillips spectrum [Phillips, 1966] which is a K-to-the-minus-four spectrum roughly satisfied by real seas, although recent work shows a more complicated spectral structure [e.g., Phillips, 1985, or Pierson and Donelan, 1987]. The latter reference emphasizes the need to use spectra that are accurate in the Bragg resonance region of interest. On the other hand, if a particular scattering structure is being studied, then the spectrum chosen will be representative of that structure, as, for example, in the case of the "solitons" proposed by Middleton and Mellen [1985].

For all the criticism that can be leveled at the Bragg model, it has the virtue of delivering predictions that are often consistent with experience and are difficult to obtain from any other model. For this reason the Bragg model, though conceptually flawed, continues to be used. In this section we view it as a paradigm for distributed scatter generally. It is intrinsically "distributed," in that it derives from either an integral or a wide-sense spatial transform over a flat surface, and it incorporates the surface boundary conditions, thus disclosing a polarization dependence. And finally, we must respect, if not accept uncritically, its apparent ability to agree with measurement in the range of local angles of incidence of interest to us here.

### *1. Bistatic Scattering from Peaks in the Bragg Approximation*

In the simplest possible model, the exposed faces of the wave-wedge are uniformly covered with a carpet of Bragg-scattering wavelets, often called "ripples." The scattering problem for an element of such a surface is treated in detail in the Appendix, Section 1, where the bistatic cross section for scattering through angle $\phi_s$ at very small (close to zero) grazing angles is found for an element with arbitrary slope and azimuthal orientation. The effects of local shadowing are straightforward in this model, since a scattering path will exist only when the planes of illumination and observation intersect

on the front face of the wedge, as expressed by the U-functions in Eqn. (12). Note that the implications of the threshold shadowing theory of Sections II.B. and C. have already been taken into account through the model of scattering "islands" we are using. Referring again to the Appendix, it is clear that if the azimuth angle $\phi_0$ of the surface element is less than $\pi/2$, the illumination ($\hat{k}_i''$) enters the back side of the element and will not be scattered into direction $\hat{k}_s$, while if $\phi > \phi_s + \pi/2$, the observer will be looking at the back side of the element and will not see the scattered field. This means that only those surface azimuths $\phi$ that lie in the range $\pi/2 < \phi < \pi/2 + \phi_s$ can contribute to bistatic scattering through an angle $\phi_s$. (Note that this is a condition on both $\phi$ and $\phi_s$, since it also restricts the range of $\phi_s$ for given $\phi$.) The *mean* cross section per unit area is found by averaging $\sigma$ over this range of angles for a particular probability density function $p(\phi)$. That is,

$$\bar{\sigma}^0(\phi_s) = \int_{\pi/2}^{\pi/2+\phi_s} \sigma^0(\phi, \phi_s)\, p(\phi)\, d\phi \tag{20}$$

where $\sigma^0(\phi, \phi_s)$ is given in (A17). The distribution of wave orientations $\phi$ could be anything from a delta-function, as when the crests line up in a breaking zone, to a uniform angular distribution, as in a short-crested confused sea. Since these represent two opposite extremes, we consider both cases.

Consider first *Case 1*, in which all the wedge faces are oriented with fixed angle $\phi_0$:

$$p_1(\phi) = \delta(\phi - \phi_0) \tag{21}$$

In this case, the average in (20) is obtained by replacing $\phi$ by $\phi_0$ in (A17). The cross sections for the two polarizations are plotted in Fig. 12 for a slope of 30° and for grazing angles close to zero, as explained in the Appendix following Eqn. (A17). "Monostatic" means that the scattering angle $\phi_s = 180°$, while the wedge face is rotated from broadside (180°) to glancing incidence (90°); "bistatic" means that the wedge is fixed in broadside position, while the receiver is moved from a monostatic (180°) to a glancing (90°) observation position.

Referring to Section 1 of the Appendix, it may be seen that for vertical polarization (V-POL), the scattering is controlled almost entirely by the first term in (A14) along with the outboard $\sin^2$ terms in (A17), which force the fall-off as the angles approach 90°. For horizontal polarization (H-POL), the most interesting result is the relative independence of the monostatic return on wedge orientation. This is due to the H-V-H conversion that takes place as the surface normal of the tilted wedge rotates out of the plane of incidence, bringing the first term of (A14) into play for p=H. Thus the H-POL return behaves with wedge orientation angle much like the V-POL return, only lying about 10dB lower. It should be noted that this is the same mechanism that produces the cross-polarized return in the two-scale Bragg model.

Consider next *Case 2*, in which the wedge orientations are uniformly distributed between $\pi/2$ and $3\pi/2$, the allowed range of angles again containing only those for which there is an unshadowed path between source and observer. Here the probability density is given by

$$p_2(\phi) = 1/\pi \tag{22}$$

and the trigonometric functions in (A17) have to be integrated over the restricted range of angles given in (20). The integrals were performed numerically in a simple computer program and the results are shown graphically in Fig. 13.

The vertically polarized returns show a smooth 40dB falloff over the range of bistatic angles, while the horizontal returns have a smaller variation, but seem to display a kind of "resonant" behavior. But these are not true resonances, being artifacts of the changing dominance of the two

terms in (A14) as the scattering angle moves through its range. Reference to (A8) and (A9) reveals that $\alpha_{HH}$ tends to peak at the extremes and have a hole in the middle, while $\alpha_{VV}$ tends to be large in the middle. Thus the H-POL curve starts off much like its bistatic counterpart in Fig. 12, but gets picked up by $\alpha_{VV}$ in (A14) over the intermediate angles, looking like a replica of the V-POL curve until experiencing the effect of $\alpha_{HH}$ again as $\phi_s$ approaches zero. Of greater interest is the other end of these curves, which denote the values of radar *backscatter* cross section predicted by this model. We will find shortly that they are in good agreement with measurement.

*2. The NRCS and a New Shadowing Function*

The results obtained thus far still do not provide us with a prediction of the cross section per unit area (sometimes called the Normalized Radar Cross Section, or NRCS) that would be measured operationally. To do this we recall the basic picture of the scattering "island" as a prism with an interior angle of 120° and base width and crest length of $L_I$. we will assume the grazing angle to be smaller than 30°, so that only one face of the prism contributes in a scattering interaction (the other is in-shadow). The average cross section of a single "island" thus becomes the product of one of the cross sections per-unit-area found above and one-half the area of the island, $L_I(L_I/2)$. If the "intermittency index" defined by Eqn. (19) is considerably greater than 1, then the cross section per unit area measured by a radar is just the product of the average cross section per peak, or "island," with the average number of peaks per unit area, given in Eqn. (18). That is,

$$(\mathrm{NRCS})_p\ (\phi_s) = \bar{\sigma}^0(\phi_s)\ (1/2)(L_I/L_{SH})^2 \tag{23}$$

where the two lengths are given in Eqns (15)-(17), and illustrated graphically in Fig. 11.

As noted at the beginning of Part II, conventional shadowing theory produces a "shadowing function" that smoothly extinguishes the backscatter intensity linearly as the grazing angle approaches zero. In the threshold theory being used here, "shadowing" means something quite different. Here, the cross sections of the individual peaks vary little ($L_I$ is weakly dependent on grazing angle), and the reduction in the NRCS results primarily from collecting fewer of these peaks under the pulse footprint as their separation increases. This behavior is expressed by defining a new shadowing function, $S_T(\psi)$, as 1/2 the length ratio in (23) with the lengths given in (15)-(17):

$$S_T = \frac{1}{2}(L_I/L_{SH})^2 = \frac{1}{2}\left[\frac{1 - erf\ (\xi_0)}{1 + erf\ (\xi_0)}\right]^2 \tag{24}$$

We have plotted this function in Fig. 14, including for comparison the asymptotic form of the conventional shadowing function,

$$S_c \rightarrow \sqrt{(\pi/2)}\ (\phi/s_0) \tag{25}$$

Keep in mind that these averages all make sense only if the intermittency index N in (19) is large. Otherwise the backscatter appears as a random occurrence of isolated spikes. However, when the conditions are right, it is clear that below about 2° the threshold-derived shadowing function will display a much steeper characteristic than does the conventional function.

*3. Comparison with Measurement*

Experimental support for the theory discussed in this section is hard to find, because surprisingly few reliable measurements have been made at very low grazing angles. Moreover, while we have expressed the NRCS in terms of statistical averages, some workers give the NRCS as the *median* cross section. In fact, the problem of finding a suitable statistical characterization for low angle clutter

is not a simple one [see, for example, Trunk, 1976]. Of the few measurements that exist, we review the more pertinent ones below.

a) *NRL 4FR Data*: The Four-Frequency-Radar (4FR) data taken by NRL around 1968 [Daley, et al, 1968] were collected with reasonable care and are often used to "confirm" the Bragg scattering hypothesis [see, e.g., Valenzuela, 1978]. The smallest grazing angle measured was 4°, which is somewhat below the mean sea slope angle and therefore should correspond to the NRCS of (23), with $S_T = 1/2$. Figure 15 reproduces the figures shown in Valenzuela for a frequency of 4.455 GHz (about 7cm wavelength), upwind aspect in strong winds (>22kts). The results at 4° will therefore lie in the upper part of the "Maybe" region in Fig. 5, so our geometrical optics assumptions should be valid. Under these conditions, the appropriate values for the NRCS are taken as 3dB less than those at the left edge of Fig. 13 (to account for the 1/2 in (24)): that is, -30dB for V-polarization and -41dB for H-polarization. These values are indicated by the big circles in Fig. 15, and the agreement with the measured values is seen to be quite good for both polarizations. It should be emphasized that these results are based on a much more sophisticated argument than the simple Bragg scatter curves shown on the Figures, which assume a uniform carpet of scattering wavelets for V-pol, and a normally distributed slope distribution for the composite-surface values in the H-pol plot. However, since the Bragg theory rests on such shaky assumptions, it is quite possible that the agreement with such measurements as these is purely accidental in both cases. Much more needs to be done before the Bragg theory can achieve intellectual respectability, and about all that can be said here is that our results share, with other applications of the Bragg hypothesis, this remarkable tendency to agree with these 4FR data.

b) The Critical Angle: Some 30 years ago, it was observed that when radar sea backscatter was plotted against range, there appeared to be a change in the rate of decrease of signal level at ranges corresponding to a grazing angle of 2° or so [Katzin, 1957]. This angle was called the "Critical Angle," and was ascribed to an interference phenomenon in which direct and (phase-reversed) reflected waves combined above the surface to produce a field at the scattering elements that decreased as the fourth power of the grazing angle. Both the concept and its implications are absurd, and were viewed with suspicion even at the time [Katz and Spetner, 1960]. However, very often something seems to occur in the data at these angles to give the idea of a "critical angle" some objective validity. Most recently, a 2° anomaly has been found in low angle sea backscatter data collected in the North Atlantic [Trizna,1987].
The "interference" argument has persisted because the observed decay law does seem roughly to follow the fourth power of the grazing angle, although once a line has been drawn through a mass of spread data points, the eye is often mislead into accepting an "agreement" that is ambiguous at best (see Fig. 16a). The Threshold Shadowing argument proposed in this report gives an alternative explanation for the observed behavior. We have plotted a fourth power decay law as a dashed line in Fig. 14, and quite clearly it looks very much like the shadowing functions $S_T$ based on Eqn. (24). In Fig. 16b we borrow a figure from the Katz and Spetner paper cited above, showing some X-band data from the RRE in England at very low grazing angles. Superimposed is the "5 kt" shadowing function from Fig. 14, which is in very good agreement with the measured behavior.

c) Other Measurements of Low Angle Sea Backscatter: The lack of good low angle radar data is really rather surprising, considering how easily it could be collected from comfortable sites on the shore overlooking the sea. Two sources of such data are the measurements by Hunter and Senior overlooking the Atlantic from a site in the south of England [1964], and by Sittrop from the west coast of Norway [1975]. These investigators took the trouble to record wind speed and direction while measuring X-band radar backscatter at grazing

angles between about 0.5 to 5 degrees. In Figs. 17a and 17b, we have separated these data into crosswind and upwind/downwind categories and compared them, respectively, with the conventional ($S_C$) and threshold ($S_T$) shadowing functions. One expects that upwind/downwind aspects would be controlled by the deep shadowing responsible for island formation in the threshold model, while crosswind aspects would show the radar the troughs most of the time, and thus would display the more gradual clutter decay described by the conventional shadowing function. There is certainly a strong qualitative difference between the backscatter behaviors for the two aspects, and they corroborate this hypothesis extremely well.

In a brief review of low-angle backscatter, Chan and Helmken [1983] adapt some measurements by others to show the effect of ducting. Their Fig. 7 is reproduced here as our Fig. 18, where we have added the 15kt shadowing function from Fig. 14 as a dashed line. Again, the agreement is very good for the non-ducting conditions. It is of interest to note that the points plotted for the ducted case are not necessarily following a different shadowing function, but instead belong to larger angles than those obtained from simple free-space scaling. The situation expected in the similar case of the evaporation duct is discussed in Wetzel [1977].

d) Measurement of Sea Spikes: A dominant feature of low angle radar backscatter is the presence of Sea Spikes, which are most obvious with horizontal polarization under conditions of low intermittency index N (low grazing angles and small radar footprint), but must also make an important contribution to the NCRS under conditions of large N. The reason, of course, is that Sea Spikes are high-amplitude events, showing cross sections generally above $1m^2$, and at times reaching $20m^2$ or so [Lewis and Olin,1980; Hansen and Cavaleri, 1982; Trizna, 1987]. In our threshold model, Sea Spikes would have to be associated with the exposed islands of scattering area $(L_I)^2/2$, which is of the order of $100m^2$. Considering the values of $\sigma^0$ for distributed clutter shown in Fig. 12, it is obvious that this form of scatter falls far short of being able to account for Sea Spikes. We must seek elsewhere for the source of this important scattering phenomenon.

The agreement between theory and experiment demonstrated thus far is encouraging, particularly the tendency of the new shadowing function to predict the observed backscatter behavior in the limit of extremely small grazing angles - at least in those cases for which Fig. 5 gives geometrical shadowing theory a fighting chance. In regard to the backscatter cross sections themselves, it is of interest to note that the several independent measurements referenced here (NRL/4FR, Katzin, RRE, NWC, Sittrop, Trizna) permit the following "ballpark" estimate of low angle sea backscatter behavior at X-band frequencies: "For grazing angles of a degree or so, moderate wind speeds (about 15kts), and for both H and V polarizations, the NRCS is -40dB($m^2/m^2$) give or take a few db." Considering the wide variety in experimental procedures and cross section derivations, it is quite surprising to find this much consistency in data spanning 30 years.

### *4. The "Soliton" Hypothesis of Middleton and Mellen*

In the previous applications in this section, the spectrum used was the general ocean wave spectrum of Phillips. As noted earlier, Middleton and Mellen [1985] have recently proposed a sea surface model in which the dominant scattering element at low grazing angles is taken to be a "Soliton," that develops out of a hydraulic shock that is produced, initially, by a puff of wind. Actually, close observation of a dynamic, wind-driven surface lends some credence to the wind-puff/hydraulic shock connection, although the production of solitons by this mechanism has met with skepticism [Pierson, private communication]. The hypothesis is highly speculative, and Middleton and Mellen have no strongly convincing arguments in support of it. Nevertheless, it has a certain appeal - particularly in a field where there have been no new ideas for over 20 years.

The profile of the soliton is taken to be a simple Gaussian shape with a certain height H, width L, and speed c:

$$z(r,t) = H \exp(-4(r - ct)^2/L^2). \tag{26}$$

From some reasonable statistical assumptions, a correlation function was calculated, whose Fourier transform provided a spectrum having the following form:

$$w(k) \sim (h^2w^2)/[1 + (kw/2)^2]^2 \tag{27}$$

where h and w are the rms values of H and L in (26). It is of interest to note that when $kw > 2$, the spectrum assumes the k-minus-4 dependence familiar from the Phillips sea wave spectrum.

Middleton's interests lie primarily in acoustic scattering, so he assumed that the dimensions of these objects were small enough that the spectrum in (27) could be used in the Bragg formalism, and calculated the normalized backscatter cross section for an ensemble of such objects on an acoustically "soft" (pressure-release) surface. (In the duality between acoustic and electromagnetic scattering, this would correspond to horizontal polarization.) For low grazing angles (less than about 10°), the resulting NCS can be written in the form:

$$\sigma^0 \sim \left(\frac{h}{w}\right)^2 s_0^4 \left[\frac{(kw)^4}{[1 + (kw)^2]^2}\right] \tag{28}$$

where $s_0$ is the rms sea wave slope (which plays the role here of the grazing angle in the previous Bragg theory), and k is the sonar/radar wavenumber. Since the "soliton" object has the form of a Gaussian perturbation, we might consider it as representative of isolated scattering features generally. That is, (26) is a scattering *something* that has a height and a length which are statistically characterized by rms parameters. Thus we might be tempted to regard the cross section in (28) as generic for such scattering objects. At least the asymptotic behavior is reasonable: when $kw > 1$, the cross section is independent of frequency, as one would expect in Bragg scattering using the k-minus-four spectrum derived above for these objects; when $kw < 1$, the cross section assumes the wavelength-minus-4 dependence of Rayleigh scattering, and very closely resembles Booker-Gordon scattering by weak atmospheric irregularities [1960]. Thus, alas, the results are only what one would expect *a priori* under the conditions describing this type of scattering, so we have really learned nothing new from this approach.

## B. Implications of Wedge Models

Close observation of almost any open water surface discloses that the basic surface features are wedge-like structures, not the sine waves or patches of gravity/capillary waves that make life easy for the scattering theorist. Scattering from those wedges that are large compared to the incident wavelength may be treated by one of the short-wavelength approximations. Since the interior angles are limited by surface stability conditions to about 120°, the wedge faces will, at low grazing angles, generally be viewed at oblique incidence, where Physical Optics tends to underestimate the scattering, and asymptotic scattering theories emphasizing edge effects begin to provide significant corrections. All such theories date from Sommerfeld's rigorous treatment of diffraction at edges in 1896, and while Sommerfeld himself reduced his solutions to more manageable Fresnel integrals and their asymptotic forms, the present theories of wedge scattering derive from the reinterpretation of these results independently by Keller (GTD) and by Ufimtsev (PTD) in 1957. But before trying to make sense out of some of these wedge scattering theories, we will take a brief look at the few existing applications to sea scatter.

*1. Previous Applications of Wedge Models*

Although wedges are an obvious feature of the sea surface, scattering models based on wedges have made their appearance only recently.

a) Kalmykov and Pustovoytenko [1976]: These authors describe X-band backscatter measurements at low grazing angles ($<3°$) in which "bursts" occur for both horizontal and vertical polarizations. They found that the horizontal returns were often greater than the vertical, contrary to the usual backscatter experience at higher grazing angles. In an attempt to provide some explanation for this behavior, they assumed that the "bursts" were due to breaking crests pointing toward the radar, as sketched in Fig. 19a. The cross section ratios were calculated from the classical asymptotic forms (which are the same as the GTD diffraction coefficients). The coefficients plotted in Fig. 19a as a function of interior wedge angle apply to the model contained in the paper, which may, or may not, have any validity. The authors wisely did not press the issue.

b) Kwoh and Lake [1983]: Small 2-D wedge-like waveforms were generated mechanically in a wave tank, and profiled with a scanning laser slope gauge. A method-of-moments calculation of scattering by the resulting shapes showed angle and polarization dependence quite similar to the GTD results for a wedge, and were in reasonable agreement with measurements of the scattered field, at least for angles above the minimum grazing angle of 22°. This work has important implications in the modeling of sea scatter, and should be read by anyone with an interest in the field.

c) Lyzenga, Maffett and Shuchman [1983]: Using what is essentially the PTD formalism for a 120° wedge, these authors found the edge contribution to wedge scattering, and showed that by adding a suitable portion of this component to the conventional Bragg component, an improved fit can be obtained with the NRL 4FR X-band data for horizontal polarization and grazing angles from 5 to 30 degrees.

d) Wetzel [1986a]: Noting that the sea surface is a "wedgy" rather than a "wavy" surface, this author found such a surface to have the expected k-minus-four spectrum, but with a spectral scale factor that is proportional to wind speed. This wind speed dependence seems to track the NRL 4FR data quite well (if massively averaged), and a GTD calculation of wedge scattering provides both grazing angle and polarization agreement superior to that provided by the Bragg theory in the angular range in which Bragg theory is usually thought to apply. But as in all applications of discrete-target scattering models to the sea, there is no independent *a priori* basis for establishing target size and distributions, hence either mean or specific scattering levels.

*2. Problems in Applying Wedge Theory to Sea Scatter*

All of the above calculations used a simple two-dimensional wedge model, while for application to a real sea surface it will be important to consider scattering in three dimensions. In GTD, an extension to three dimensions occurs in allowing oblique incidence, in which case the scattered field appears in the form of a cone of rays - the so-called "Keller Cone" - whose half-angle is equal to the angle of incidence at the edge [Keller, 1957]. There are no other scattered waves; this is still a strict optical theory. The next extension is a generalization in which it is assumed that the incident field excites at each point on the edge a fictitious physical current of just such a form as to produce the scattered field on the optically defined Keller Cone emerging at that point. The edge may now be made arbitrary, and the current thus defined is integrated along the edge, as if it were a real current, to yield a value for a scattered field at points in space lying outside the Keller Cone. Several formalisms based on this idea have emerged in recent years: the Method of Equivalent Currents (MEC) as described by

Knott and Senior [1974], the method of Incremental Length Diffraction Coefficients (ILDC) by Mitzner [1974], Michaeli's MEC (MMEC) by Michaeli [1984], to name the most important. Ufimtsev's PTD, which has already been used in section II.A.2, is also concerned with edge currents, but indirectly, as a conceptual device for the correction of the Physical Optics approximation rather than in concrete form for the calculation of scattered fields. It should be noted that none of these methods is more "fundamental" or "rigorous" than the others. They are all of them - GTD, PTD, MEC, ILDC, MMEC - heuristic procedures for finding approximate solutions to scattering problems involving objects with edges (or "ribs," as Ufimtsev calls them). And there are still other methods (known by their acronyms as UAT, UTD, STD, HTD, etc.) which are designed mainly to eliminate the caustic singularities in the GTD, and will not concern us here. Since most of these asymptotic theories are quite complex, and often seem to differ in obscure ways, they are constantly being intercompared (e.g., Knott and Senior, 1974; Plonus,et al, 1978; Knott, 1985), or measured against Sommerfeld's original rigorous solution (Deschamps, et al, 1984).

In order to disentangle ourselves from this mass of scattering theories and methodologies, we consider first the very basic problem of two-dimensional scattering from a wedge as described by the GTD. In Fig. 20a, the incident ray, denoted by $k_i$, encounters an infinite 2-D wedge having an interior angle $\alpha$ and lying normal to the plane of incidence. $e_V$ and $e_H$ indicate respectively the orthogonal Vertical and Horizontal polarizations. In the GTD, the scattered field consists of two parts: a field $E_{GO}$ reflected from the illuminated face of the wedge according to the laws of geometrical optics, and a "diffracted" field, $E_D$, originating at the edge, consisting of a fan of rays which, for incidence normal to the edge, uniformly cover the plane of incidence. The field on these rays is defined by

$$E_{H,V}(\gamma_i, \gamma_s) = \frac{e^{i(kr+\pi/4)}}{\sqrt{2\pi kR}} D_{H,V}(\gamma_i, \gamma_s) \tag{29}$$

where

$$D_{H,V}(\gamma_i, \gamma_s) = \frac{\sin(\pi/n)}{n} \left[ \frac{1}{\cos(\pi/n) - \cos(\gamma_s - \gamma_i)/n} \pm \frac{1}{\cos(\pi/n) - \cos(\gamma_s + \gamma_i)/N} \right] \tag{30}$$

with $n = 2 - \alpha/\pi$ (the *exterior* wedge angle is $n\pi$), and the incident and scattering angles measured from the front face of the wedge. The - and + signs are used for the H and V polarizations respectively. The four rays labeled in Fig. 20a have special significance: $E_D^1$ returns to the source and contributes the backscatter cross section of the wedge; $E_D^2$ defines the "reflection boundary" for the front face, and since its angle is $\gamma_s = \pi - \gamma_i$, it causes the second term in (30) to blow up; $E_D^3$ is a ray which would correspond to "specular reflection" if the wedge were sitting on a plane surface; $E_D^4$ defines the "shadow boundary" and since its angle is $\gamma_s = \pi + \gamma_i$, it causes the first term in (30) to blow up. These singularities are in no way related to actual field behavior, of course. They are artifacts of what is essentially an asymptotic expansion of the Fresnel Integral in Eqn. (3), where the leading term is proportional to 1/w, hence to $1/(\sqrt{kR/\pi\theta})$. This means that the GTD can be used only for angles well outside an angular zone of width $1/(\sqrt{kR/\pi})$ surrounding the singular rays. But except for these singular domains, the GTD has often been found to give reasonable approximations even under conditions fairly well removed from the "optical limit."

If end-effects are ignored, two-dimensional fields can be converted into three-dimensional fields "per unit length" by the factor $(k/2\pi R)^{1/2}$, from which a cross section defined in the usual way takes the form

$$\sigma_{H,V}(\gamma_i, \gamma_s) = L^2 D_{H,V}^2(\gamma_i, \gamma_s)/\pi \tag{31}$$

where L is the length of the wedge. This is the form used by Lyzenga, et al [*loc. cit.*] for their PTD corrections to Bragg scatter, and by Plonus, et al [1978] in an interesting experimental comparison of various approximation methods. Backscatter cross sections obtained by substituting (30) into (31) with $\gamma_s = \gamma_i$ are shown as functions of wedge interior angle in Figs. 19: for incidence along the wedge-angle bisector (Fig. 19a, corresponding to the breaking wave model used by Kalmykov and Pustovoytenko, *loc. cit.*) and at zero grazing angle across the top of the wedge (Fig. 19b, corresponding to the normal wedgy sea of our low-angle model.) We see that the polarization dependence is reversed for these two cases (H>V in 19a, V>H in 19b). In Figs. 21 we show two examples for a stability-limited wedge angle of 120°: in Fig. 21a, the backscatter cross section versus grazing angle from 0 to 90 degrees, and in Fig. 21b, the bistatic cross section for scattering angles between 0 and 180° in the plane of incidence, for a zero degree incident grazing angle. The plots show similar behavior, having an infinity in the direction of specular reflection from the front face. In the backscatter case, this direction corresponds to broadside scattering, which is generally an intractable case for GTD-like approximations (see, e.g., Sikta,et al,1983). Fig. 21a was used by Wetzel [1986a] to compare the implications of wedge scattering with some NRL 4FR backscatter data. The circles on Fig. 21a show the relative behavior of the 4FR data with polarization and grazing angle.

But such curves, based on such theories, cannot tell us what we really want to know. They apply to a perfect wedge, aligned with perfect precision normal to the plane of incidence. As soon as the wedge deviates from the perpendicular, by however small an angle, the backscattered field vanishes. The reason for this is seen in Fig. 20b, where the incident ray makes an angle $\beta \neq \pi/2$ with the wedge edge, and the diffracted rays now all lie on the Keller Cone, whose interior half-angle is $\beta$. As mentioned earlier, there are no other diffracted rays - certainly none back into the direction of incidence to produce "backscatter." The bistatic case is no better, because the observer must lie on one of the elements of the Keller Cone, and again a scattering path is possible only for a single, precise orientation of the wedge edge. These unforgiving geometrical constraints can be relieved only by a return, in one form or another, to the basic idea of scattering from current distributions; that is, by using the fictitious "equivalent currents" in geometrical theories, or the approximate "optical currents" in Physical Optics.

a) Method of Equivalent Currents: The bistatic cross section for a 120° wedge of length L in the low grazing-angle limit is calculated using the MEC in Section 2 of the Appendix:

$$\sigma_{H,V}(L;\phi_w,\phi_s) = C_{H,V}\, L^2\, sinc^2\left[\frac{1}{2}kL\,(\cos\phi_w - \cos(\phi_s - \phi_w))\right] \qquad \text{(A21)}$$

where $C_{H,V}$ = -29dB (H-pol), -8dB (V-pol), and $\phi_w$, $\phi_s$ are the azimuthal wedge and scattering angles respectively (see Fig. A3). (To avoid confusion, it should be noted that in Eqn. (31) and Fig. 21b, the bistatic angle lies in the plane of incidence and sweeps up and over the top of the wedge, while in (A21) and Fig. A3, the bistatic angle is azimuthal and sweeps around the wedge in the horizontal plane.)

At this point we should recall to mind one of the central problems with all models, of this sort, that introduce specific scattering structures having no natural origin in the physics of the underlying surface. That is, while we see wedge-shaped structures on the surface of the sea, they have never been measured and counted as such, so there is no knowledge of the distributions of their sizes and orientations. Nor is there a body of hydrodynamic theory from which such distributions might be inferred. For this reason we are left with the need to come up with "reasonable" assumptions for these distributions, which usually translates as "not completely idiotic," and leaves one with a corresponding skepticism about any conclusions drawn from them Nevertheless, we cannot proceed without taking this necessary step.

It would be absurd to assume the scattering island to consist of a single large, coherently scattering wedge of length $L_I$, so we will replace this overly simplified model with one in which the illuminated islands are populated by ensembles of wedges of various sizes and orientations, having individual cross sections given by (A21). For backscatter, the scattering angle $\phi_s = \pi$, and since the sinc-function gives a very narrow beam around the wedge angle $\phi_w = \pi/2$, we can write (A21) as

$$\sigma_{H,V}(L,\delta) \approx C_{H,V} L^2 \, sinc^2(kL\delta) \tag{32}$$

where $\delta$ is the departure of $\phi_w$ from $\pi/2$. The "3-dB" points of the $sinc^2$ function occur at $\pm kL\delta \approx \pi/2$, so the range of wedge angles that could contribute to the backscattered signal is just

$$\Delta = 2\delta = \pi/kL . \tag{33}$$

Assuming the wedge angles to be uniformly distributed, the probability that a wedge of length L will provide a backscattered return becomes

$$P_{BS}(L) = \Delta/\pi = 1/kL \tag{34}$$

If each such wedge is further assumed to scatter independently, then the average cross section may be written as the average of (32) times (34) over the distribution p(L) of lengths L:

$$<\sigma_{H,V}> \sim C_{H,V} \int_0^\infty L^2 \left( \frac{1}{kL} \right) p(L)dL = \frac{C_{H,V}}{k} \int_0^\infty Lp(L)dL . \tag{35}$$

The wedge lengths L will be distributed between some minimum length (which seems by observation to be about 10cm), and some much larger length of the order of the Island dimension $L_I$. Not knowing what form this distribution might take, we choose a Rayleigh distribution

$$p(L) = (L/L_0^2)e^{-L^2/2L_0^2} \tag{36}$$

in which the mean length $L_0$ lies somewhere between the extremes stated above. With this choice, the average cross section per wedge in (35) becomes

$$<\sigma_{H,V}> = \pi/2 \; (L_0/k) C_{H,V} \tag{37}$$

The "wedge" in our model is really a kind of flat prism, as sketched in Fig. A3, and since neither long, thin nor narrow, tall wedge faces are physically reasonable, or visually verified, we take a canonical aspect ratio of 2/1 for the length/height ratio of all wedge faces, so that the mean "area" of a wedge against the plane of the sea is about $L_0^2$. Assuming, now, that the wedges are distributed densely over the scattering islands, and that the grazing angle is sufficiently low that only half are visible ( $\psi < 30°$), yet sufficiently high to be above the threshold shadowing knee in Fig. 14 (a degree or two), the NRCS from (23) takes the form

$$\text{NRCS}|_{H,V} = <\sigma_{H,V}>/2L_0^2 = C_{H,V} \pi/8 \; /(kL_0). \tag{38}$$

Finally, in order to make some kind of reasonable estimate of $L_0$, we let $L_0$ be the geometric mean of $L_{MIN}$ (about 10cm) and $L_I$:

$$L_0 = (0.1L_l)^{1/2} \tag{39}$$

For moderate wind speeds $L_l$ is about 10m, so the mean wedge size is about 1m. Using this value and the values of $C_{H,V}$ from (A21) in (38) for X-band frequencies (k=200/m), the NRCS's become

$$\text{NCRS}\,|\,\text{v} = -33 \text{ dB } (\text{m}^2/\text{m}^2)$$

(40)

$$\text{NCRS}\,|\,\text{H} = -54 \text{ dB } (\text{m}^2/\text{m}^2)$$

b) Physical Optics: It was noted earlier that Physical Optics (P.O.) underestimates the scattering at the flatter surface aspects seen in the low grazing-angle regime, which means at relatively large off-broadside angles, well down into the sidelobes of the scattering pattern. This occurs because of the inaccuracy of the assumed current distributions at the edges, but the field predicted by P.O. seems to be badly in error only in those configurations where the diffracted rays of GTD and PTD would normally come into play; which is to say, only under certain highly specialized conditions. Moreover, it should be emphasized that while the PTD is considered to provide edge-wave corrections to Physical Optics, these corrections share the geometrical constraints of the GTD. It is therefore of interest to look at the scattering implications of a straightforward P.O. approach.

The P.O. cross section of a rectangular plate with sides a and b, viewed at angles $\sigma'$ and $\phi'$, where $\sigma'$ is the angle between the plate normal and the incident direction and $\phi'$ is the angle of the plane of incidence relative to the a side, is given by Kerr [1952] in the form

$$\sigma(k, a, b, \delta', \phi') = \frac{k^2(ab)^2}{\pi} \left[ \frac{\sin^2(ka\sin\theta'\cos\phi')}{(ka\sin\theta'\cos\phi')^2} \cdot \frac{\sin^2(kb\sin\theta'\sin\phi')}{(kb\sin\theta'\sin\phi')^2} \right] \cos^2\theta \tag{41}$$

Notice that there is no polarization dependence in the P.O. approximation. The scattering geometry may be viewed in terms of Fig. A1, where $\theta'$, $\phi'$ in (41) are replaced by $(\phi - \pi/2)$, $(\pi/2 - \psi)$, with $\psi$ given by Eqn. (A4). It will again be assumed that the exposed scattering islands are covered by wedges whose orientations, $\phi$, are uniformly distributed, whose lengths, $L_l$, are Rayleigh distributed, and whose aspect ratios b/a are all equal to 1/2 (i.e., a=L, b=L/2, for all values of L.)

Performing the averages as in the last section, we write:

$$<\sigma> = \frac{k^2}{4\pi} \int_0^\infty L^4 F(kL)\, p(L)\, dL\,, \tag{42}$$

where p(L) is given in (36), and F(kL) is the angle integral,

$$F(kL) = \frac{1}{\pi} \int_{-\pi/2}^{+\pi/2} sinc^2\,(kL\cos\psi\sin\phi)\, sinc^2\,(\frac{1}{2}kL\cos\psi\cos\phi)\sin^2\psi \cdot d\phi \tag{43}$$

with the definition (from (A4), with $\theta = 30°$, $\psi_i^0 = 0°$)

$$\psi = \arcsin\,(\frac{1}{2}\cos\phi). \tag{44}$$

The solution of this set of relations is less formidable than it might appear. Numerical evaluation of the integral in (43) discloses that it can be quite accurately represented by

$$F(kL) = 2/(kL)^3 \tag{43'}$$

Substitution into (42) yields the very simple expression

$$<\sigma> = \pi/2\ (L_0/k)(1/2\pi) \tag{45}$$

which should be compared with the MEC result in (37). Since $1/2\pi$ can be expressed as -8 dB, we come to the remarkable conclusion that for this low grazing angle regime, the P.O. cross sections for H and V polarization are exactly the same as the MEC cross section for V polarization. Perhaps this is not so remarkable as it is reassuring, since GTD and P.O. quite often give similar results in scattering calculations. But the paths leading to (37) and (45) were enough different that one cannot help being struck by the coincidence of the two results. Aside from numerical constants, these expressions have the form $(L_0^2)$ times (1/kL), the first being a "size" factor proportional to the area occupied by the wedge, and the second being a "beam" factor, expressing the decreasing number of wedges seen as their average scattering pattern narrows. The uniform angular distribution used in these calculations are appropriate to an isotropic, or "confused" sea. But if a strongly directional sea were viewed up/down wind or crosswind, the form and frequency dependence of these cross sections might change significantly.

*3. Recapitulation*

Thus far we have examined three scattering models for low grazing angle sea backscatter, and mentioned some of the results of experimental measurements in this scattering regime. It would be useful at this point to pause for a moment and intercompare the values of the NRCS obtained from these various sources for X-band backscatter in moderate winds.

| SOURCE | V-Pol | H-Pol |
|---|---|---|
| NRL 4FR (About 5°) | -33 dB | -37 dB |
| Bragg Model (Sec. III.A.1) | -30 dB | -42 dB |
| MEC Wedge Model (Sec. III.B.2a) | -33 dB | -54 dB |
| P.O. Wedge Model (Sec. III.B.2b) | -33 dB | -33 dB |
| "Consensus Meas. (about 1°) | -40 dB | -40 dB |

The cross sections from the scattering models developed in this report assumed grazing angles above the "knee" in Fig. 14, so should be compared against the NRL 4FR measurements at 4 or 5 degrees. The "Consensus" measurements, mentioned at the end of Sec.III.A.3, were all made at grazing angles of about 1°, so should be compared against the model values lowered by the additional 7 or 8 dB required by the $S_f$ curves in Fig. 14. One is tempted to conclude from this that the models are all quite good for Vertical polarization, while for Horizontal polarization the Bragg model is not bad at the higher angles and the P.O. model much better at the lower angles. The MEC model, based on the geometrical theories of diffraction, appears to underestimate the level of Horizontally polarized backscatter by 15 to 20 dB in this regime of grazing angles. However, none of these models can account for the powerful "Sea Spike" returns that characterize this regime, and which could themselves make a contribution to the averaging process defining the NRCS. These returns will be the subject of the next section.

## C. Scattering by Other Surface Features

Thus far we have looked at scattering from small amplitude surface perturbations amenable to a Bragg scatter formulation, and at wedge-like structures of indeterminate size, but large enough to be treated by optical approximations, both geometrical and physical. Other surface features might include:

(i) Pyramidal cusp-like structures, that probably scatter much like a short-crested wedge, or two wedges meeting at an angle.

(ii) Parasitic capillaries, that are visible on the front face of most forced waveforms, are of low amplitude, and appear to occupy a rather narrow spectrum with wavenumbers in the neighborhood of the transition between gravity and capillary waves.

(iii) The pools of surface turbulence associated with breaking waves. If the surface displacement spectrum of the turbulence were known, its scattering behavior could most likely be obtained from the Bragg formulation described earlier.

(iv) The spray associated with vigorous breaking in strong winds. Looking at waves breaking over a submerged breakwater that produced a lot of spray, Kalmykov, et al [1976], used a rain model to explain their measurements. This model required an equivalent rain rate of 1 meter per hour (!) to match the observed levels of backscatter. Since it is difficult even to conceive of what a rain rate of such intensity might actually be like, it is quite possible that they were barking up the wrong tree.

There are two other kinds of structures that will occupy our attention for the remainder of this section: "shocky"-looking structures seemingly associated with localized wind-puffs or the passage of a steep wave, and the "plumes" sliding down the front faces of breaking waves, as suggested by Longuet-Higgins and Turner [1974]. The feature that characterizes both of these structures is the sharp entry into the underlying surface at their "toe" as they move along.

### *1. Hydraulic Shocks or "Sloshes"*

Consider first the subject of "hydraulic shocks." When associated with shallow water effects such as a bore on a beach, breaking in the surf zone, or constricted flows in a channel (see Lighthill, 1978), they are usually referred to as "hydraulic jumps." But as noted earlier, Middleton and Mellen [loc cit] have proposed that wind puffs on an open sea surface may induce small hydraulic shocks that decay into Gaussian solitons which, in turn, become a source of scattering. A bit of "naked eye oceanography" convinces one that small shocky-looking structures occur commonly on open water surfaces, sometimes in response to small-scale turbulent components in the surface wind field, and sometimes for reasons that are not clear. In fact, they are seen quite frequently at wind speeds above a few knots, taking the form of what might be called "micro-breakers," and seemingly induced by the passage of small, but steep, waveforms. Such an event may be seen at the arrow in the tank wave shown in Fig. 22. (Parasitic capillaries of the type also seen in the figure are found everywhere on almost any disturbed water surface.) Small shocky structures can be created on the surface of a basin of water by blowing at it obliquely with a household fan. In a laboratory setup of just this kind, a high-resolution radar looking into the wind has recorded sharp spikes of backscatter which seem to be associated with the formation of these structures [Hansen and Wetzel, unpublished observation, 1986].

Figure 23a shows what a puff-induced event might look like, based on both observation and physical plausibility. The vertical force of the localized puff causes a dimple in the water surface, while the horizontal component urges the edge of the dimple on the downwind side to move out from the center at a speed greater than the normal wave velocity for an impulsively excited surface, causing the forward face of the disturbance to steepen up and show a sharp entry into the quiet water ahead. The

mysterious "micro-breakers" mentioned above look very much the same. It is tempting to call this a "shock wave," but we must be careful not to confuse a "shock wave" with an asymmetrical "slosh." A shock wave tends to retain its form over some reasonable distance, while the event we are talking about here is short-lived, and its subsequent development is uncertain. If it relaxes into a smoother form of disturbance propagating from the puff site with unchanging shape, it becomes the presumed source of Middleton and Mellen's Solitons. But perhaps the initial "slosh" flies apart into a dispersal of wave components running at different speeds.

The nature of these events appears to be completely unknown, although one can imagine that the scale of the phenomenon will play a role. It has been observed that the "ring wave" produced by the splash of a raindrop on a water surface propagates away from the splash site as a single, well-defined waveform [Wetzel,1987]. The speed of this waveform is quite close to the minimum in the velocity vs. wavelength characteristic for water waves. The neighborhood of this minimum contains a relatively broad range of wavelengths with similar velocities, so it is reasonable to imagine that a group of waves having close to the same velocity might assemble itself from the chaos of the initial splash because the scale is right for such a result. Raindrop splashes are measured in centimeters, as are the critical wavelengths at the velocity/wavelength minimum. The scale lengths in the atmospheric turbulence responsible for surface "puffs," or in the perturbing waveforms responsible for "micro-breakers," should be considerably larger, however, so the wavelengths involved will lie along the gravity-wave dispersion curve, and the transient "slosh" will quickly disintegrate. We will try to make some sense of this topic by considering several scattering models that might apply to surface events which start out looking like the disturbance sketched in Fig. 23a.

In Fig. 23b the disturbance is shown separated by a dotted line into a symmetric "dimple" and the asymmetrical "slosh" component. The model is further developed in Fig. 23c, where the "slosh" is idealized as a ridge of transverse length L, having the cross-section of a circular segment of radius a and entry angle $\beta$, and lying at the edge of a "dimple" of radius R. The scattering behavior of this disturbance will, of course, depend on the dimensions a, L and R, the angles (local grazing angle), and the wavelength of the incident signal. Since this is so speculative a scattering mechanism, and we have no clear idea of how it originates, it is difficult to decide what range of dimensions might actually be of interest. To be quite arbitrary, yet guided by observation of these events, we will take "dimple" radii to lie between 10cm and 1m, with "slosh" radii a some small fraction of R. For microwave wavelengths between 1 and 100cm, then, we will have to consider both long-wavelength (perturbation) and short-wavelength (physical optics) approximations. The depth of the "dimple" will, by the conditions of its formation, always be a very small fraction of the radius, and, based on a "ring wave" scattering calculation by Wetzel [1987], we will assert without proof that a wide, shallow depression of the type sketched in Fig. 23a will have an extremely small scattering cross section whatever theory is used. This leaves us with the more sharply curved, elevated "slosh" feature as the major contributor.

a) Long-Wavelength (Perturbation) Approximation: If the height of the circular segment in Fig. 23c is much smaller than a wavelength of the incident signal, a simple surface-perturbation theory of the type used by Wright [1966] can be used. His expression for the backscatter cross section due to a surface perturbation (x,y) is given in the Appendix, Section 3, Eqns. (A23), (A24), (A25). It should be noted that this is a deterministic cross section for a specific perturbation, not a statistical result based on a surface correlation function, as in Rayleigh/Rice perturbation theory and the Kirchhoff theory of Beckmann and Spizzichino [1963].

With reference to Fig. 23c, the integral in (A23) can be written

$$I(\psi) = \int dy \int_{a\sin\theta_-}^{a\sin\theta_+} (\sqrt{a^2 - x^2} - b)e^{jKx}\, dx \,, \tag{46}$$

where $b = z_0$ controls the shape of the segment, as well as the "toe" angle $\beta$, and $K = 2k\cos(\psi)$. It is obvious that under the conditions for which the perturbation approximation is valid ($ka << 1$) the exponential may be put equal to 1, and the integral becomes simply the volume, V(a,L), of the segment, so the cross section of the "slosh" feature takes the simple form:

$$\sigma_{PERT} = \frac{4}{\pi} k^4 |g_{V,H}|^2 V^2(a,L) \tag{47}$$

with the angle factors $|g_{V,H}|$ given by (A24) and (A25). (Note the interesting similarity to volume scattering in the Born Approximation for a volume of unity dielectric constant.) Taking the circular segment to be a semicircle, the volume is $V = a^2L/2$, so the cross section in (47) becomes

$$\sigma_{PERT} = \pi(ka)^4 L^2 |g_{V,H}(\psi)|^2, \quad ka << 1, \tag{48}$$

where L is the transverse length of the structure. (It is of further interest to note that this is exactly the form initially obtained by Wright [1966] for the cross section of a patch of area $L^2$ containing Bragg-resonant capillaries of rms height a.) The angular g-factors are plotted in Fig. 24 for a dielectric constant = 50, corresponding to sea water at X-band frequencies. It should be noted that these angular factors are the same ones that appear in all EM Bragg scattering theories, as, for example, in the "slightly rough" Bragg curves in Fig. 15.

b) Short-Wavelength (Physical Optics) Approximation: When the circumference of the segment in Fig. 23c is long compared to a wavelength ($ka >> 1$), it is appropriate to use the physical optics approximation. Here the scattering takes place at the point of specular reflection, shown as the point P in Fig. 23c. For a conducting cylinder of radius a and length L, the cross section in this approximation is given by $.5(ka)L^2$ [Kerr, 1951 - we have added a factor of .5 to account for the reflection coefficient of water at microwave frequencies]. However, the water surface ahead of the scatterer produces a reflected wave which must be added to the incident wave in the neighborhood of P. Strictly speaking, for very large ka, the surface-reflected wave will itself be specularly reflected at P, away from the incident direction. However, for relatively small values of grazing angle , and modest values of ka, the scattering patterns of the direct and surface-reflected waves at P should overlap back at the source. The effect may be simulated by multiplying the specular-point cross section by an angle- and polarization- dependent factor based on the geometry of Fig. 23c:

$$F^2 = |E_{DIRECT} + E_{REFLECTED}|^2 \tag{49}$$

$$F^2_{V,H}(a,f,\psi) = |e^{ika\cos 2\psi} + R_{V,H}(f,\psi)e^{ika}|^2$$

where $R_{V,H}(f,\psi)$ is the (complex) reflection coefficient for an incident wave of frequency f and grazing angle. We call $F^2$ the "Surface Proximity Function" and have plotted it for both polarizations, in Fig. 25a for ka = 2,4,6, and in Fig. 25b for the larger values ka = 10,20. The physical optics approximation for scattering from a large "slosh" may thus be written

$$\sigma_{PO} = \frac{1}{2}(ka)L^2 F^2_{V,H}(a,g,\psi). \tag{50}$$

c) Effects of Surface Slopes and Wind Speed: The angle in the factors $|g|^2$ and $F^2$ is the local grazing angle. These scattering structures are excited on the sea surface, so this local angle will be $\psi = \psi_0 + \alpha$, where $\psi_0$ is the grazing angle relative to the mean surface (horizontal), and $\alpha$ is the local slope angle of the underlying surface. When the scattering structure is tilted toward the incident ray, the local grazing angle increases, while when tilted away, the angle decreases, reaching its minimum of zero when $\alpha = -\psi_0$. Let us assume that the sea slope distribution is Gaussian [Kins-

man, 1965], characterized by an rms slope $s_0$ which, for the relatively small angles involved ($< 30°$) can be replaced by the slope angle. The averages of the angle factors in (48) and (49) therefore become, respectively,

$$< |g_{V,H}(\psi_0)|^2 > = \frac{1}{\sqrt{2\pi} s_0} \int_{-\psi_0}^{\infty} |g_{V,H}(\psi)|^2 e^{-\alpha^2/2s_0^2} d\alpha, \tag{51}$$

$$< F_{V,H}^2(a, f, \psi_0) > = \frac{1}{\sqrt{2\pi} s_0} \int_{-\psi_0}^{\infty} F_{V,H}^2(a, f, \psi) e^{-\alpha^2/2s_0^2} d\alpha. \tag{52}$$

The dependence of mean square slope on wind speed may be found in the celebrated sun-glitter measurements by Cox and Munk [1954]. They measured the glitter from both clean surfaces, which included the flashes from all the small-scale structure, and "oiled" surfaces, on which the capillaries were suppressed. Since we are primarily interested in the larger slopes of the underlying surface, we will use the latter, for which the mean-square slope $s_0^2$ is given by

$$s_0^2 = 0.008 + 0.00156W, \ (W \text{ in m/sec}). \tag{53}$$

The use of (53) in (51) and (52) gives an estimate of the wind-speed dependence of the "slosh" cross sections (viewed normal to L) for given dimensions a and L, which will themselves be functions of wind speed. For a moderate wind speed of 15 kts, the rms slope is 0.14 (about 8°). We have shown the effect of such a wind on the angle factors $|g|^2$, as calculated from (51), by the dashed curves in Fig. 24. The result is akin to the Two-Scale Bragg model illustrated on the H-Pol curves in Fig. 15. The effect on the Proximity Factors for Physical Optics is more complex, since the averages depend on the scatterer size and the illuminating frequency, as well as on the rms slope. In Fig. 26, the effect of a 15 kt. wind is shown for the same values of ka used in Fig.25. There is little effect on the V-Pol returns, other than to bring up the very low angle segment of the curve and to smooth the angular resonances at the higher ka's. The effect on the H-Pol curves is much more pronounced, and the H-Pol returns actually match or exceed the V-Pol returns over the entire angular region at the higher values of ka. The reason for this lies, of course, in the Brewster angle "bite-out" that removes the reflected V-Pol field at angles commensurate with the rms slope angles (about 8°). Contributions to the total scattered field from this scattering mechanism would therefore tend to show, even at the higher grazing angles, a considerably smaller spread between the V-Pol and H-Pol returns than that predicted by the Bragg theory. This is just what is observed (see, e.g., Fig.15).

Unfortunately, there is no *a priori* basis for estimating the "slosh" dimensions required to obtain numerical values for the cross sections defined in (48) and (50) - they have never been measured (and those who have not observed natural water surfaces might question whether they even exist.) However, a small-scale "slosh" would probably, like most small-scale perturbations forced into being on a water surface, have the dimensions of waves at the minimum of the velocity/wavelength curve; that is, a couple of centimeters. Thus we will take a minimum value of the radius a to be 1 cm. Taking a minimum "dimple" diameter to be about 1 foot, we assign a least value for R to be 10 cm., placing the division between the perturbation and physical optics approximations (ka = 1) at the middle of the microwave region - C-Band (5 GHz, 6 cm). Thus for "sloshes" of this size, we will use (48) for S-Band and below, and (50) for X-Band and above. The result for low grazing angles ($< 5°$) is sketched in Fig. 27, where a wind speed of 15 kts is assumed, and the transition between the two approximations is drawn in as a smooth dashed line. For larger values of a the curves would move up, the transition point would occur at lower frequencies, and the polarization difference at a given frequency would decrease.

Although not yet established as a legitimate scattering obstacle, the existence of these "shocks" or "sloshes" would help explain certain puzzling aspects of low angle sea clutter, particularly small

amplitude "sea spikes." As noted earlier, the turbulent wind field of a 20″ fan blowing obliquely over a water filled basin in the laboratory and viewed with a high resolution horizontally polarized radar, produced a random sequence of sharp transient returns of significant amplitude [Hansen and Wetzel]. These returns could be visually correlated with the appearance of the type of micro-sloshes we have been discussing. In their behavior they were quite reminiscent of the "Sea Spikes" measured by Lewis and Olin [1980] in open water.

Figure 28 reproduces some low grazing angle (1.4°) X-band results obtained by Lewis and Olin [*loc. cit.*] under two quite different sea surface conditions. The records on the top were obtained from a "wind-blown sea with many whitecaps," while those below were characteristic of "calm" water. The general structure and temporal behavior of the returns for the two conditions are virtually identical, the only difference being a scale difference of 40 dB. Moreover, for each surface condition the V-Pol and H-Pol returns have the same amplitudes. The only two models that can account for comparable H-Pol and V-Pol returns are (1), the nose-on geometrical optics wedge model of Kalmykov and Pustovoytenko [*loc.cit.*] (see Fig. 19a), and (2), a Physical Optics model of some kind; either the glancing-incidence wedge model of section III.B.2.b.), or the "slosh" model being discussed here. Since model (1) is highly contrived and unrealistic, we are left with the latter choices as the most likely sources of low-angle transient returns. As Sherlock Holmes has said:

> "My dear Watson! When all possible explanations save one have been eliminated, that one, however unlikely it might seem, must contain the true solution."

Of course, we might not have exhausted "all possible explanations," but we have considered quite a few, and while the "slosh" hypothesis cannot fully account for the "calm water" returns observed by Lewis and Olin, it is the only model whose trends are all in the right directions.

*2. Sea Spikes and the "Plume" Model for Breaking Waves*

Certainly the most obvious place to look for scattering features in an active sea at low angles is at the peaks of breaking waves. But what are these scattering features? The peaks display different shapes according to which of the several types of breaker is involved (plunging, surging, spilling), and then there is turbulence, and spray. The orderly, serene models we have been discussing thus far apply to structures and surfaces that are hard to find in the chaos of a heavily breaking sea. Moreover, scattering from breakers is characterized by the appearance of "Sea Spikes" having cross sections several orders of magnitude greater than those predicted by any of the mechanisms discussed thus far. We have already seen "Sea Spikes" in the records collected by Lewis and Olin at the top of Fig. 28. Other investigators have observed them as well [Kalmykov and Pustovoytenko, *loc.cit.*; Long, 1975], and radar operators encounter them on a regular basis (hence their colloquial nomenclature.) Peak cross sections can range from 10-1000 $m^2$ for both polarizations, but these peaks occur sporadically, so the average cross section will be much smaller. Actually, when considering low angle cross sections generally, it is important to know how the quoted values of NRCS were obtained. Were they based on raw averages (including sea spikes), amplitude-limited data (chopping off the sea spikes), or selected data (removing data sections containing sea spikes)? Or were they averages at all, being instead defined as median cross sections? It is easy to infer from the breaking-wave records in Fig. 27 that, for this set of measurements at least, the mean "flux" of sea-spike events is roughly $0.001/m^2$-sec. Since the duration of the H-Pol sea spikes was roughly one second, and their mean amplitude about $5m^2$, this flux translates into a mean NRCS of about -23 dB, which is considerably greater than the low-angle results quoted earlier in section III.B.3. However, the NRL-4FR data are the median values of the NRCS, as were the values measured by Trizna [1987], so, unlike a mean value, the quoted NRCS levels would fail to reflect the contributions from the powerful sea spikes.

Cumulative distributions are much more informative, and Trizna has found them to reveal some interesting aspects of low angle backscatter. Figure 29 gives an example of how such distributions change with wind speed (X-band, H-Pol, upwind, about 5° grazing, wind speed increasing from left

to right). Clearly the statistical behavior is complex, and no single distribution tells the whole story. Trizna views the data in terms of multiple Weibull distributions, each characterizing the contributions from a particular class of scattering features. This approach in a way resembles that of the "Contaminated Normal" distribution used by Trunk [1976], in which the data are described by a series of normal distributions with different variances. The Weibull distribution is a generalization of the Rayleigh distribution, and, having two adjustable parameters, affords greater flexibility in fitting the data. The straight lines on Fig. 29 represent such "fits," the left hand (low wind) curve following a standard Rayleigh distribution over its entire length.

Trunk asserts that low angle, high resolution sea backscatter is not log-normal, as is sometimes stated, and indeed, the departures from Rayleigh seen with increasing wind in Fig. 29 are certainly not log-normal distributions, which would show long tails with the opposite curvature. In fact, those segments designated as "sea spike regions" appear to have relatively tighter distributions, as if sea spikes were produced by a special scattering mechanism quite different from that responsible for the main body of backscatter returns. Such a mechanism, based on a particular hydrodynamic model of a breaking wave, has been explored in some detail by Wetzel [1986]. We summarize some of its features below.

Although the word "breaker" usually summons up a mental image of a curled mass of crashing water (the "plunging" type), the breaking waves occuring in the open sea are generally of the "spilling" type, in which the interior crest angle at a wave peak sharpens to the point of instability ( 120°), and a series of water masses emitted at the crest slide down the front face of the wave under the force of gravity. Longuet-Higgins and Turner [1974] describe this process in their "plume" model of a spilling breaker, idealized in Fig. 30. The "plume" has a characteristic shape (sketched in Fig. 30a) and entrains air to form the "whitecap." The scattering model for these features resembles very closely the Physical Optics model for "sloshes" described above, the only differences being in the scale of the event and the range of expected local grazing angles.

The plumes emerge from the crest of the breaking wave, so initially the underlying wave face angle $\alpha$ will be steep - close to the value of 30° we have been using in other models for the crest peaks. The radius of the plume will be considerably larger than that of the "sloshes" discussed above, lying between 3 and 15 cm, just to take a wild guess, although one would expect the larger plumes to have rougher surfaces, thus reducing their resemblance to smooth cylinders - particularly at the higher frequencies. The toe length L over which the plume can be expected to resemble a cylindrical scatterer is another unknown, but we will assume it is of the order of a few plume diameters. Using (50) for the plume cross section, and the implications of Fig. 25 for the factor $F^2$, we find that these assumptions lead to individual plume cross sections lying between 0.25 - 25 $m^2$ for the popular X-band frequencies (k=2/cm). A breaking wave will generally emit several plumes, so if we assume that the cross sections combine incoherently, which is the worst case, we conclude that the "sea spikes" associated with a breaking wave could quite easily have cross sections lying in the range between 1 - 100 $m^2$. Interestingly, the range of cross sections measured by Lewis and Olin at the top of Fig. 28 was 1 - 10 $m^2$, while the "sea spike" regions in Trizna's cumulative distributions (Fig. 29) contained individual returns from the open ocean in excess of 100 $m^2$. Clearly, using dimensional parameters well within the realm of credibility, the "plume" model is capable of delivering "sea spike" cross sections in the amplitude range actually observed.

The polarization dependence of the plume cross sections can be inferred from the surface-proximity factors shown in Fig. 25. For the smaller plumes (e.g., ka=6) the H-Pol returns could exceed the V-Pol by almost 10dB close to the peak, but would decay rapidly as the plume slid down the wave face (toward decreasing local grazing angles), while the V-Pol return would increase. Since the acceleration of the plume down the wave face makes the local grazing angle a function of time, the temporal behavior of small sea spikes due to plumes should resemble that sketched in Fig. 31a. We see that the H-Pol returns are much "spikier," and associated with the wave peaks, while the V-Pol

returns are smoothly distributed over the length of the wave. This is just the kind of behavior often remarked upon by observers of low angle sea backscatter, particularly at grazing angles of several degrees (above the knee of the shadowing curve.) Corresponding behavior for the larger plumes (ka=20) is shown in Fig. 31b. Here the H-Pol and V-Pol returns oscillate out of phase, but with similar mean amplitudes, as the plume moves down the wave face.

Unfortunately, there is little reliable experimental evidence available which could either confirm or deny this scattering hypothesis. What evidence does exist is largely circumstantial: reasonable assumptions about plume dimensions yield observed scattering levels; the polarization dependence of plume scattering is consistent with observations; the range of oscillations in large-plume returns (Fig. 31b) is consistent with the width of the sea spike region at the higher windspeeds in Trizna's distribution functions (Fig. 29). Other evidence in support of the plume model may be found in the reference cited above. We conclude our discussion of the plume model with the following paragraph from that reference:

"We have found that one implication of the plume model - the existence of a curved scattering surface rising sharply out of the underlying wave surface - leads to radar scattering cross sections which, with a reasonable assumption of plume thickness, can be as large as those observed experimentally. We note, however, that the scattering results are based on two idealizing assumptions: (1) that the radar wavelength is of the order of [or less than] the plume thickness; (2) that the front surface of the plume is "smooth". As the radar wavelength increases, the scattering moves into the Rayleigh regime and falls off sharply with the fourth power of frequency. At lower frequencies, therefore, the plumes become invisible and our attention must shift to larger features, such as the wedgelike crest of the underlying wave. On the other hand, as the radar wavelength decreases, the roughness (see Fig. [30a]) over the scattering face of the plume can no longer be ignored, and the scattering amplitude must be multiplied by a roughness factor $\exp -2(k\sigma_r)^2$, where $\sigma_r$ is the rms roughness of the plume surface. Moreover, at short wavelengths, the likelihood of finding strong-scattering coherent segments along the plume front diminishes. It can be seen, therefore, that plume scattering of the type we have been discussing can occur only within a rather narrow window in the microwave spectrum, the location and width of this window being determined by unknown properties of the plumes, such as their thickness, shape, and roughness. Nevertheless, it is interesting and instructive to sketch the scattering behavior of a (reasonable?) plume having a thickness of 3 cm (about an inch) and an rms roughness of 10% of its thickness. Figure [32] places this behavior in the context of other scattering mechanisms that might be expected to play a role in microwave scattering from breaking waves. Although this breakdown into scattering domains is speculative, and dependent on as yet poorly understood breaker morphology, it has the virtue of differentiating between the kind of scattering one might expect at different frequencies, and guiding attention to the most appropriate model."

## IV. SUMMARY AND CONCLUSIONS

The first question to be asked in any discussion of low angle sea backscatter is how the radar sees the surface; that is, what is the nature of the shadowing process? Although all existing rough surface shadowing theories are based on geometrical optics, we approached the illumination problem through diffraction theory, with the result:

- The limits in windspeed/wavelength space of both Geometrical and Physical Optics (Fig. 5) established the operational conditions under which these approximations may be used with any confidence, while the estimated sensitivity of the diffraction model to radar polarization and wave crest irregularities and (Figs.3 and 7, respectively) was found to be sufficiently weak that simple two-dimensional physical optics should apply over a useful range of operating parameters.

For those operating parameters which allow use of the geometrical optics approximation, a "threshold" model for sea surface illumination applies at extreme grazing angles, providing a scattering field of isolated "islands" emerging from a dark background.

- Since the area and spacing of these scattering islands are functions of grazing angle and wind speed, we were able to define a new shadowing function for very low grazing angles (Fig. 14). The implications of this shadowing function were verified in a variety of experimental situations (Figs. 15-18).

Having identified, and given some quantitative measure of, the preferentially illuminated parts of the sea surface, it was possible to apply various scattering models to these regions.

- Bistatic scattering models were developed for both composite-surface Bragg scattering, and wedge scattering by the Method of Equivalent Currents and Physical Optics (Appendix).

- Using these models to define a low-angle NRCS produced values in reasonable agreement with experiment (section III.B.3), but also raised the curious suspicion that low angle scattering might be model-independent - especially curious in view of the almost diametrically opposite assumptions underlying the Bragg (small perturbation) and optical approximations.

- A new scattering feature - the "slosh" - was introduced, and described by a simple heuristic scattering model. Scattering by small "sloshes" would be expected to behave with time and polarization much like observed low angle, high resolution returns from calm water.

- The "plume" model of scattering from breaking waves seems able to account for many of the observed characteristics of the Sea Spikes that populate the low grazing angle clutter scene.

This report is intended to provide both a review and an extension of the state of our knowledge in the field of low angle sea scatter. But it would appear that we have come about as far as possible without more detailed knowledge of the surface features ultimately responsible for the scattered field. Although a "spectrum" has never been known to scatter an electromagnetic wave, models (like the Bragg model) that require only the specification of a spectrum have an easy time of it, since they need never know what the surface actually looks like. A spectrum is a highly averaged, fictitious entity in which all of the phases required to construct a real scattering surface are lost. In order to quantify "feature" scattering - from wedges, spray, sloshes, plumes, etc. - we must know their dimensions, lifetimes, distributions, etc. And since spectral theories cannot explain low angle sea scatter, the accumulation of this information must be the next order of business. The existing assortment of scattering theories and approximations should certainly suffice to produce acceptable levels of accuracy once the actual scattering obstacles are defined.

## REFERENCES


Barrick, D.E. and W.H. Peake (1967), "Scattering from surfaces with different roughness scales: analysis and interpretation," Rept. No. BAT-197A-10-3, Battelle Memorial Institute, Columbus, Ohio.

Bass, F.G. and I.M. Fuks (1964), "Calculation of shadowing for wave scattering from a statistical rough surface," Izv. vuzov. Radiofizika 7,101-112.

Beckmann, P. (1965), "Shadowing of random rough surfaces," IEEE Trans. Antennas Propagat., AP-13, 384-388.

Beckmann, P. and A. Spizzichino (1963), *The Scattering of Electromagnetic Waves from Rough Surfaces* (Macmillan, New York.)

Booker, H.G. and W.E. Gordon (1950), "A theory of radio scattering in the troposphere," Proc. IRE, 38, 401.

Chan, W.H.L. and H.F. Helmken (1983), "Low grazing angle radar back- scatter from the ocean surface," Rept. NWC TP 6450, Naval Weapons Center, China Lake, California.

Cox, C.S. and W.H. Munk (1954), "Statistics of the sea surface derived from sun glitter," J. Mar. Res., 13, 198-227.

Daley, J.C., Ransone, J.T., Burkett, J.A. and J.R. Duncan (1968), "Sea- clutter measurements on four frequencies," Report No. 6806, Naval Research Laboratory, Washington, D.C.

Deschamps, G.A., Boersma, J. and S.W. Lee (1984), "Three-dimensional half-plane diffraction: Exact solution and testing of uniform theories," IEEE Trans. Antennas Propagat., AP-32, 264-271.

Furutsu, K. (1966), "A statistical theory of ridge diffraction," Radio Sci., 1, 79-98.

Hunter, I.M. and T.B.A. Senior (1966), "Experimental studies of sea surface effects on low-angle radars," Proc. IEE, 113, 1731-1740.

Kalmykov, A.I., Kurekin, A.S., Lementa, Y.A., Ostrovskiy, I.Y. and V.V. Pustovoytenko (1976), "Scattering of microwave radiation by breaking sea waves," Gor'kiy Radiofiz., 19, 1315-1321 (translation).

Kalmykov, A.I., and V.V. Pustovoytenko (1976), "On polarization features of radio signals scattered from the sea surface at small grazing angles," J. Geophys. Res., 81, 1960-1964.

Katz, I. and L.M. Spetner (1960), "Polarization and depression angle dependence of radar terrain return," J. Res. NBS-D., 64-D, 483-486.

Katzin, M. (1957), "On the mechanisms of radar sea clutter," Proc. IRE, 45, 44-54

Keller, J.B. (1957), "Diffraction by an aperture," J. Appl. Phys., 28, 426-444.

Kerr, D.E. (ed.) (1951), *Propagation of Short Radio Waves*, Chapt. 6 (McGraw-Hill, New York).

Kinsman, B. (1965), *Wind Waves* (Prentice-Hall, Englewood Cliffs, N.J.).

Knott, E.F. and T.B.A. Senior (1974), "Comparison of three high- frequency diffraction techniques," Proc. IEEE, 62, 1468-1474.

Knott, E.F. (1985), "The relationship between Mitzner's ILDC and Michaeli's equivalent currents," IEEE Trans. Antennas Propagat., AP-33, 112-114.

Kwoh, D.S. and B.M. Lake (1984), "A deterministic, coherent, and dual- polarized laboratory study of microwave backscattering from water waves, Part I: Short gravity waves without wind," IEEE J. Ocean. Engin., OE-9, 291-308.

Leader, J.C. (1971), "The relationship between the Kirchoff approach and small perturbation analysis in rough surface scattering theory," IEEE Trans. Antennas Propagat., AP-19, 786-788.

Lewis, B.L. and I.D. Olin (1980), "Experimental study and theoretical model of high resolution backscatter from the sea," Radio Sci., 15, 815-826.

Lighthill, M.M. (1978), *Waves in Fluids*, (Bantam Press, New York.)

Long, M.W. (1975), *Radar Reflectivity of Land and Sea*, (Heath, Boston).

Longuet-Higgins, M.S. and J.S.Turner (1974), "An entraining plume model of a spilling breaker," J. Fluid Mech., 63, 1-20.

Lynch, P. and R.J. Wagner (1970), "Rough surface scattering: shadowing, multiple scatter, and energy conservation," J. Math. Phys., 11, 3032-3042.

Lyzenga, D.R., A.L. Maffett and R.A. Shuchman (1983), "The contribution of wedge scattering to the radar cross section of the ocean surface," IEEE Trans. Geosci. Remote Sens., GE-31, 502-505.

Michaeli, A. (1984), "Equivalent edge currents for arbitrary aspects of observation," IEEE Trans. Antennas Propagat., AP-32, 252-258.

Middleton, D. and R..H. Mellen (1985), "Wind-generated solitons: A potentially significant mechanism in ocean surface wave generation and surface scattering," IEEE J. Ocean Eng., OE-10, 471-476.

Middleton, D. (1986), "A proposed soliton mechanism in wind-wave surface generation and scattering," NUSC Tech. Rept. 7775, 19 Dec. 1986, Naval Underwater Systems Center, Newport/New London.

Phillips, O.M. (1966), *The Dynamics of the Upper Ocean*, (Cambridge University Press, Cambridge.)

Phillips, O.M. (1985), "Spectral characteristics of breaking waves" *The Ocean Surface, Wave Breaking, Turbulent Mixing and Radio Probing*, Y. Toba, H. Mitsuyasu, eds., (D.Reidel Publishing Co.,Boston).

Pierson, W.J. Jr. and M.A. Donelan (1987), "Radar-scattering and equilibrium ranges in wind generated waves with application to scatterometry," *J. Geophys. Res.*, **92** (C5), 4971-5029.

Plonus, M.A., Williams, R. and S.C.H. Wang (1978), "Radar cross section of curved plates using geometrical and physical diffraction techniques," IEEE Trans. Antennas Propagat., AP-26, 488-493.

Rice, S.O. (1951), "Reflection of electromagnetic waves from slightly rough surfaces," Commun. Pure Appl. Math, 4, 361-378.

Sancer, M.I. (1969), "Shadow-corrected electromagnetic scattering from a randomly rough surface," IEEE Trans. Antennas Propagat., AP-17, 577-585.

Saxton, J.A. and J.A. Lane (1952), "Electrical properties of sea water," Wireless Engineer, 29, 269-275.

Sikta, F.A., Burnside, W.D., Chu, T.T. and L. Peters, Jr. (1983), "First - order equivalent current and corner diffraction scattering from flat plate structures," IEEE Trans. Antennas Propagat., AD-31, 584.

Sittrop, H. (1974), "X- and Ku-band radar backscatter characteristics of sea clutter," Proc. of the URSI Comm.II Specialist Meeting on Microwave Scattering and Emission from the Earth, (E.Schanda,Ed.), Berne, Switzerland.

Smith, B.G. (1967), "Geometrical shadowing of a random rough surface," IEEE Trans. Antennas Propagat., AP-15, 668-671.

Sommerfeld, A. (1896), "Mathematische theorie der diffraktion," Math. Ann., 47, 317-374.

Trizna, D. (1987), "Measurement and interpretation of North Atlantic ocean marine radar sea scatter," NRL Report (to be published).

Trunk, G.V. (1976), "Non-Rayleigh Sea Clutter: Properties and Detection of Targets," NRL Report No. 7986, June 25, 1976.

Ufimtsev, P.I. (1957), "Approximate computation of the diffraction of plane electromagnetic waves at certain metal boundaries: I. Diffraction patterns at a wedge and a ribbon," Soviet Physics: Tech. Phys., 3, 1708-1718.

Valenzuela, G.R. (1978), "Theories for the interaction of electromag-netic and ocean waves-a review," Boundary-Layer Meteor., 13, 61-85.

Wagner, R.J. (1967), "Shadowing of randomly rough surfaces," J. Acoust. Soc. Amer., 41, 138-147.

Wait, J.R. and A.M. Conda (1959), "Diffraction of electromagnetic waves by smooth obstacles for grazing angles," J. Res. NBS-D. Rad. Prop., 63D, 181-197.

Wetzel, L.B. (1977), "A model for sea backscatter intermittency at extreme grazing angles," Radio Sci., 12, 749-756.

Wetzel, L.B. (1986a), "A minimalist approach to sea backscatter - the wedge model," URSI Open Symposium on Wave Propagation: Remote Sensing and Communication, July 28-Aug 1, 1986, Durham, N.H., Pre-Print Vol. pp. 3.1.1-3.1.4.

Wetzel, L.B. (1986b), "On microwave scattering by breaking waves," *Wave Dynamics and Radio Probing of the Ocean Surface*, O.M. Phillips and K. Hasselmann, eds., pp.273-284 (Plenum Press, New York).

Wetzel, L.B. (1987), "On the theory of electromagnetic scattering by a raindrop splash," NRL Memorandum Report No. 6103, September 1987.

Wright, J.W. (1966), "Backscatter from capillary waves with application to sea clutter," IEEE Trans. Antennas Propagat., AP-14, 749-754.

## Appendix

## SCATTERING FORMULARY

*1. A Composite-Surface Bragg Model for Bistatic Scattering*

Consider a surface element A with orientation defined by its normal $\hat{n}$, illuminated from direction $\hat{k}_i$ and scattering into direction $\hat{k}_s$, as in the Fig. A1.

The incident vector $\hat{k}_i$ is assumed to lie in the y-z plane with grazing angle $\psi_i''$, while the scattering vector $\hat{k}_s$ is defined by grazing angle $\psi_s''$ and azimuth (or scattering) angle $\phi_s$. The normal $\hat{n}$ is defined by its inclination $\theta$ and azimuth angle $\phi$. In terms of the fixed x-y-z coordinate system,

$$\hat{n} = \sin\theta\sin\phi\,\hat{x} + \sin\theta\cos\phi\,\hat{y} + \cos\theta\,\hat{z} \tag{A1}$$

$$\hat{k}_i = 0\,\hat{x} + \cos\psi_i''\,\hat{y} - \sin\psi_i''\,\hat{z} \tag{A2}$$

$$\hat{k}_s = \cos\psi_s''\sin\phi_s\,\hat{x} + \cos\psi_s''\cos\phi_s\,\hat{y} + \sin\psi_s''\,\hat{z} \tag{A3}$$

Scattering from A depends on the *local* grazing angles $\psi_i$ and $\psi_s$ relative to the surface A. These angles are given by

$$\sin\psi_i = -\hat{n}\cdot\hat{k}_i = -\sin\theta\cos\psi_i''\cos\phi - \sin\psi_i''\cos\phi \tag{A4}$$

$$\sin\psi_s = +\hat{n}\cdot\hat{k}_s = \sin\theta\cos\psi_s''\cos(\phi - \phi_s) + \sin\psi_s''\cos\theta \tag{A5}$$

For a coordinate system *on the scattering patch A*, the bistatic cross section per unit area is given by Barrick and Peake [1967] in the form

$$\sigma_{pp}^{o}(\psi_s, \phi_s) = 4\pi k_o^4 \sin^2\psi_i \sin^2\psi_s \,|\,\alpha_{pp}\,|^2\, W(K_1, K_2) \tag{A6}$$

where $k_o$ is the radar wavenumber, and pp denotes the polarization (i.e., pp = HH or VV). The surface wave vector components are given by

$$K_1 = k_o(\cos\psi_s\cos\phi_s - \cos\psi_i) \tag{A7}_1$$

$$K_2 = k_o\cos\psi_s\sin\phi_s \tag{A7}_2$$

and the coefficients $\alpha_{pp}$ are complicated functions of the angles above and the electrical properties of the scattering surface. They are given approximately by

$$\alpha_{HH} = -\cos\phi_s \tag{A8}$$

$$\alpha_{VV} = (\cos\psi_i \cos\psi_s - \cos\phi_s)/(\sin\psi_i + \sqrt{\epsilon}) (\sin\psi_s + \sqrt{\epsilon}) \quad \text{(A9)}$$

where $\epsilon$ is the dielectric constant of the surface (about 50 for sea water at microwave frequencies.)

However, the *local* components of the incident and scattered field vectors on A are generally different from those defined in the radar reference system. That is, a rotation of $\hat{n}$ out of the plane of incidence will convert an initial horizontal or vertical polarization into a mixture of horizontally and vertically polarized components on A. In Fig. A2 we represent the incident and scattered field vectors in the radar reference system (x,y,z) as $\vec{E}_V$ and $\vec{E}_H$, and the tilted, rotated surface element A as described by its normal $\hat{n}$.

The transformation of the incident fields to the surface A where the scattering actually takes place is provided by the following vector relationships (p denotes the polarization, H or V):

"Vertical" component on A due to the incident fields:

$$\vec{E}_{VP}^{Ai} = (\hat{n} \cdot \vec{E}_p^i)\hat{n} \quad \text{(A10)}$$

"Horizontal" component on A due to the incident fields:

$$\vec{E}_{HP}^{Ai} = (\hat{n} \times \vec{E}_p^i) \times \hat{n} \quad \text{(A11)}$$

The *local* scattered fields for these two polarizations are proportional to the angular coefficients in (A8) and (A9), so we write:

$$\vec{E}_{HP}^{As} \sim \vec{E}_{HP}^{Ai} \cdot \alpha_{HH} ; \quad \vec{E}_{VP}^{As} \sim \vec{E}_{VP}^{Ai} \cdot \alpha_{VV} \quad \text{(A12)}$$

Finally, the scattered field in the *radar* reference frame is found from the component of (A12) in the scattered field directions (denoted by a carat) defined in Fig. A2.

$$E_p^s \sim |E_p^i| \{(\hat{n} \cdot \vec{E}_p^i)\hat{n}\,\alpha_{VV} + (\hat{n} \times \vec{E}_p^i) \times \hat{n}\,\alpha_{HH}\} \cdot \hat{E}_p^s . \quad \text{(A13)}$$

Note that cross-polarized terms, which we ignore here, could also be obtained from this formalism.

The angular factors $|\alpha_{pp}|^2$ in (6) were originally obtained from the square of the ratio of scattered to incident field strengths, so we will replace them in our composite-surface bistatic model with the corresponding expressions formed from (A13):

$$|\alpha_{pp}|^2 \rightarrow |\{(\hat{n} \cdot \vec{E}_p^i)\hat{n}\,\alpha_{VV} + (\hat{n} \times \vec{E}_p^i) \times \hat{n}\,\alpha_{HH}\} \cdot \hat{E}_p^s|^2 . \quad \text{(A14)}$$

A similar expression was obtained by Valenzuela [1968] for the monostatic (backscatter) case, which is often used as the current "Two-scale" or "Composite-Surface" Bragg model for radar backscatter from the sea (for a recent application see Pierson and Donelan, 1987.)

Finally, we assume that the wave spectrum W in (A8) is isotropic at the Bragg resonant wavenumber, so is a function only of

$$K = (K_1^2 + K_2^2)^{1/2} = 2k_o \cos\psi_i \sin(\phi_s/2) \quad \text{(A15)}$$

Using the Phillips [1966] spectrum for W( ):

$$W(K) = 0.005K^{-4}, \tag{A16}$$

equation (A6) reduces to

$$\sigma_p^o(\phi, \phi_s) = 1.6 \times 10^{-5} \frac{\sin^2\psi_i \sin^2\psi_s}{\sin^4(\phi_s/2)} \mid \alpha_{pp} \mid^2. \tag{A17}$$

The grazing angles are defined in (A4) and (A5), and the angular factor $\mid \alpha_{pp} \mid^2$ defined in (A14) is assembled with the help of (A1), (A8), and (A9).

Keeping all of the angles straight in a completely general formulation of bistatic scattering in the small-amplitude Bragg approximation is a real nightmare, so when using these expressions for examples in section II.A.1. we will introduce some rational simplifications. For example, the surface slope angle will be taken as 30°, which is the limiting angle for surface stability and thus quite likely to be encountered close to the wave peaks. The radar-referenced grazing angles $\psi_i^o$ and $\psi_s^o$ will be very much smaller than 30°, so we will take them both to be vanishingly small. The *local* grazing angles given in (A4) and (A5) will be approximated by the first terms in those expressions, noting, however, that these terms contain the cosine of the azimuthal angles, so they will vanish for values of these angles at the extremes of the allowed range of $\phi_s$. Even with these simplifications, the expressions are sufficiently complex that little would be gained by displaying them here. The reader is invited to reproduce them, if he wishes, from the recipe given above.

*2. Bistatic Wedge Scattering by the MEC*

Consider a wedge of length L and interior angle $\alpha$ with its edge lying in direction $\hat{t}$ in the x-y plane. The incident and scattering directions are indicated by $\hat{k}_i$ and $\hat{k}_s$ respectively:

As in the previous case, we assume that the grazing angles $\psi_i^o$ and $\psi_s^o$ are so much smaller than the wedge face angle $(\pi - \alpha)/2$ that they can be ignored. All of the angles then lie in the x-y plane.

In the Method of Equivalent Currents (MEC) as described by Knott and Senior [1974], the scattered field is expressed as an integral over a fictitious filamentary current laid along the edge C of the wedge, where this "equivalent current" is of just such a form as to reproduce the results of the Geometrical Theory of Diffraction (GTD) in those special directions allowed by the GTD, and to produce a fictitious scattered field in all other directions. It is taken as an article of faith that the fields so defined represent a generalization of the GTD fields, and have some relation to reality. The fictitious currents are themselves non-physical and non-causal, since they depend upon the direction from which the edge is observed - i.e., on the location of the observer. (This is a marvelous example of *teleology*, where the unknowable end configures the means to that end.) The scattered field defined by this method is given by the expression:

$$E_s(L; \phi, \phi_s) = \frac{E_o e^{ikR}}{2\pi R} \int_C \frac{e_{ti} e_{st}(X - Y) + h_{ti} h_{st}(X + Y)}{\sin\beta_i \sin\beta_s} e^{ikw(\hat{t} \cdot (\hat{k}_i - \hat{k}_s))} dw \tag{A18}$$

where X and Y are the GTD diffraction coefficients,

$$(X, Y) = \frac{\sin(\pi/n)}{n} \left[ \frac{1}{\cos(\pi/n) - \cos(\gamma_s - \gamma_i)/n} \pm \frac{1}{\cos(\pi/n) - \cos(\gamma_s + \gamma_i)/n} \right] \tag{A19}$$

In (A18), the coefficients $e_{it,st}$ and $h_{it,st}$ are the components of the incident (i) and scattered (s) electric and magnetic fields along the direction of the edge ($\hat{t}$); the rest of the angles are defined in Fig. A3. In (A19), $n = 2 - \alpha/\pi$, and the angles $\gamma_{i,s}$ are the incident and scattered angles measured from the common wedge face in a plane *perpendicular* to the edge, so at very low grazing angles they are both approximately equal to the wedge face slope angle $(\pi - \alpha)/2$. For Vertical polarization, the e's vanish, and the remaining h's cancel the sines in the denominator of (A18); for Horizontal polarization, the h's vanish and the e's cancel the sines. This leaves an elementary sinx/x integral in (A18), and the scattered field reduces to the simple form:

$$E_{H,V}(L; \phi_w, \phi_w) = E_o \frac{e^{ikR}}{2\pi R} (X \mp Y) \cdot L \cdot sinc \left[ \frac{1}{2} kL (\cos \phi_w - \cos (\phi_s - \phi_w)) \right] \tag{A20}$$

where the - and + signs are used for H- and V-polarization, respectively. Using the low grazing angle simplification indicated above for $(X \pm Y)$, and defining cross section in the usual way, $[\sigma = (4\pi R^2) |E_s/E_o|^2]$, the bistatic cross section for a wedge of length L and edge orientation angle $\phi_w$ becomes

$$\sigma_{H,V}(L; \phi_w, \phi_s) = C_{h,v} L^2 sinc^2 \left[ \frac{1}{2} kL (\cos \phi_w - \cos (\phi_s - \phi_w)) \right] . \tag{A21}$$

For our standard stability-limited wedge angle of 120°, the polarization coefficients have the numerical values

$$C_H = -29 \text{ dB}, \quad C_V = -8 \text{ dB}. \tag{A22}$$

*3. Perturbation Theory for Discrete Scattering Features*

There is an interesting, and often overlooked, difference between the Rayleigh/Rice perturbation approximation [Rice, 1951], on which the cross section in (A6) is based, and the scattering integral approach used by Wright [1966]. In the latter, the cross section is expressed in terms of an integral over the surface perturbation, much as in a small amplitude physical optics approximation, but with the boundary conditions treated somewhat differently in order to provide the polarization dependence often missing in P.O. calculations (however, see Leader, 1971). Wright's result takes the form of the cross section of a deterministic perturbation (x,y) over a flat surface:

$$\sigma_{V,H}(\psi) = \frac{4k^4}{\pi} |g_{V,H}(\psi)|^2 \left| \int_S \int \xi(x,y) e^{i2h\cos\psi \cdot x} dxdy \right|^2 \tag{A23}$$

where the angle coefficients may be written in the form [Valenzuela, 1978],

$$\xi_V = \frac{(\epsilon - 1)[\epsilon(1 + \cos^2\psi) - \cos^2\psi]\sin^2\psi}{[\epsilon \sin\psi + (\epsilon - \cos^2\psi)^{1/2}]^2} , \tag{A24}$$

$$\xi_H = \frac{(\epsilon - 1)\sin^2\psi}{[\sin\psi + (\epsilon - \cos^2\psi)^{1/2}]^2} \tag{A25}$$

Fig. A1

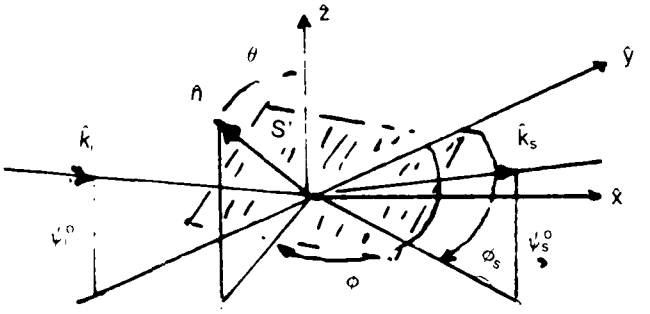


Fig. A2

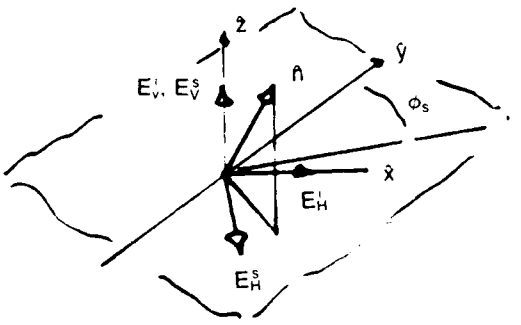


Fig. A3

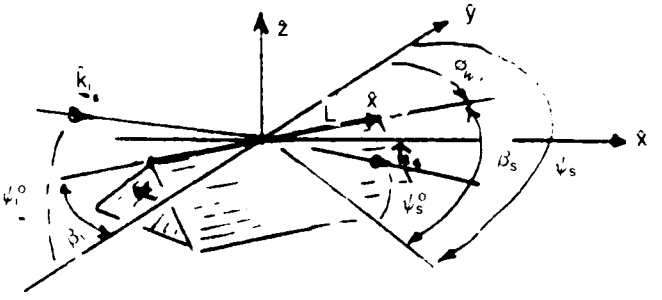

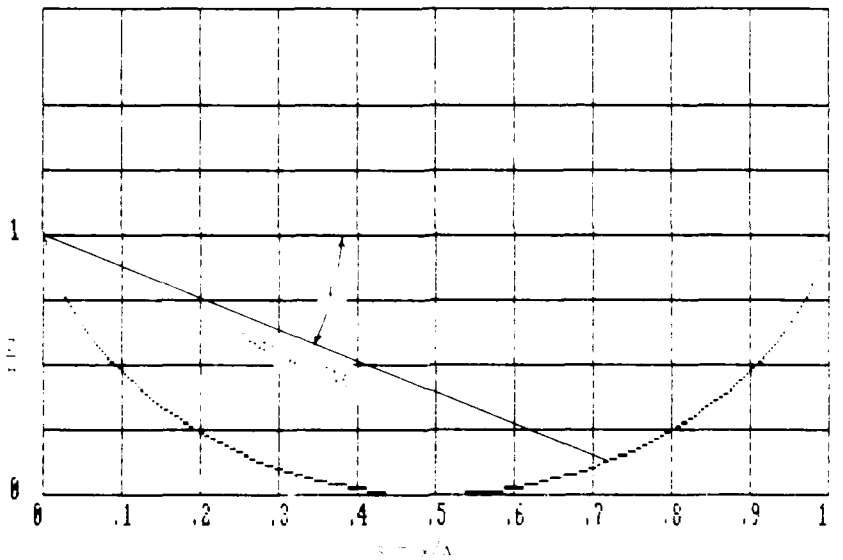


Fig. 1 — Trochoidal Wave with Shadow Line for Grazing Angle $\psi$

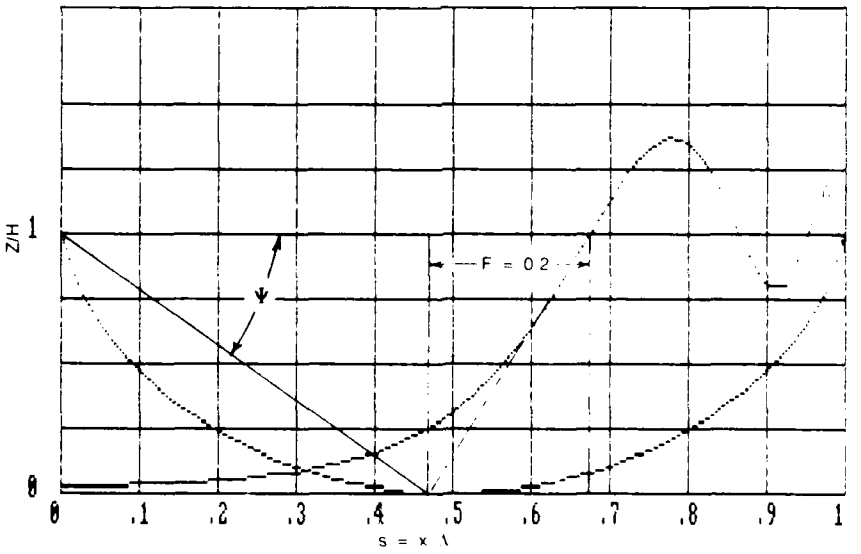


Fig. 2 — Diffraction Pattern and "Transition Fraction" for a Trochoidal Wave: X-band, 3° grazing, 15 kt wind

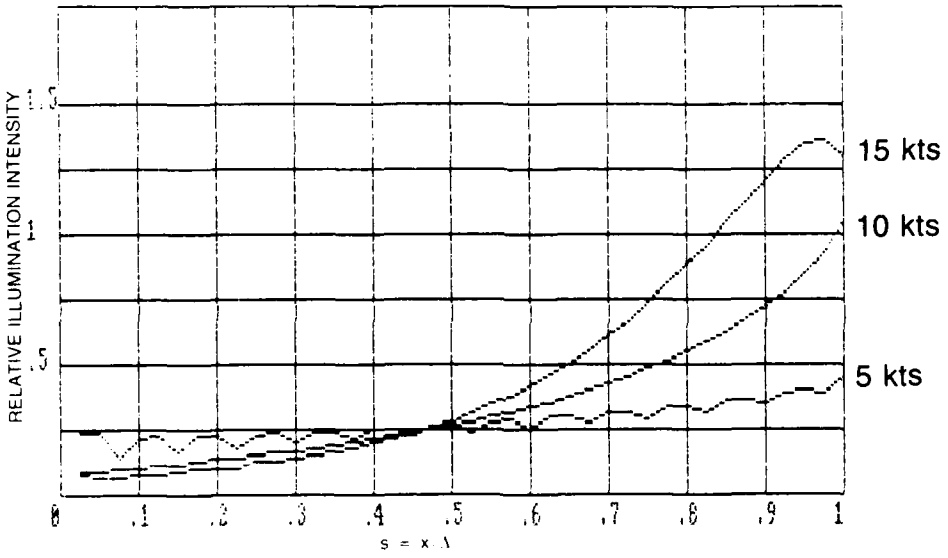


Fig. 3 — Effect of Polarization: L-Band, 3° grazing, 5, 15, 25 kt winds

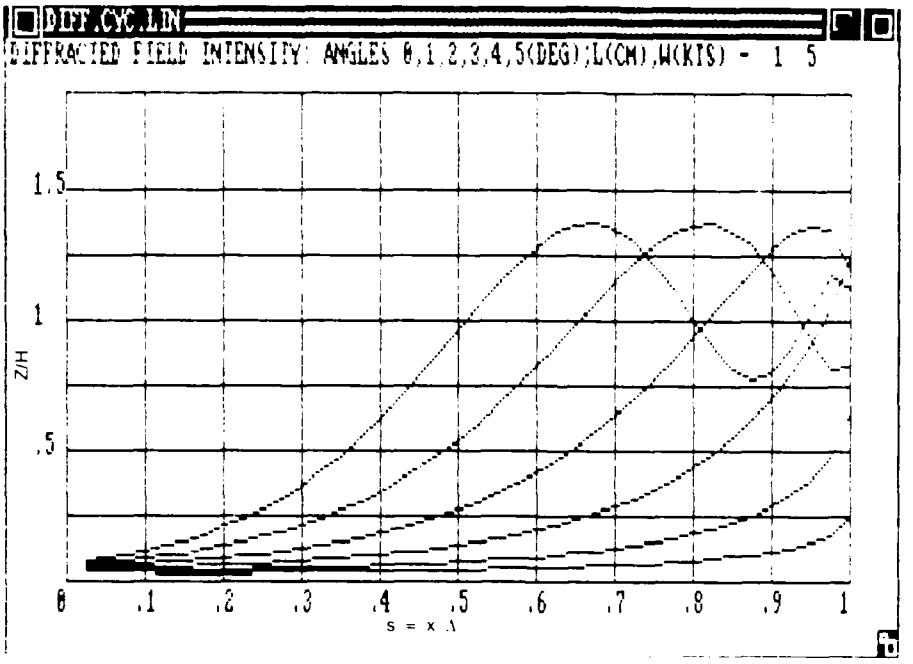


(a)

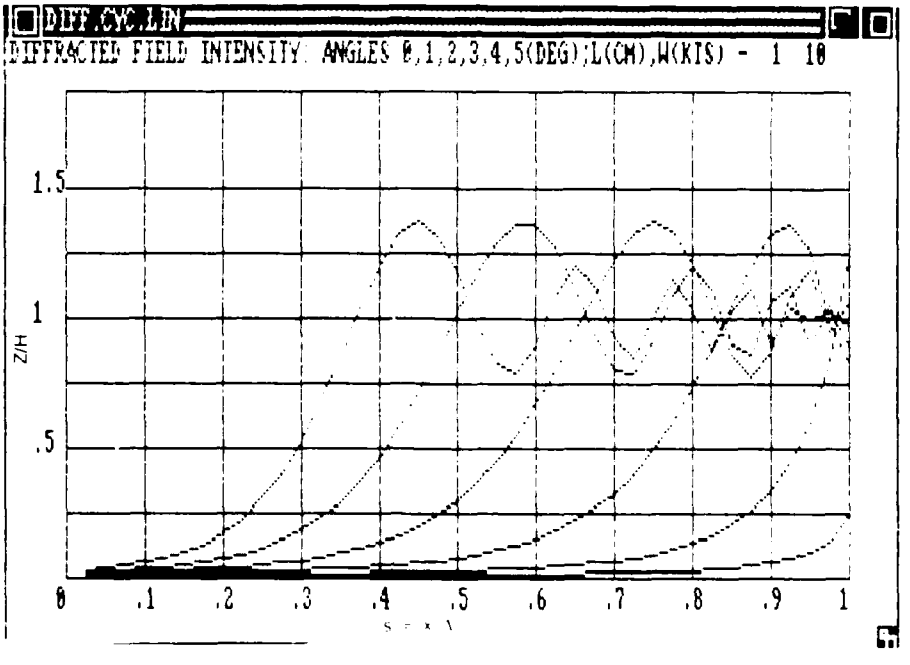


(b)

Fig. 4a-b — Diffraction Patterns for 1 - 100 cm wavelengths

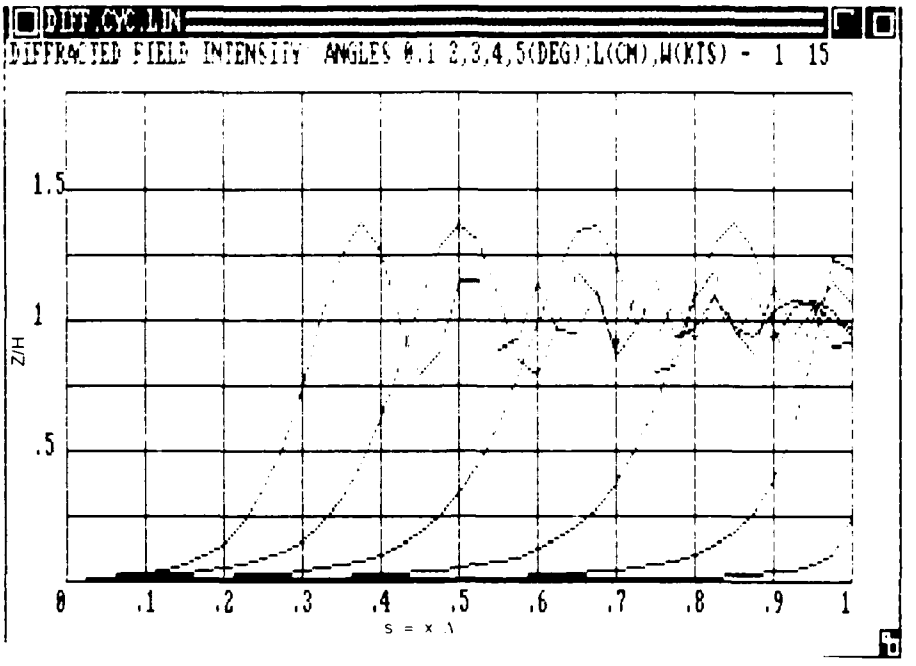


(c)

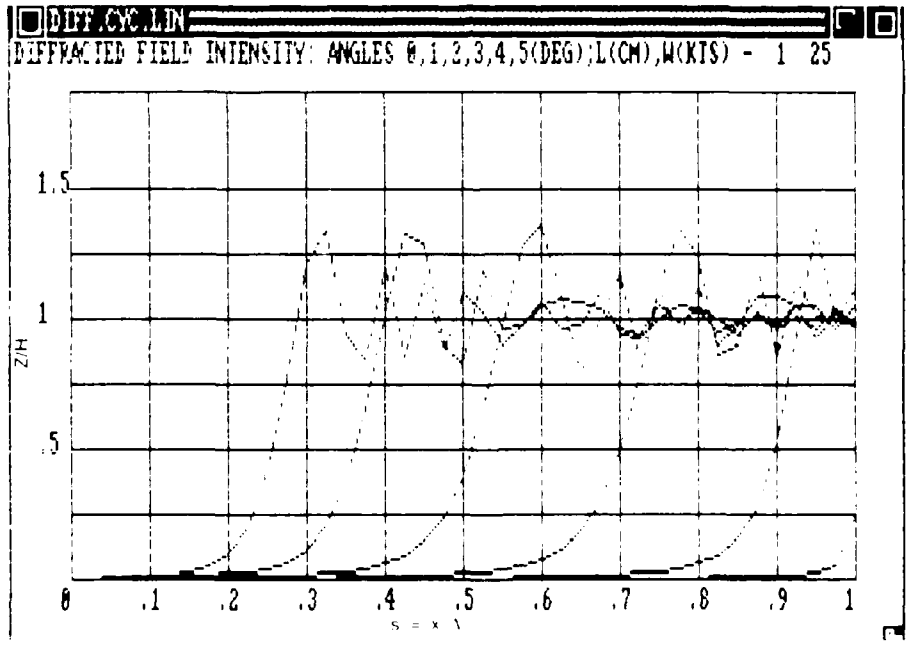


(d)

Fig. 4c-d — Diffraction Patterns for 1 - 100 cm wavelengths

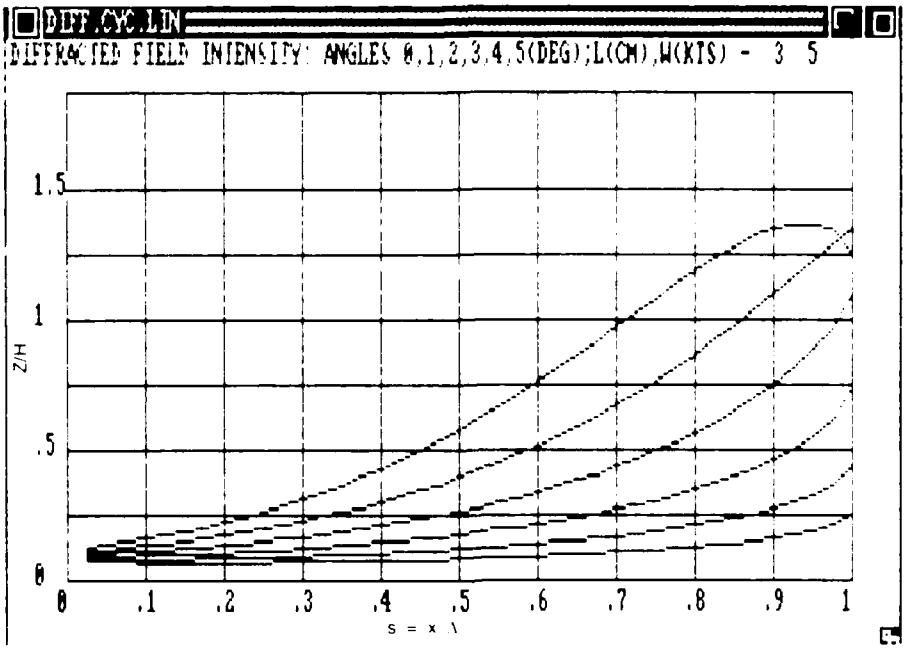


(e)

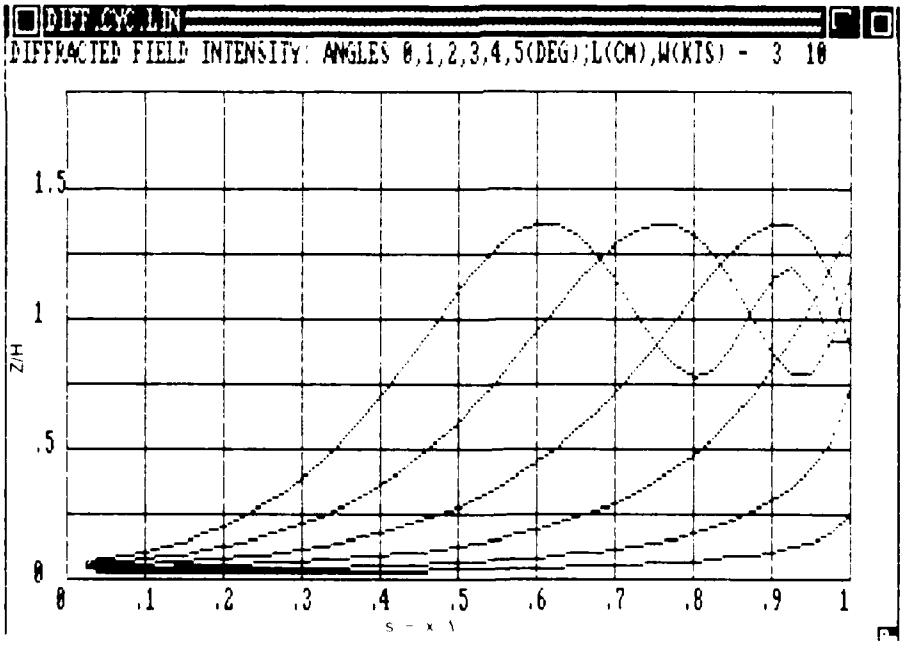


(f)

Fig. 4e-f — Diffraction Patterns for 1 - 100 cm wavelengths

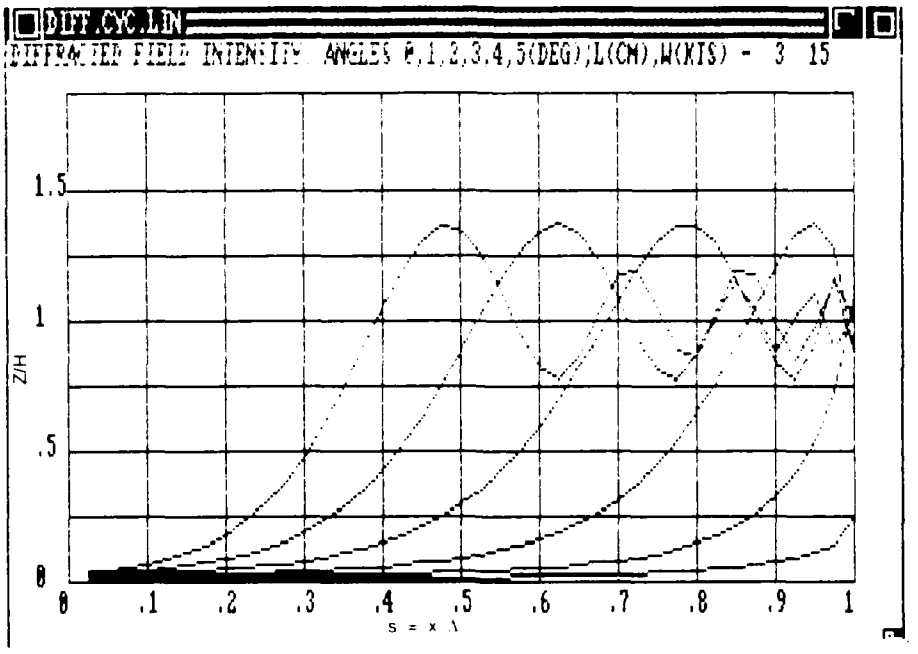


(g)

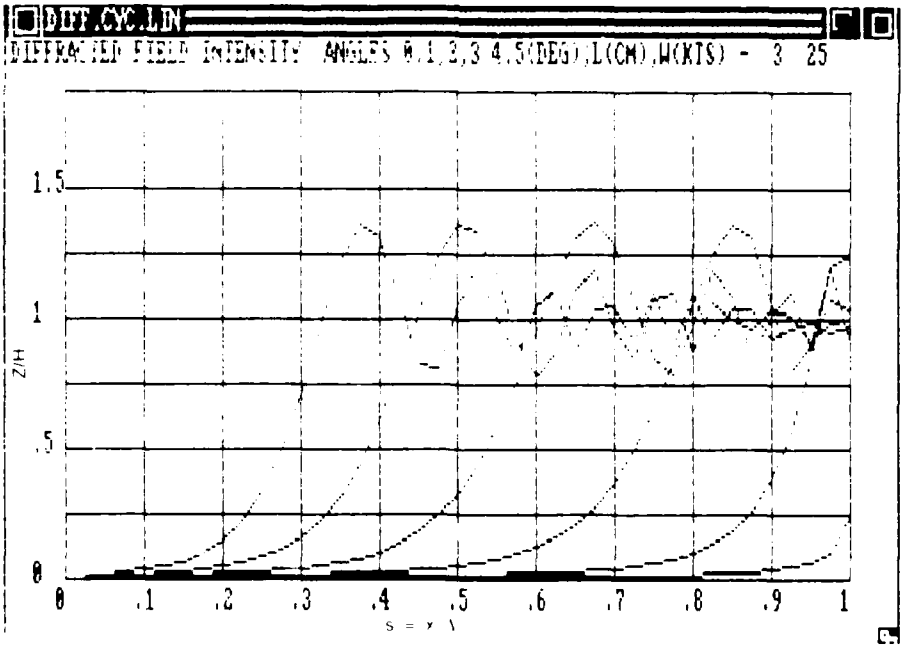


(h)

Fig. 4g-h — Diffraction Patterns for 1 - 100 cm wavelengths

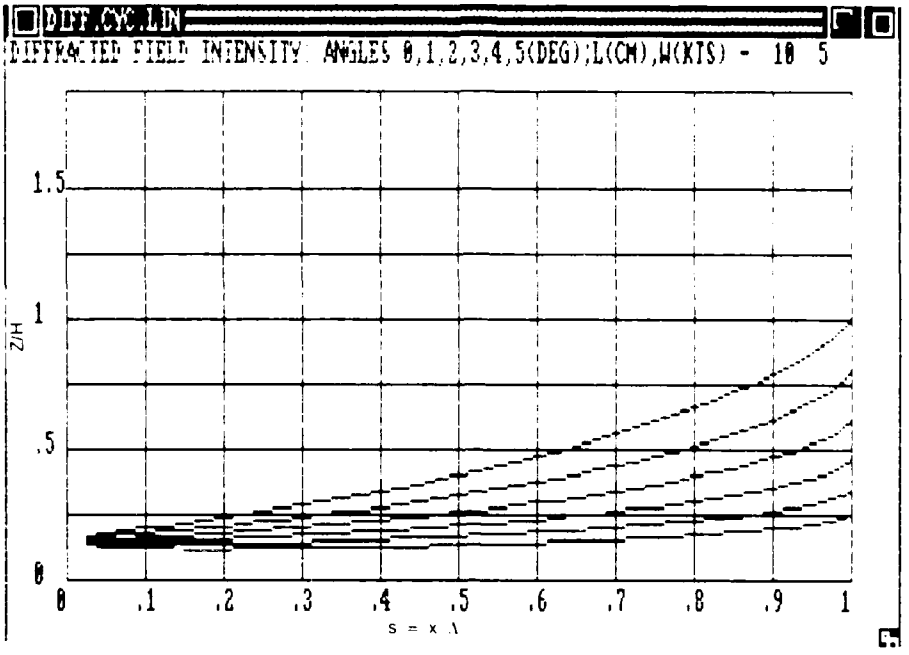


(i)

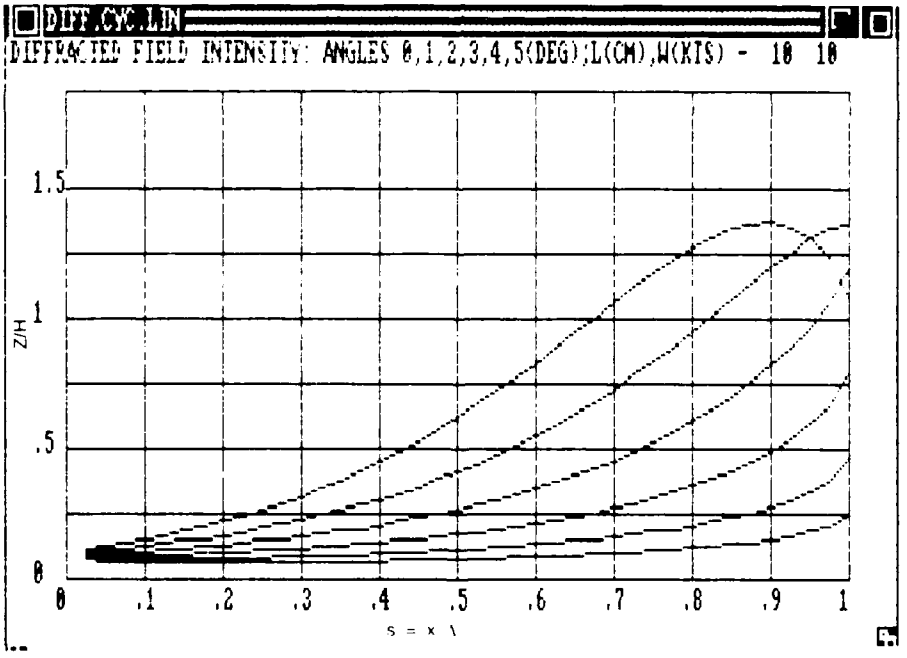


(j)

Fig. 4i-j — Diffraction Patterns for 1 - 100 cm wavelengths

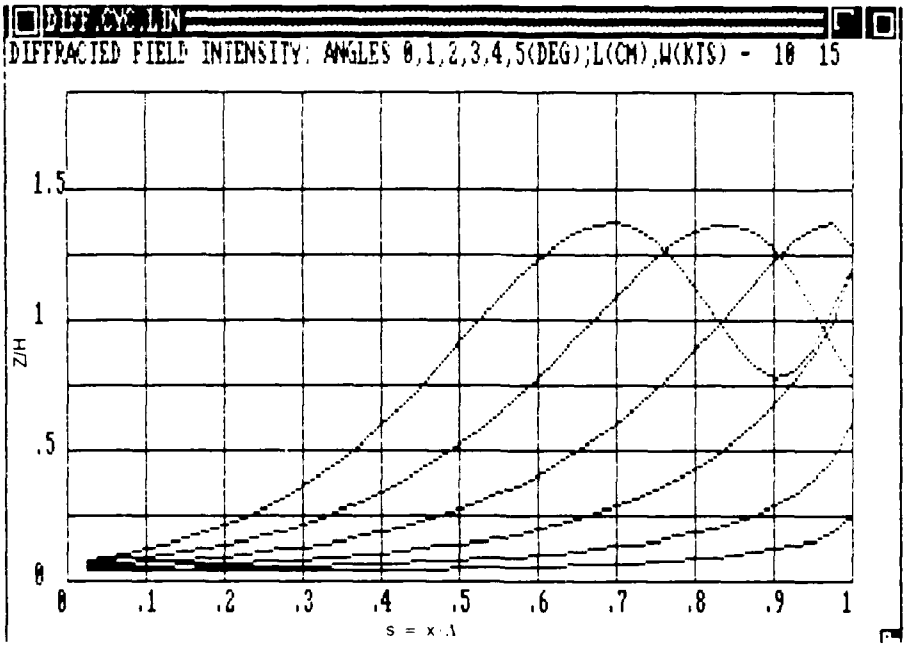


(k)

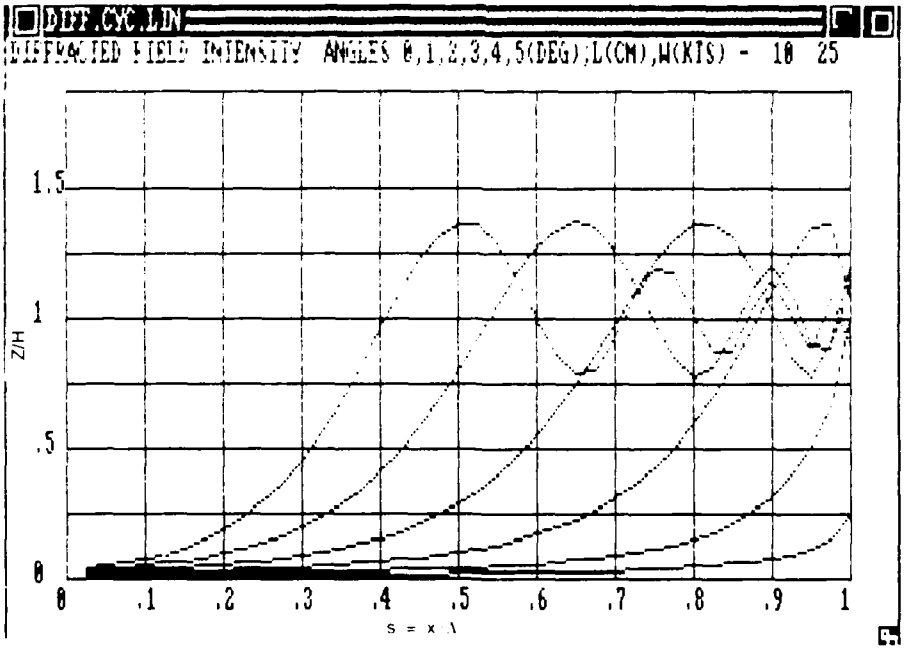


(l)

Fig. 4k-l — Diffraction Patterns for 1 - 100 cm wavelengths

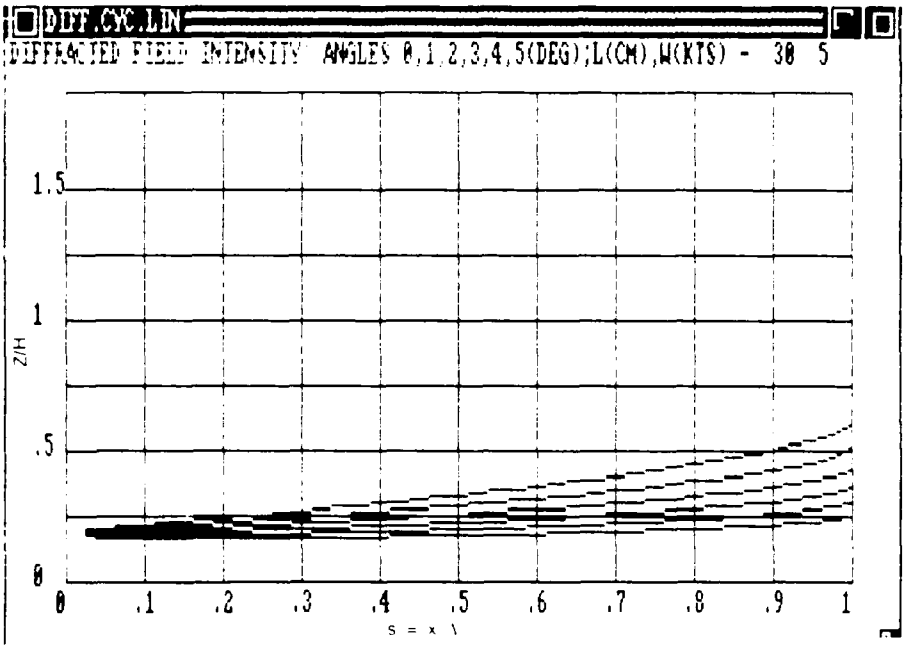


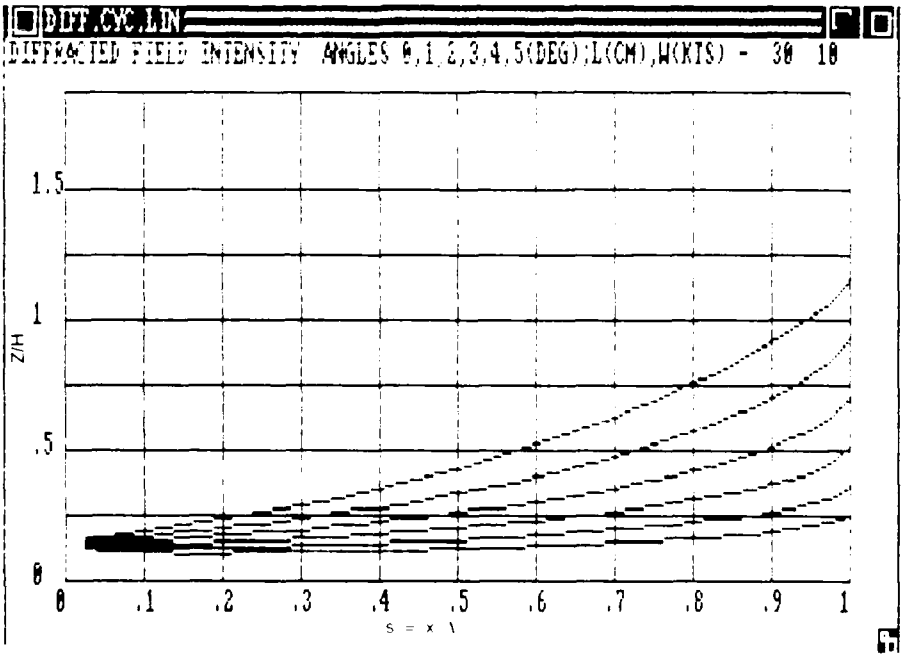


Fig. 4m-n — Diffraction Patterns for 1 - 100 cm wavelengths

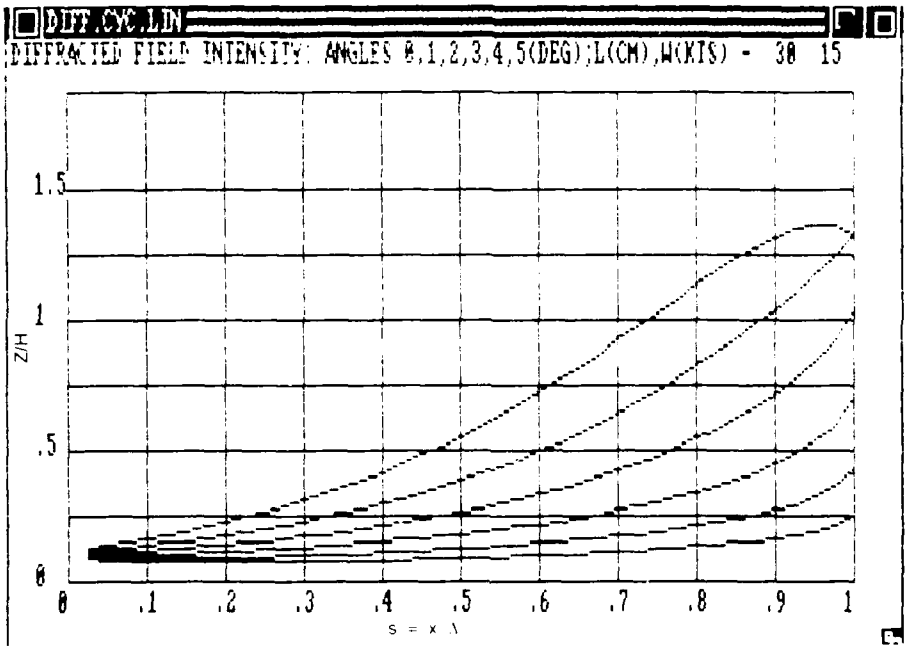


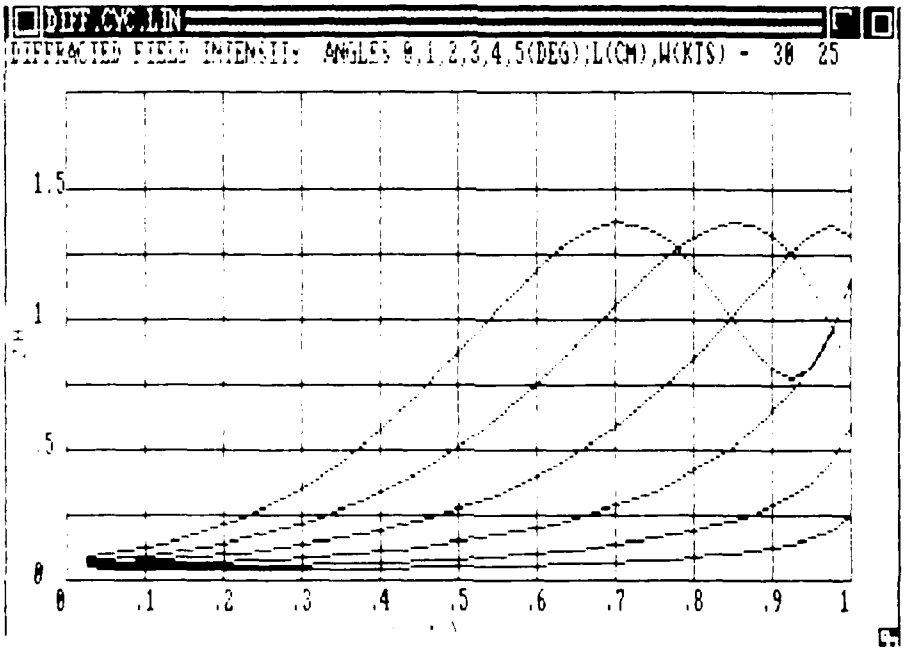


Fig. 4o-p – Diffraction Patterns for 1 - 100 cm wavelengths

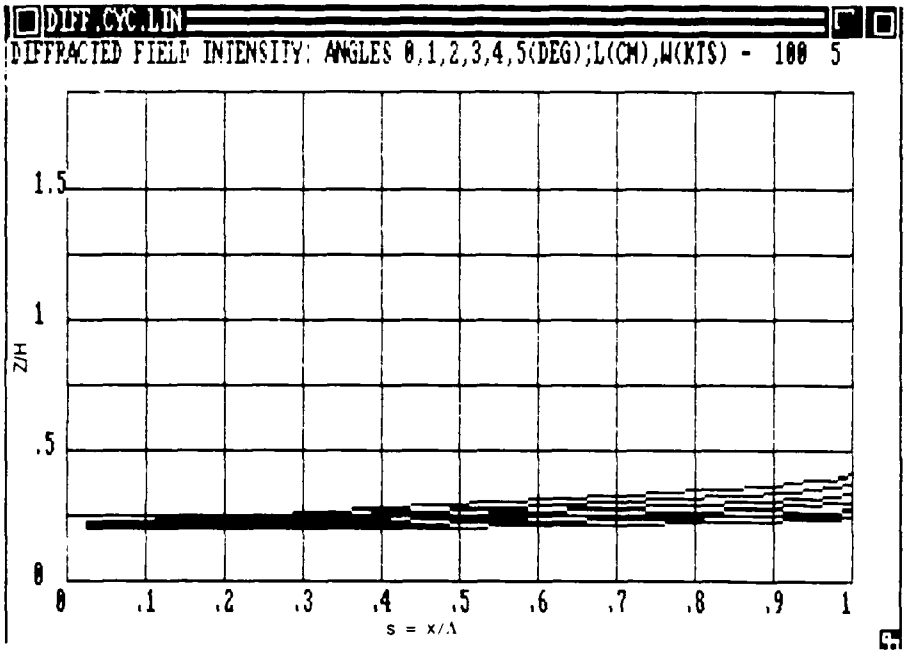


(q)

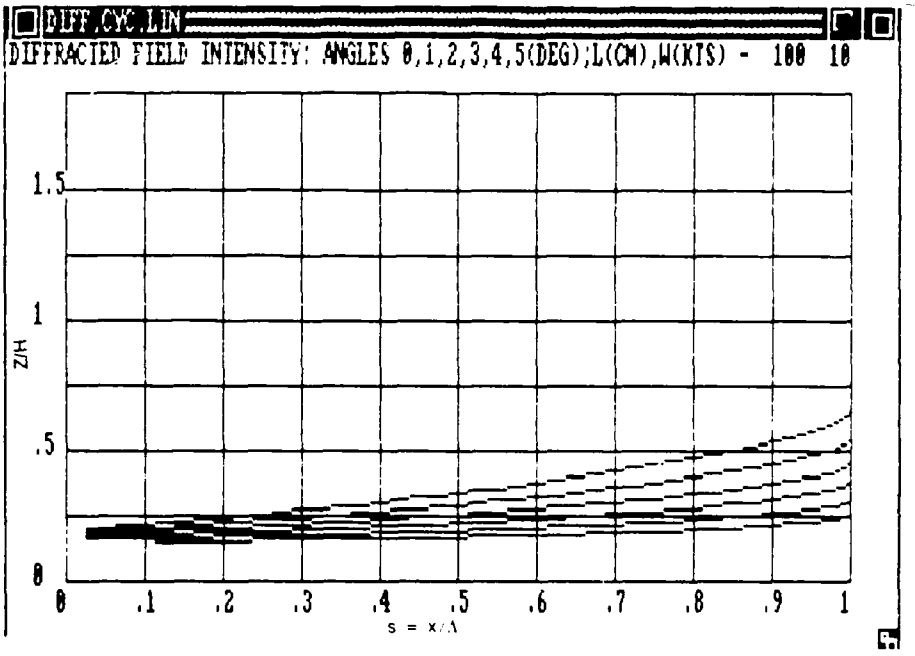


(r)

Fig. 4q-r — Diffraction Patterns for 1 - 100 cm wavelengths

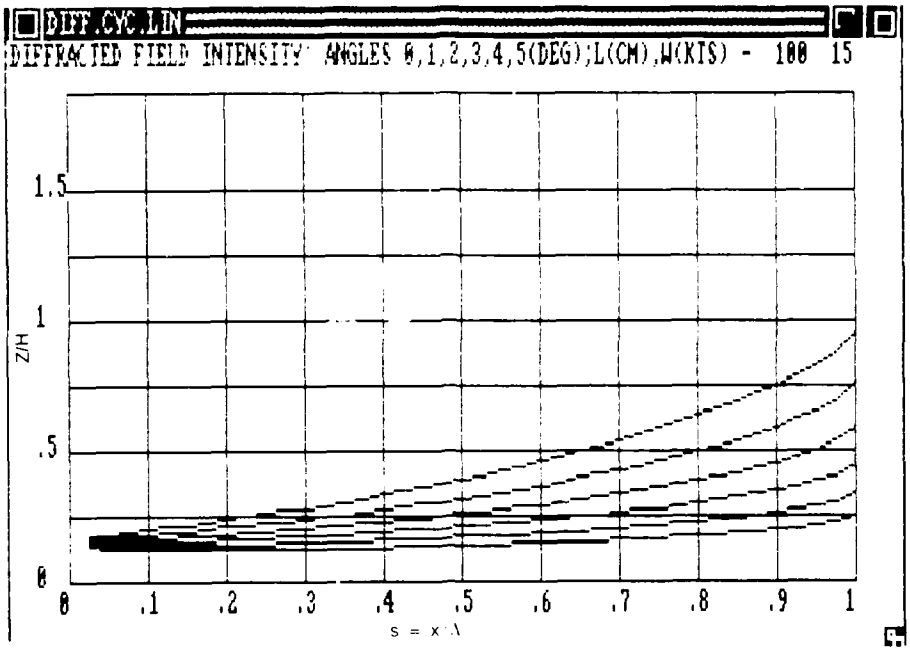


Fig. 4s — Diffraction Patterns for 1 - 100 cm wavelengths

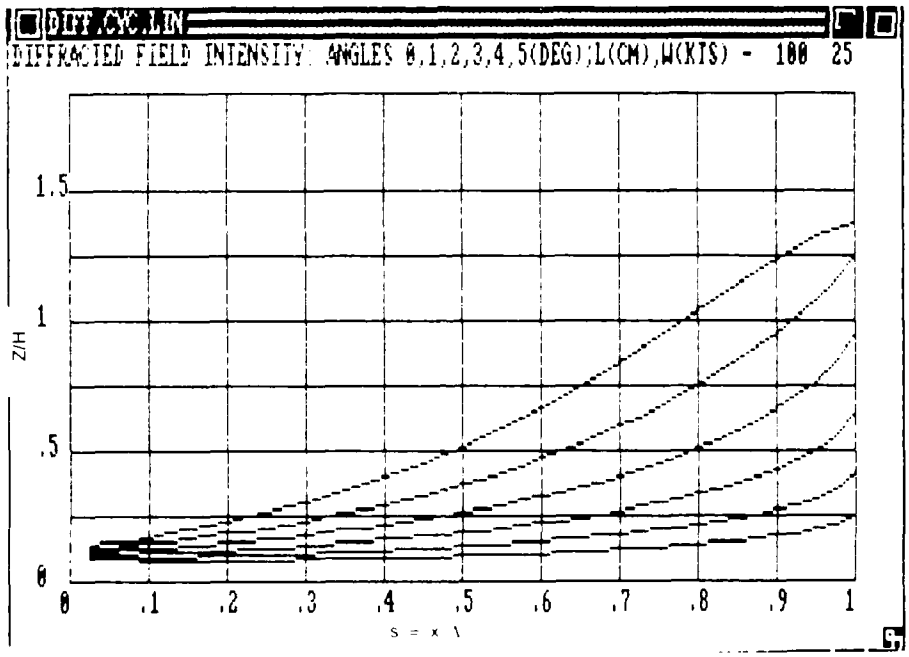


Fig. 4t — 0 - 5° grazing angles, 5 - 25 kt winds

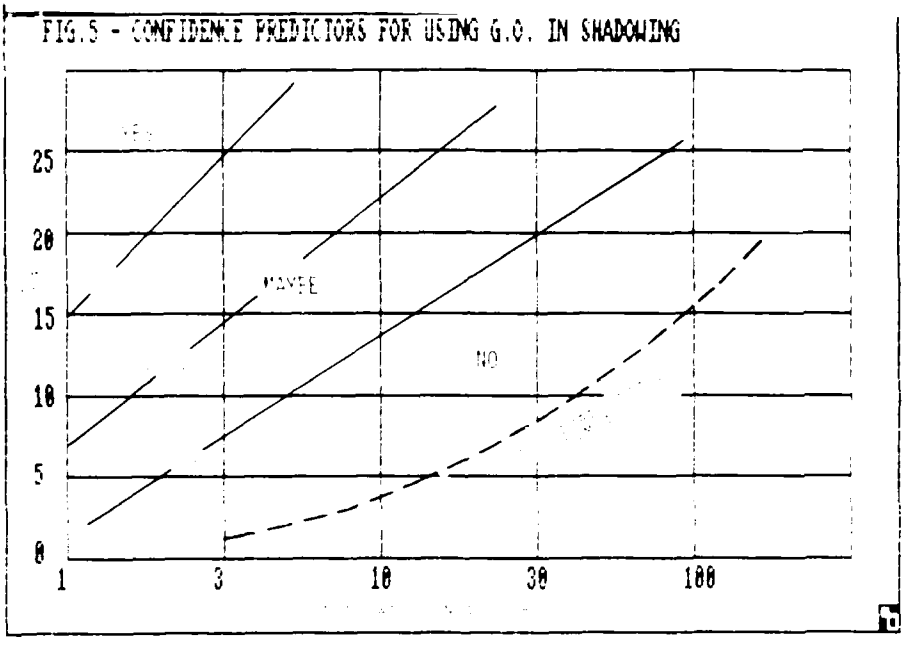


Fig. 5 — Confidence Predictors for Using Geometrical Optics

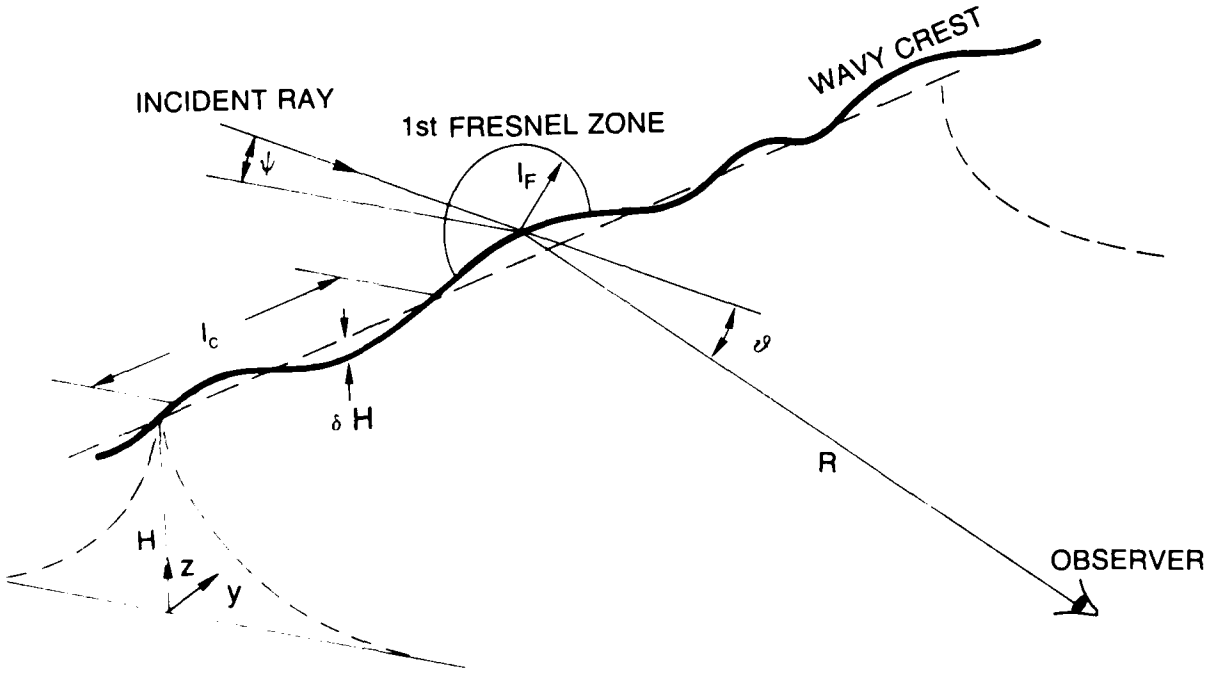


Fig. 6 — Diffraction with Crest-Height Variations

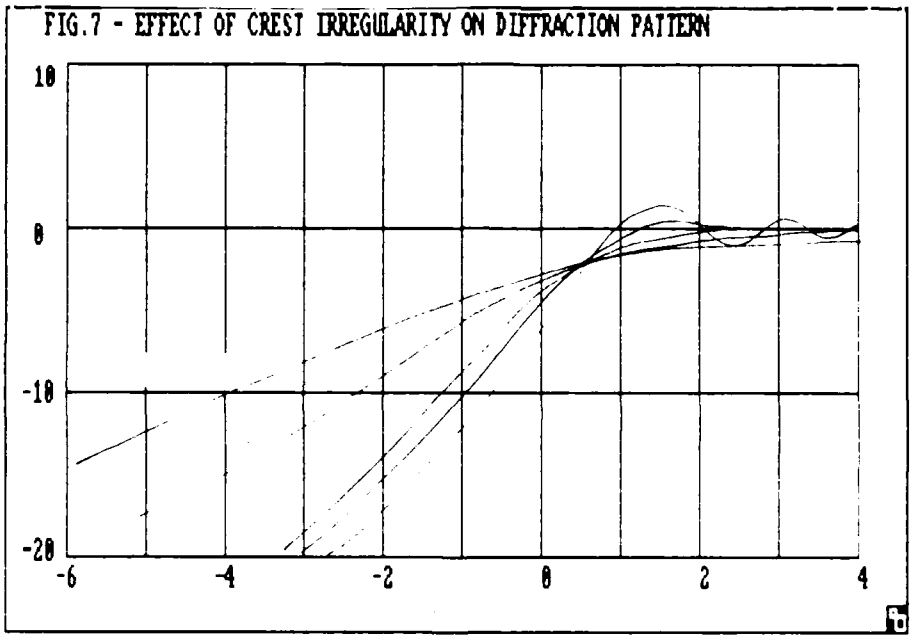


Fig. 7 — Effect of Crest Irregularity on Diffraction Pattern

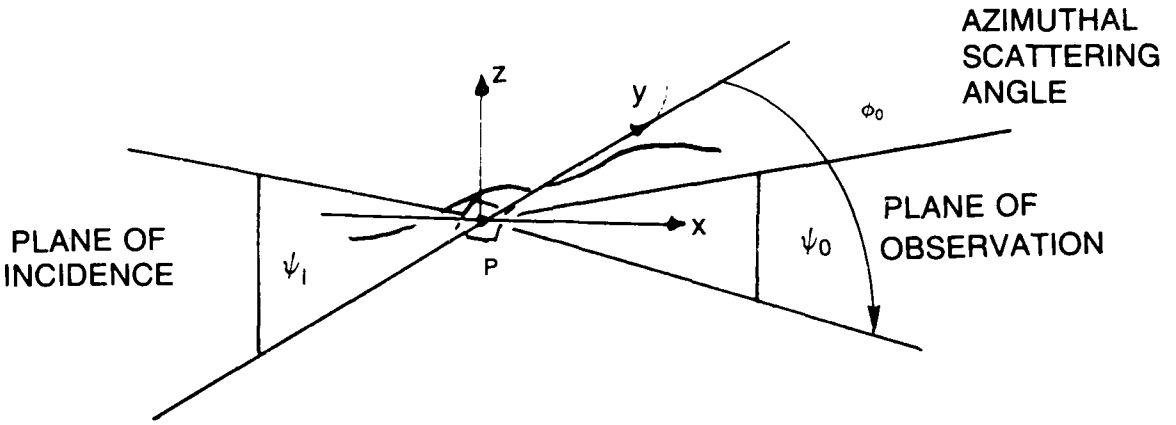


Fig. 8 — Bistatic Scattering Geometry

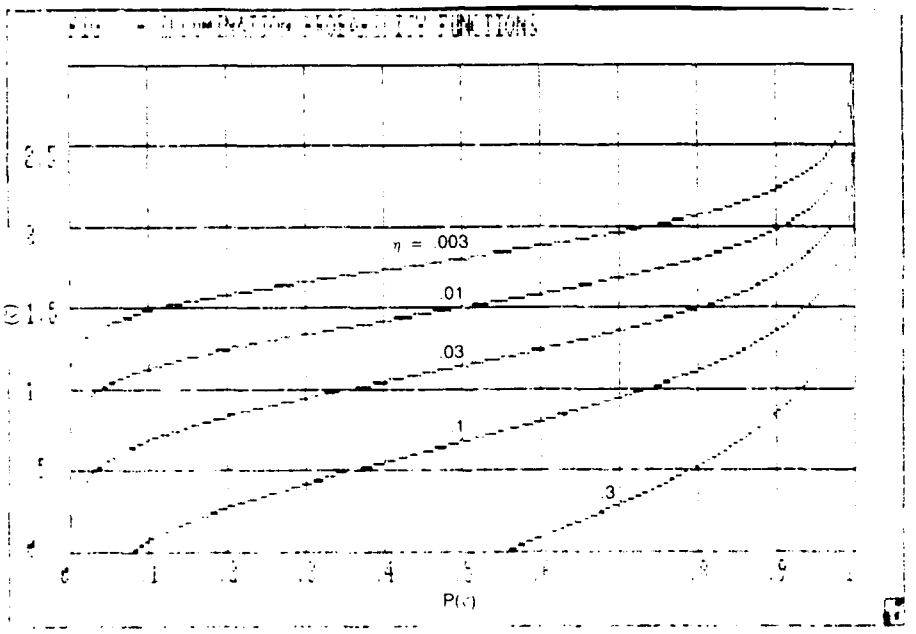


Fig. 9 — Illumination Probability Functions

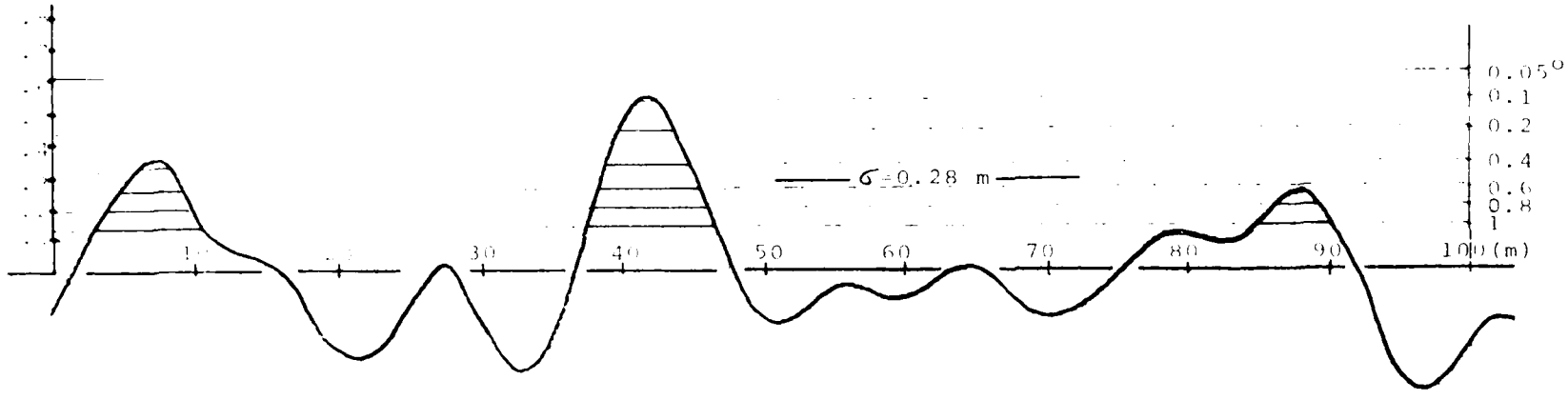


Fig. 10 — Threshold Levels vs. Grazing Angles for Simulated Sea

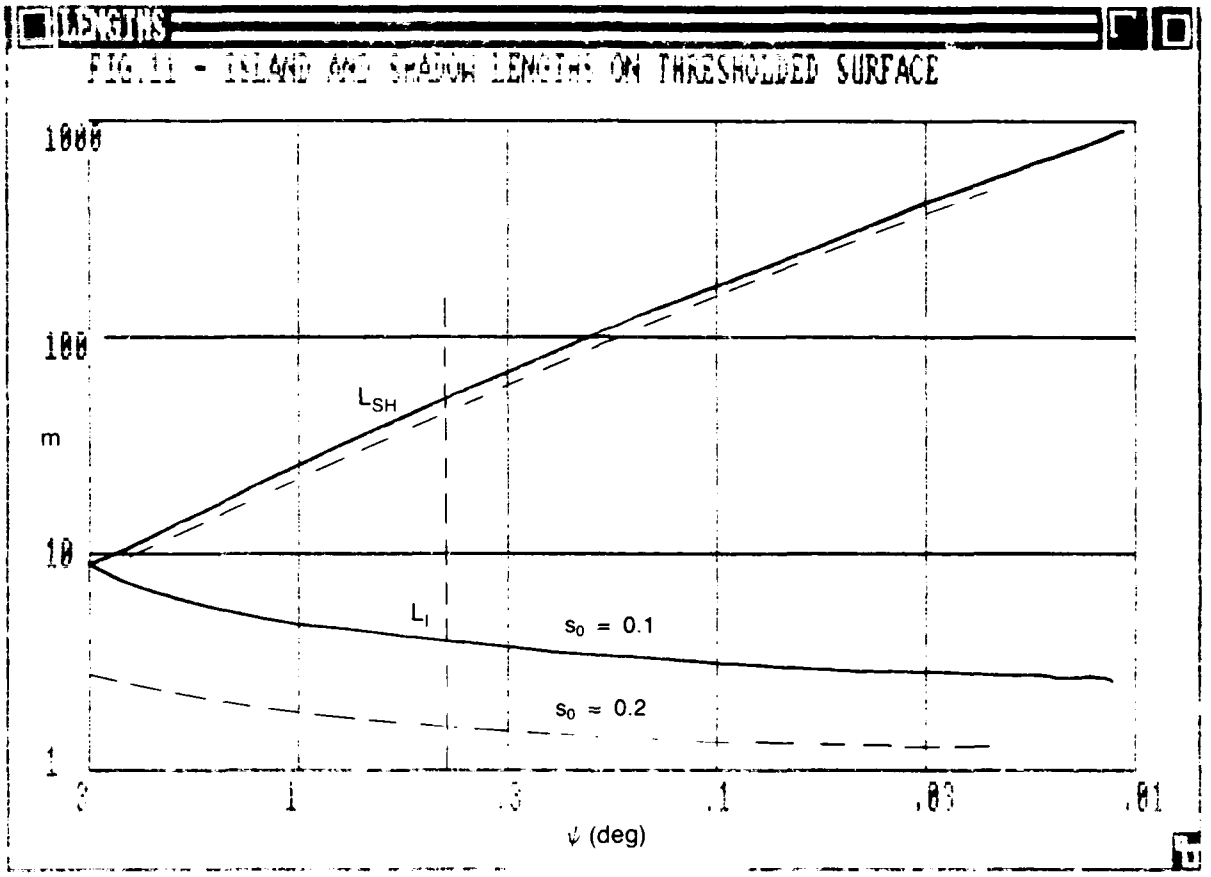


Fig. 11 — "Island" and "Shadow" Lengths on Thresholded Surface

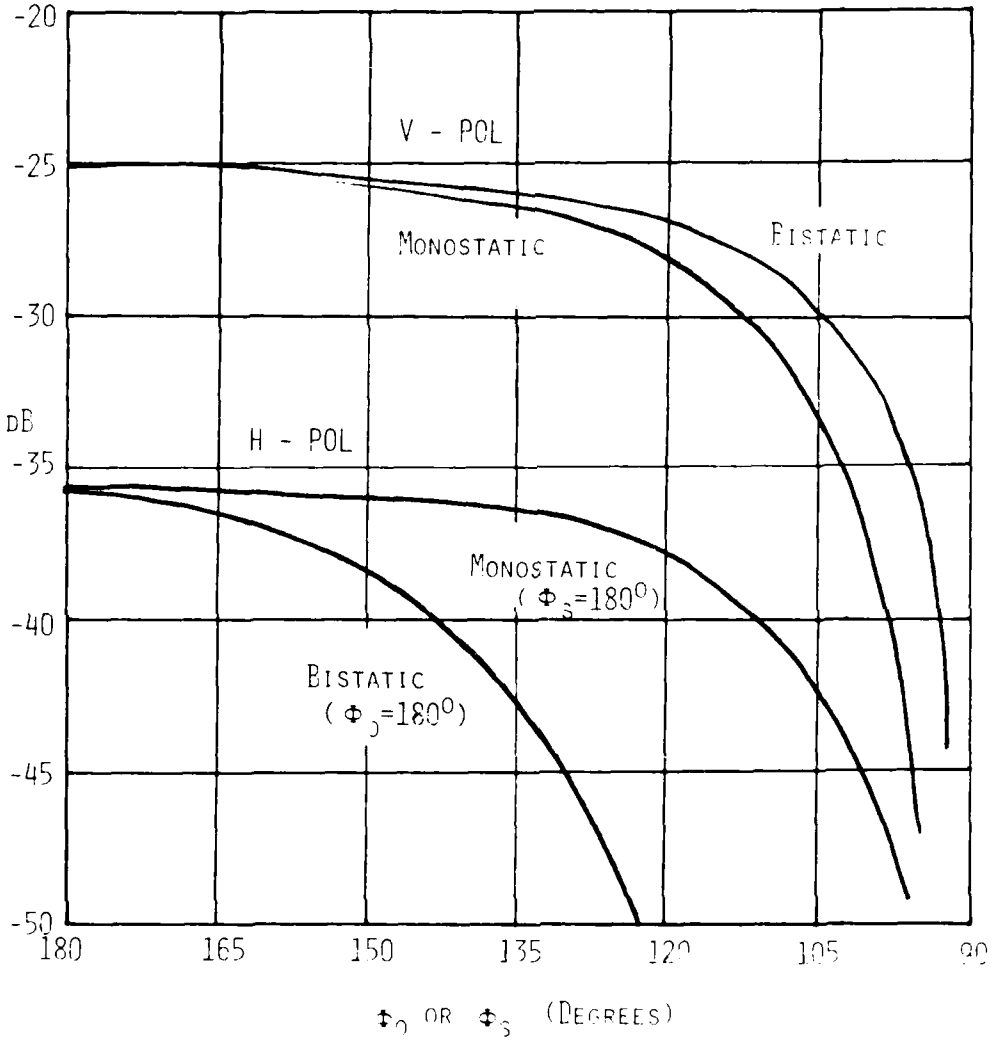


Fig. 12 — Angular Dependence of Wedge-Face Scatter - The Bragg Model

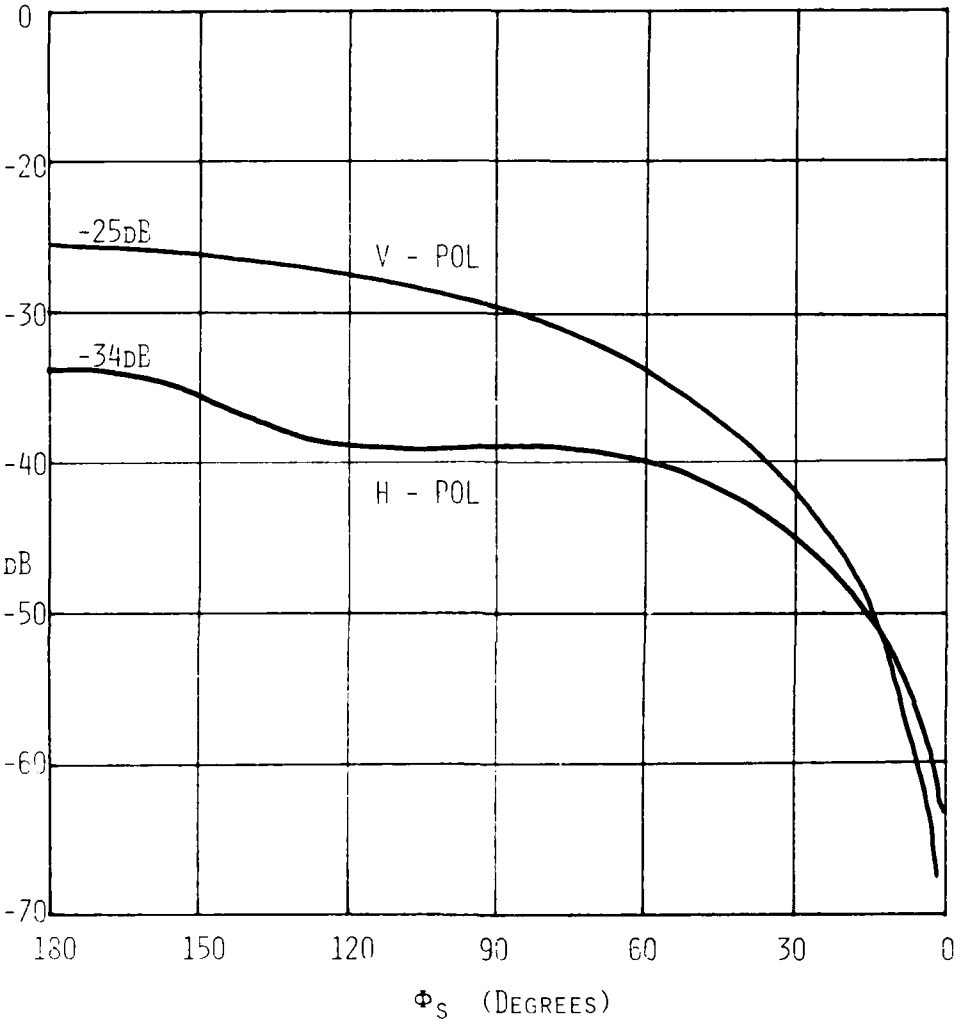


Fig. 13 — Bistatic Cross Sections for Uniform Crest Angle Distribution

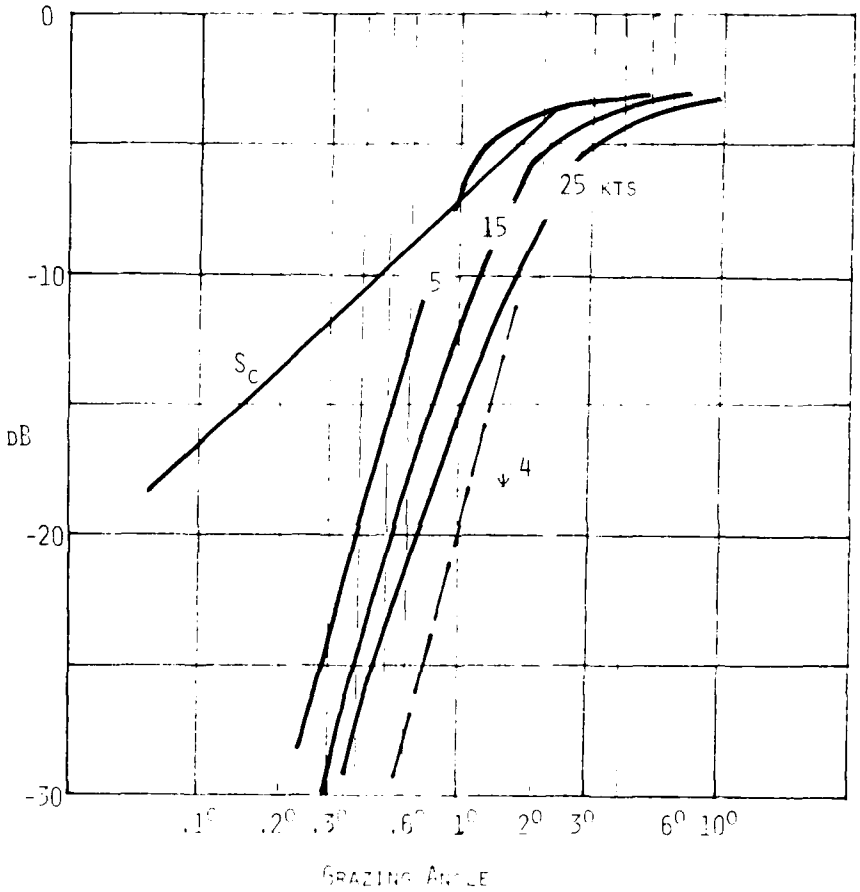


Fig. 14 — "Shadowing Functions" at Very Low Grazing Angles

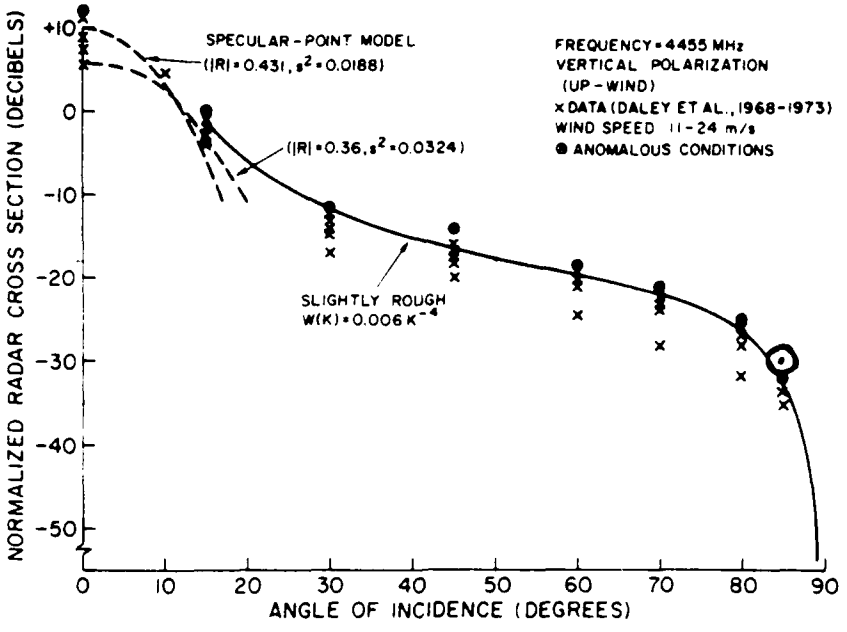


(a)

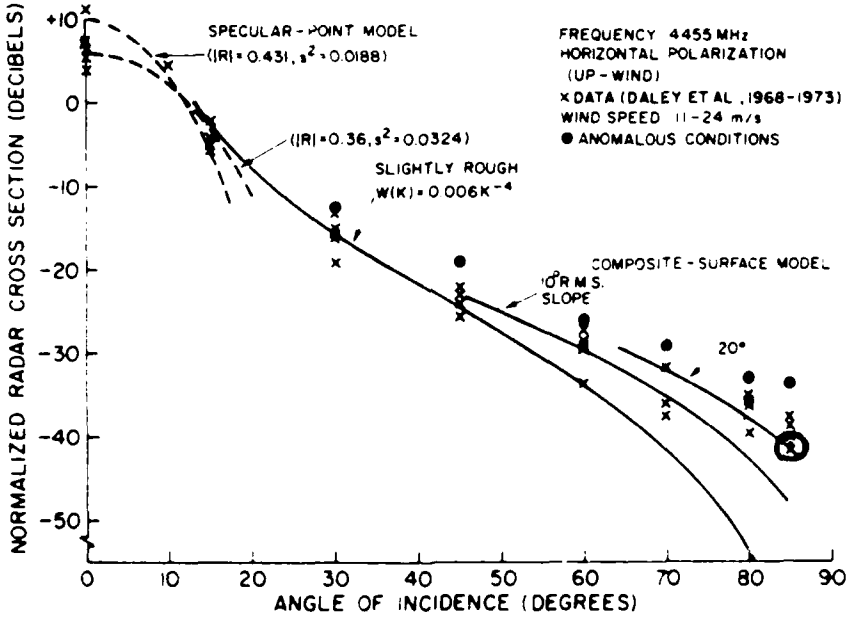


(b)

Fig. 15 — Comparison with NRL - 4FR Data

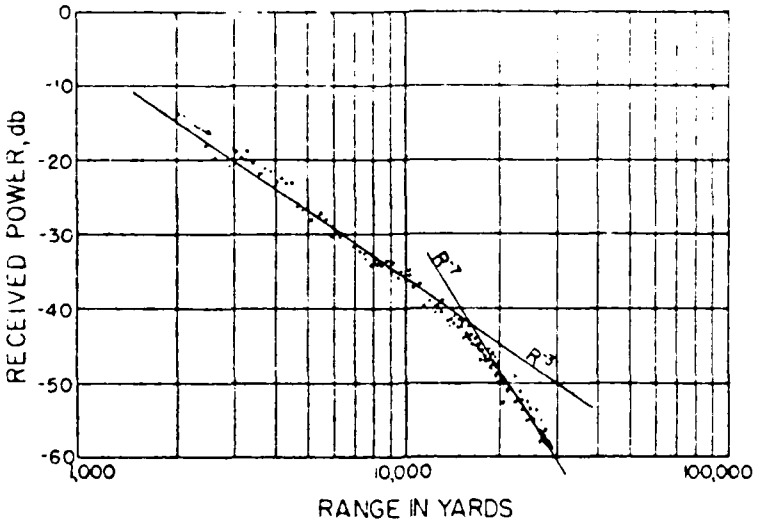


Fig. 16a — Evidence of a "Critical Angle"

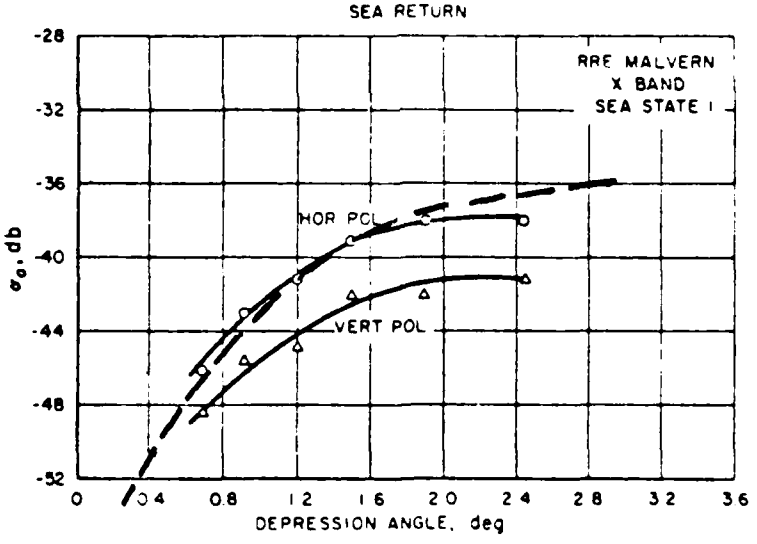


Fig. 16b — Polarization-Independent Low-Angle Behavior

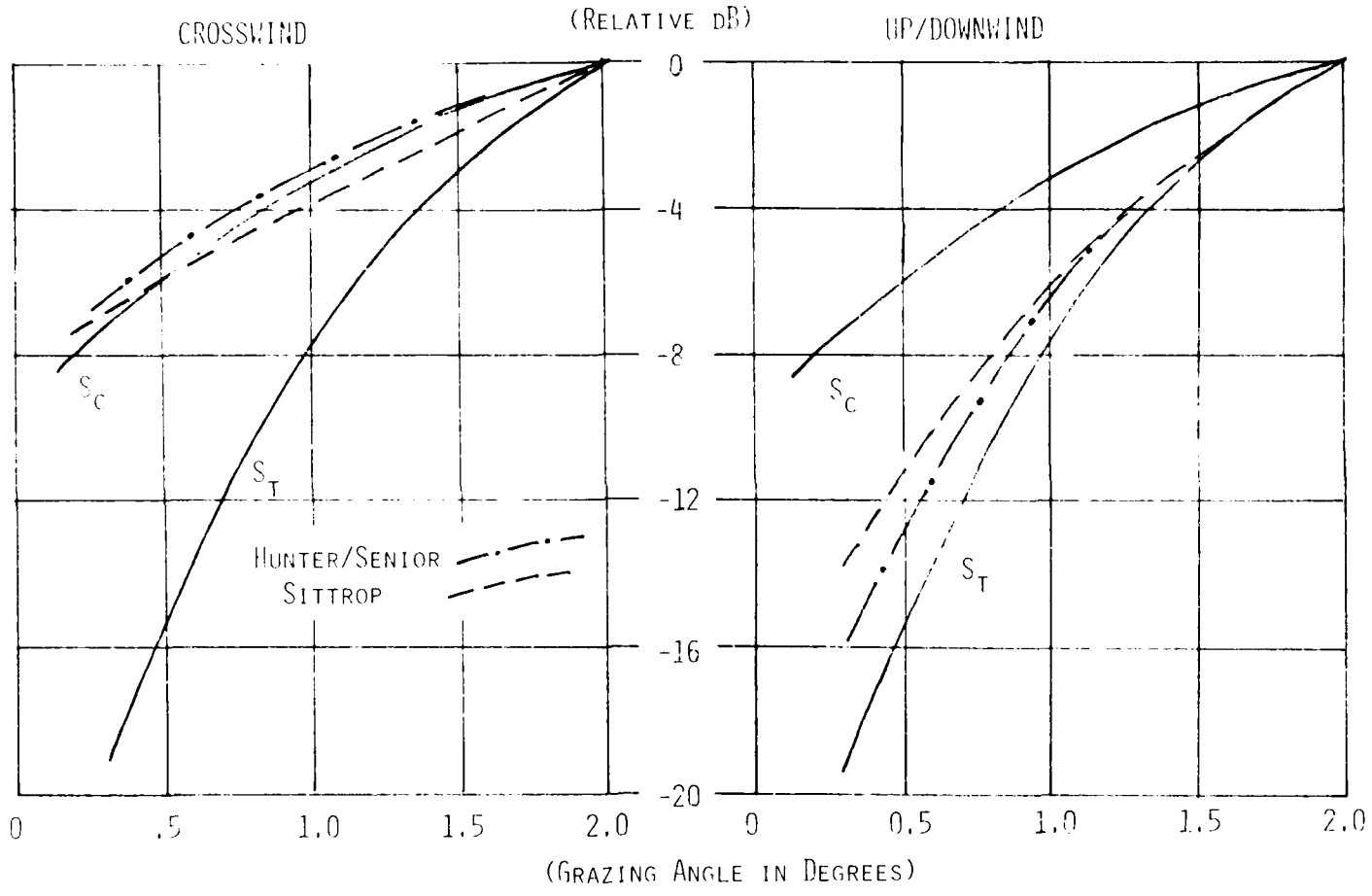


Fig. 17 — Comparison of Low Angle Backscatter with Shadowing Theories

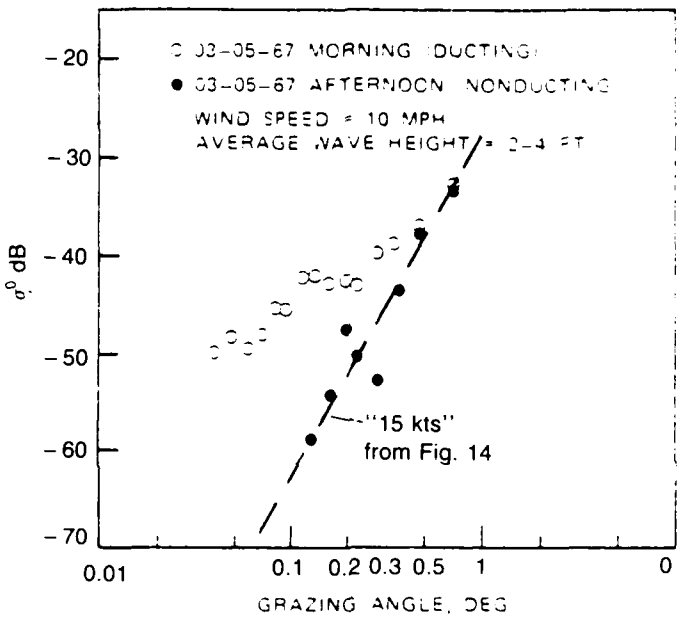


Fig. 18 — Example of Low-Angle Backscatter

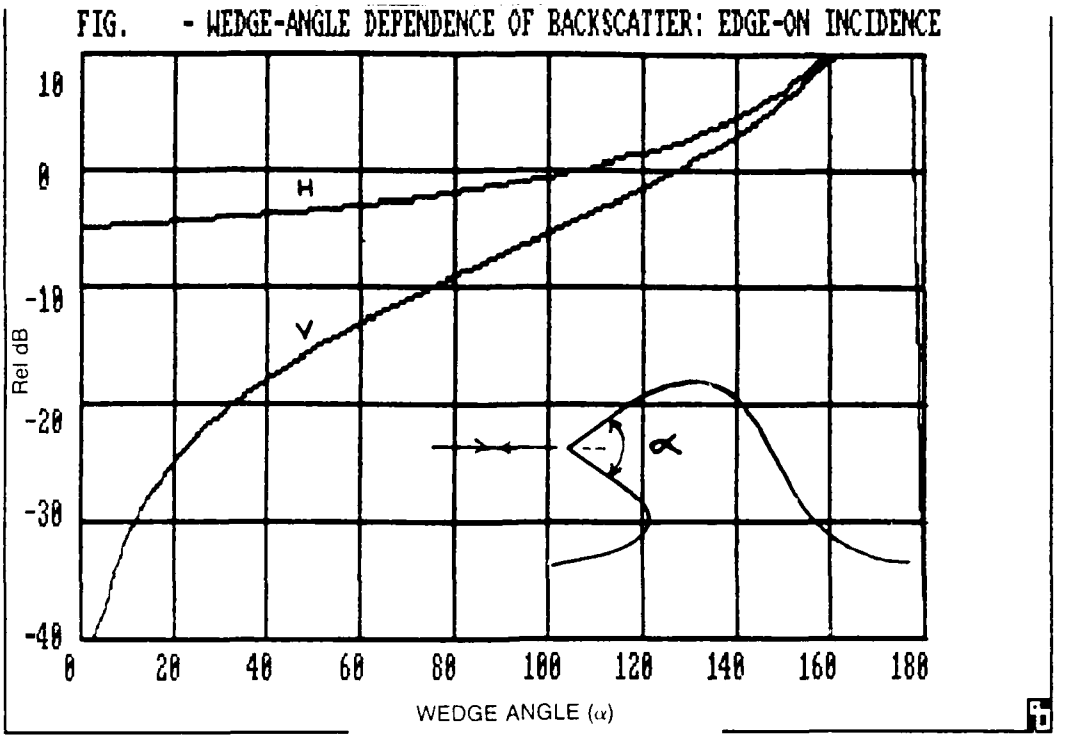


Fig. 19a — Wedge-Angle Dependence of Backscatter: Edge-On Incidence

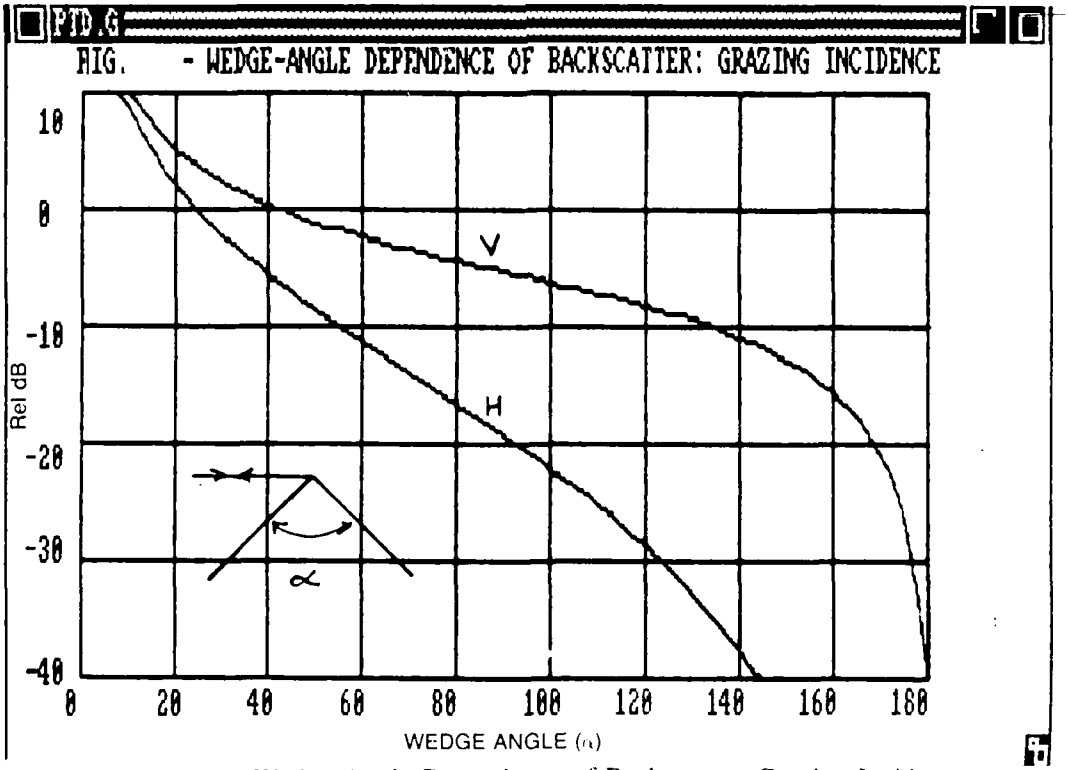


Fig. 19b — Wedge-Angle Dependence of Backscatter: Grazing Incidence

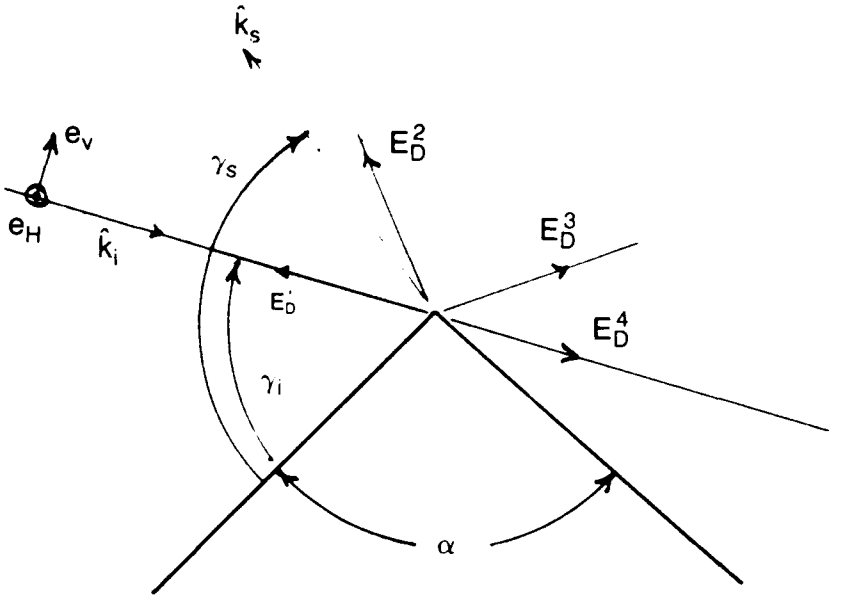


Fig. 20a — Geometry in the Geometrical Theory of Diffraction (2-D)

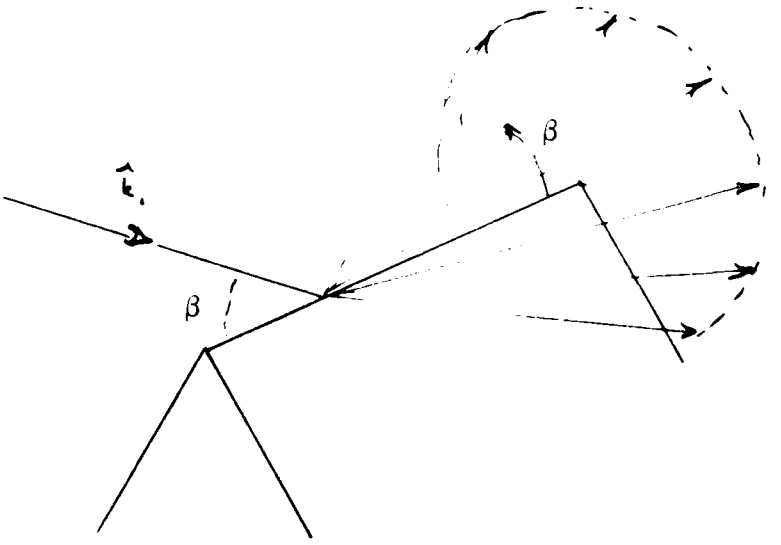


Fig. 20b — The Keller Cone

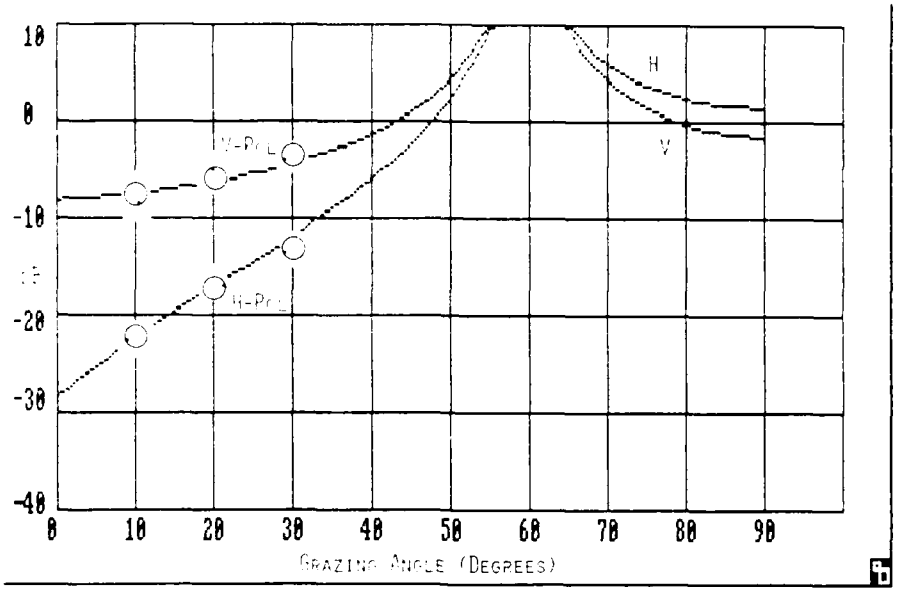


Fig. 21a — Backscatter Cross Section by the GTD (Wedge Angle = 120°)

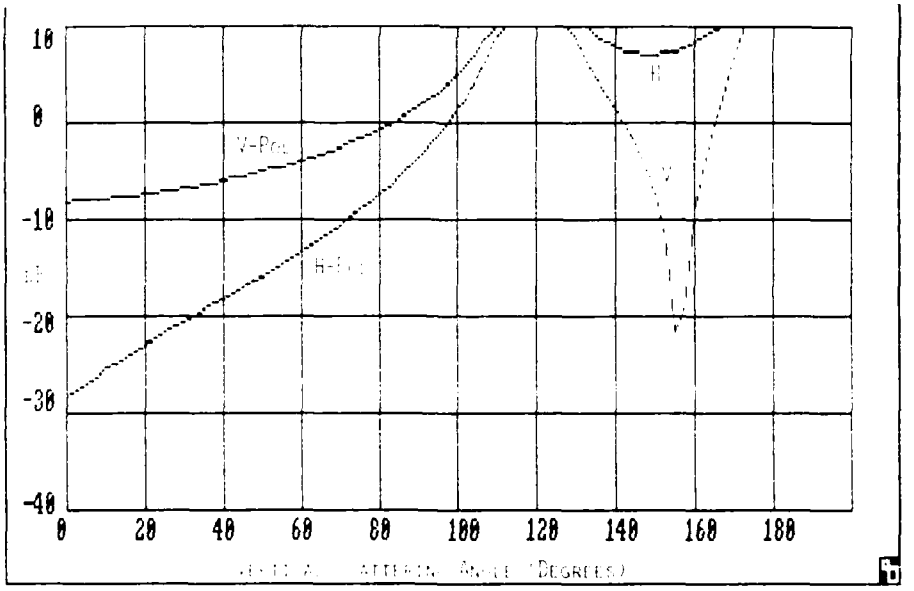


Fig. 21b — In-Plane Bistatic Cross Section by the GTD (120°)

Fig. 22 — Evidence of a "Microbreaker" in a Wave Tank. (Crapper, *"Capillary Waves."*)

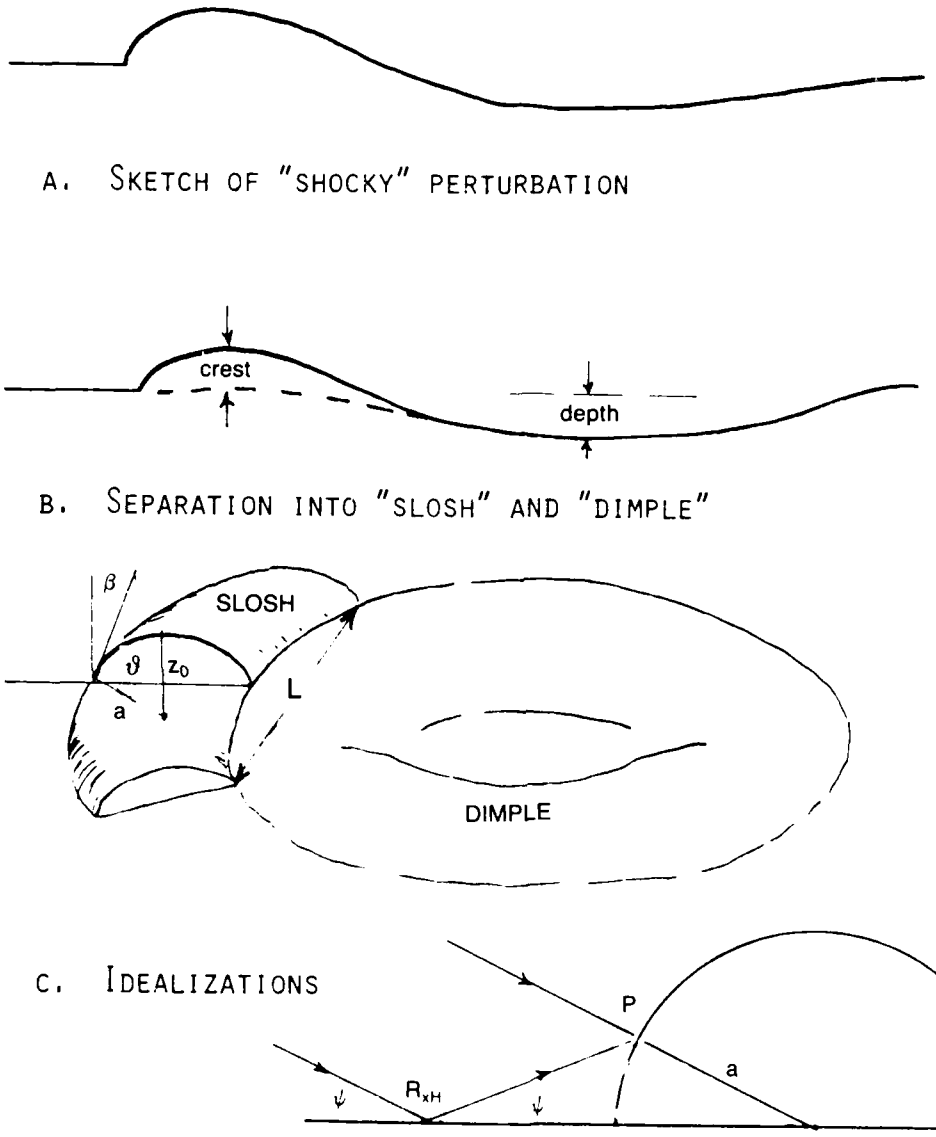


Fig. 23 — Modeling "Shocky" Surface Disturbances

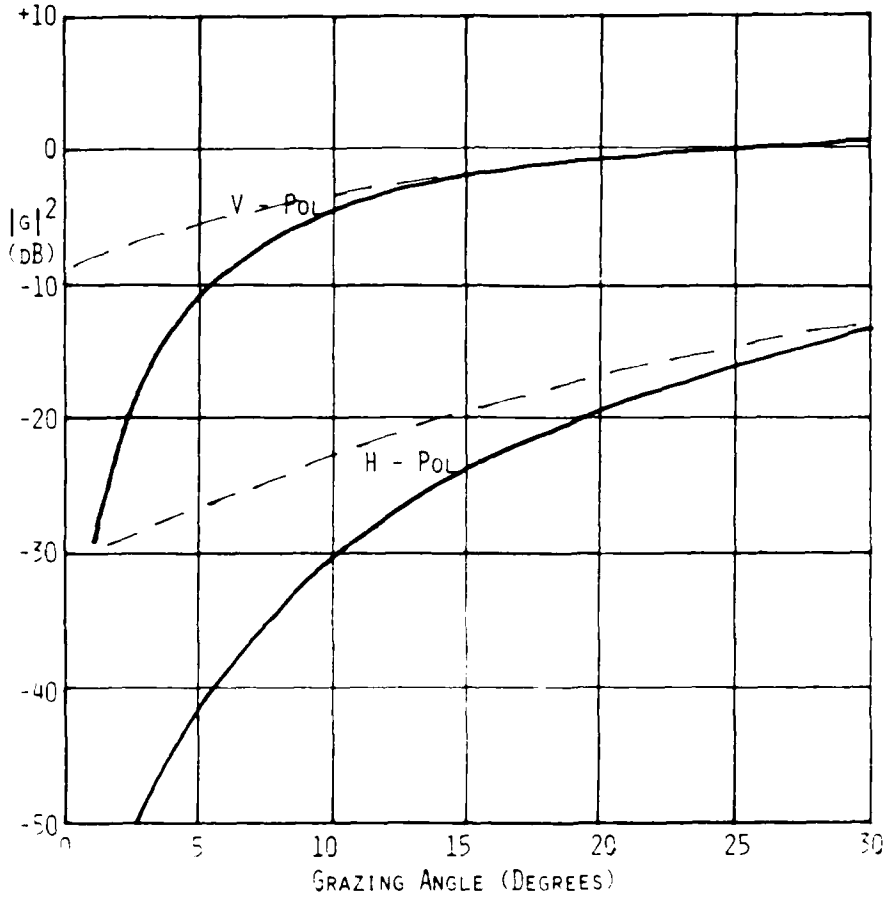


Fig. 24 — Angle Factors $|g_{V,H}|^2$ in Perturbation Theory

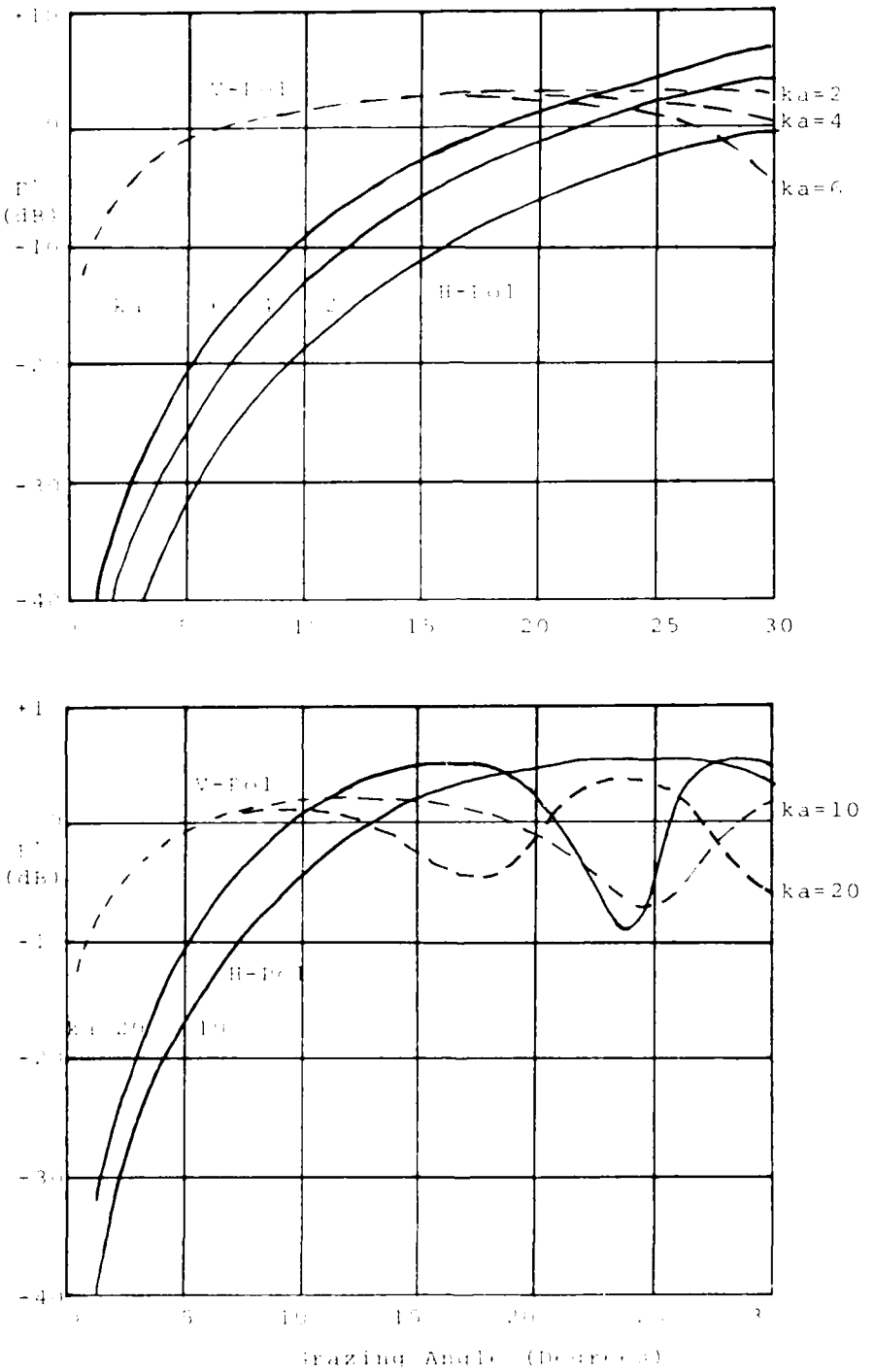


Fig. 25 — The Surface Proximity Factor $F_{V,H}^2$

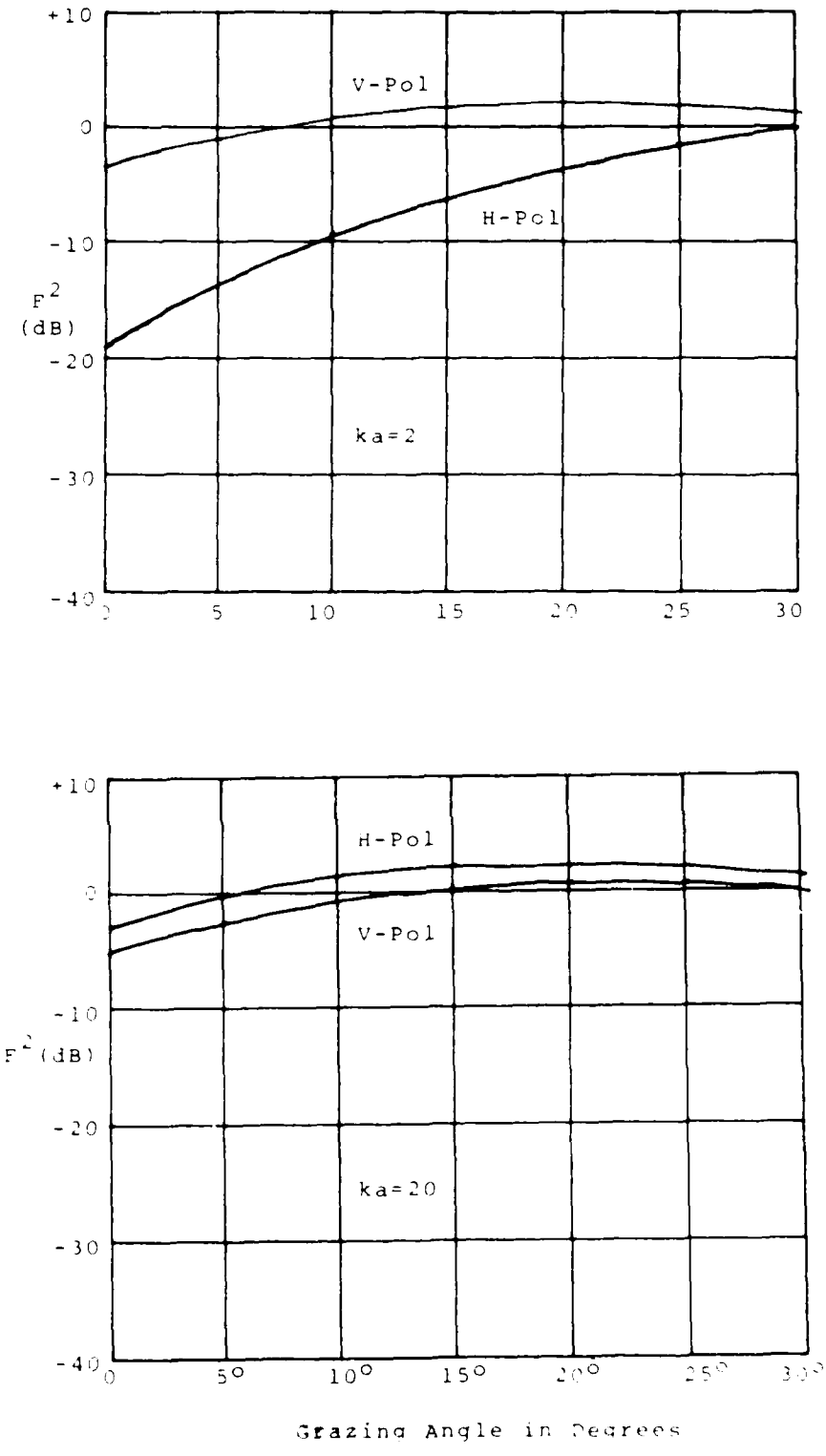


Fig. 26 — The Surface Proximity Factor with 15 kt Wind (rms slope = .15)

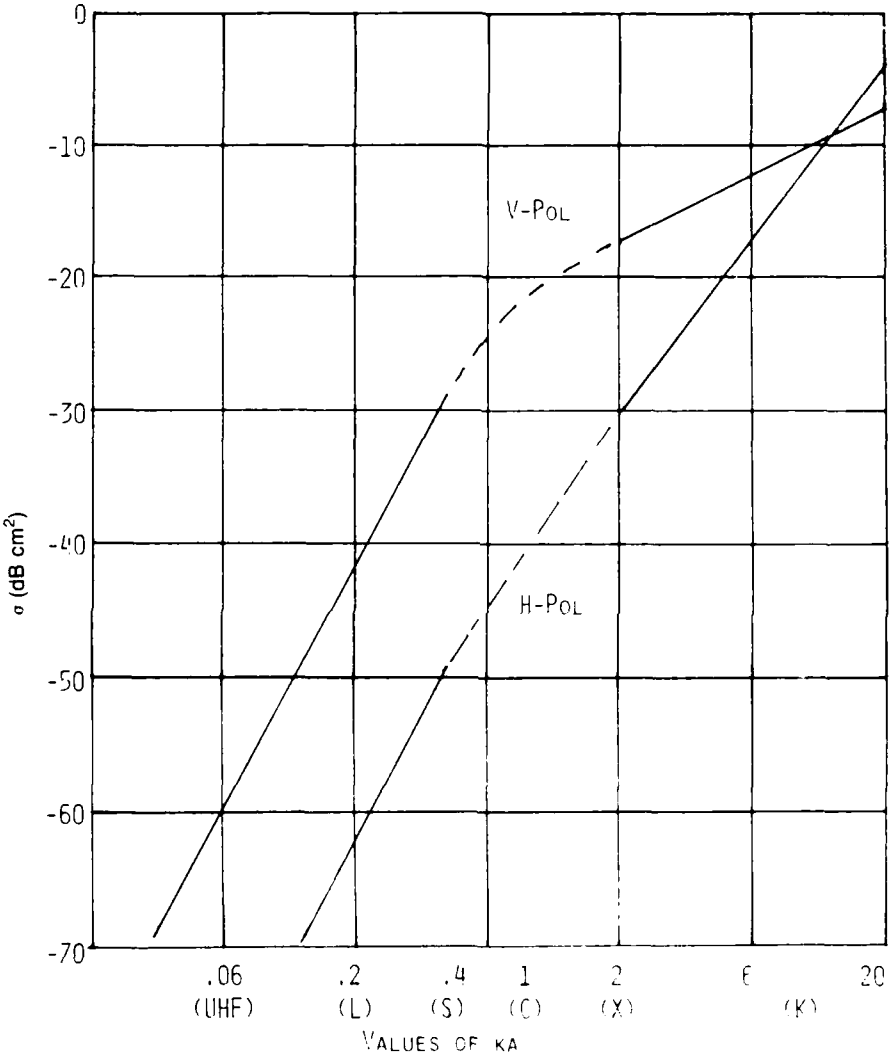


Fig. 27 — Low-Angle "Slosh" Cross Sections (1 by 20 cm, 15 kt wind)

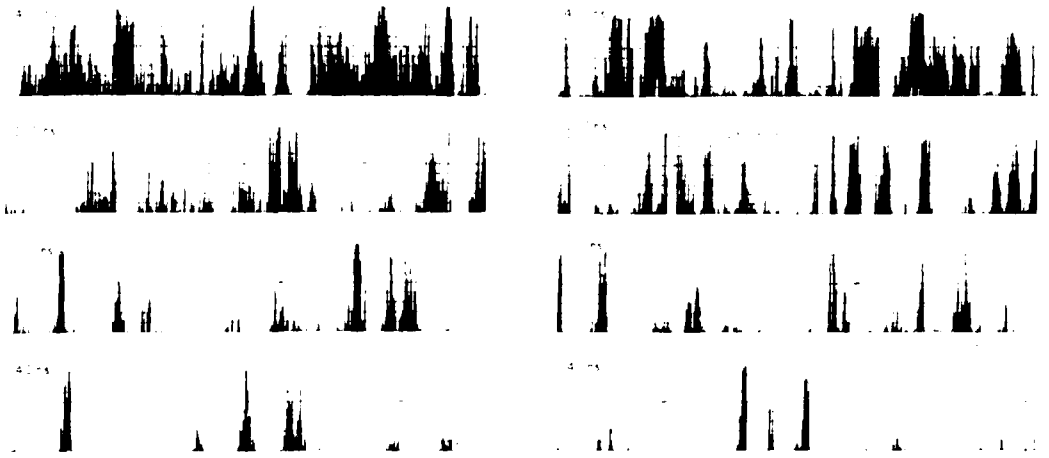

"Windblown Sea With Many Whitecaps"

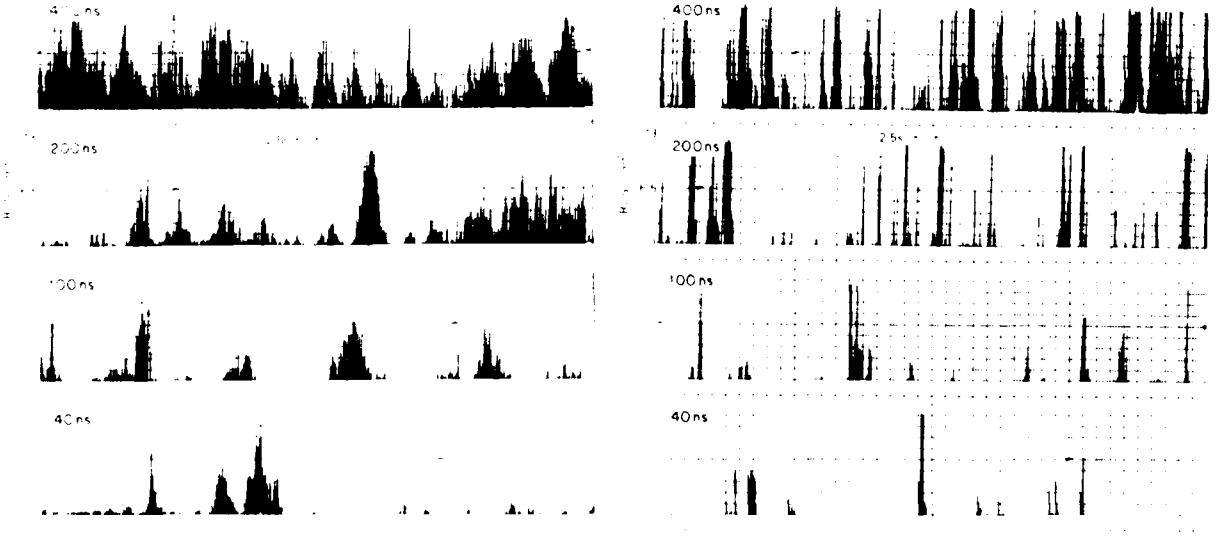


"Calm Sea"

Fig. 28 – Low Angle Backscatter Displaying "Sea Spikes". (Lewis and Olin, 1980.)

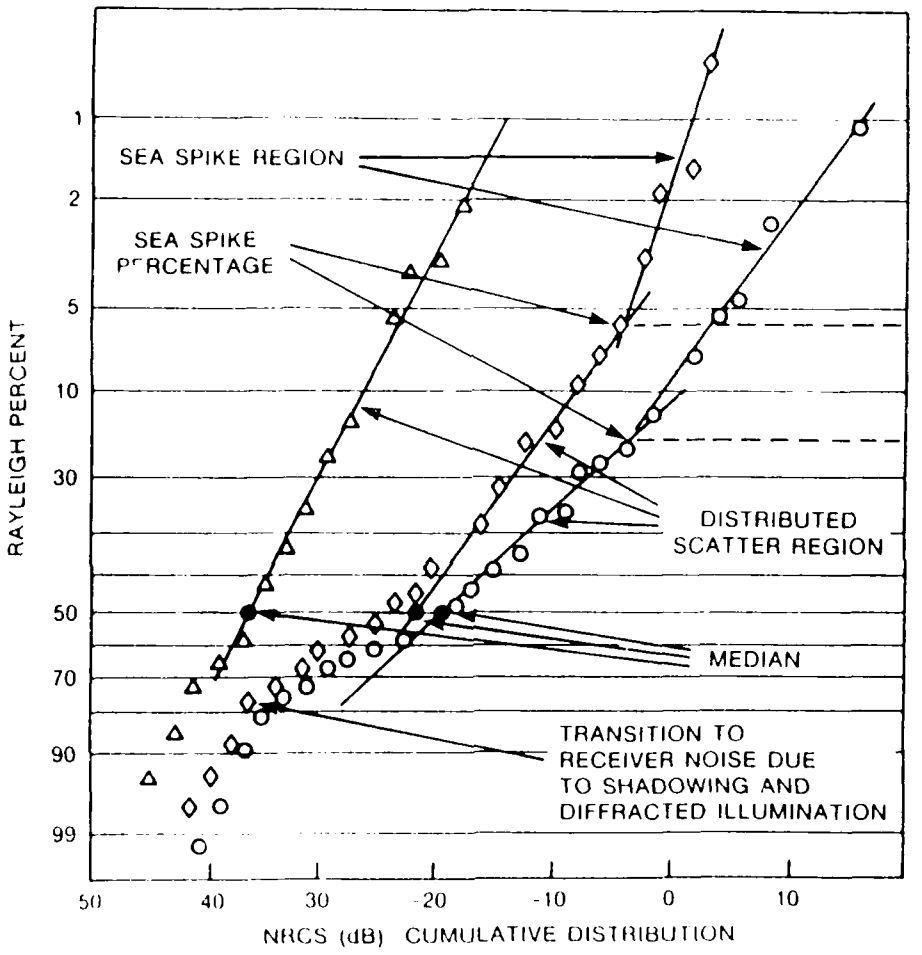


Fig. 29 — Cumulative NRCS Distributions vs Wind Strength (Trizna,1987)

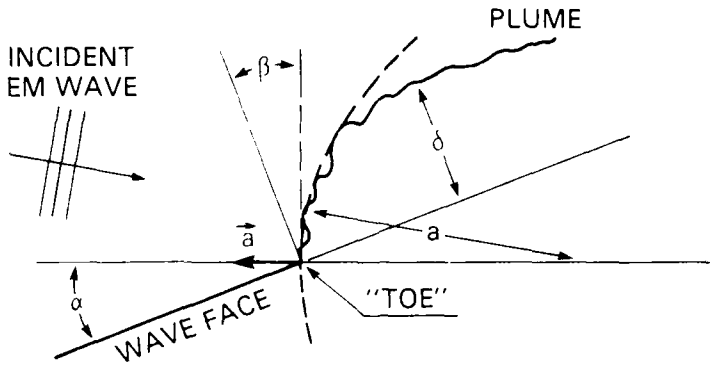


Fig. 30a — Sketch of "Plume" Geometry (Wetzel, 1986)

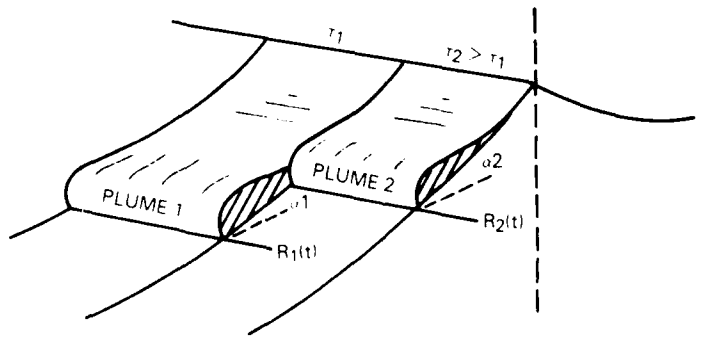


Fig. 30b — Idealized Plumes on a Breaking Wave Face (Wetzel, 1986)

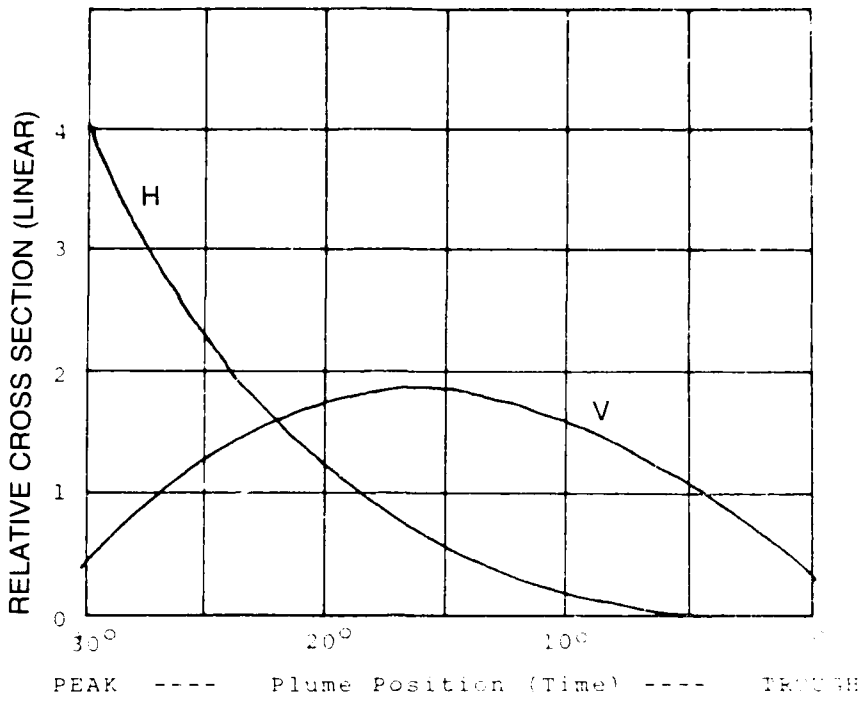


Fig. 31a — Temporal Behavior of V and H-Pol Cross Sections (ka=6)

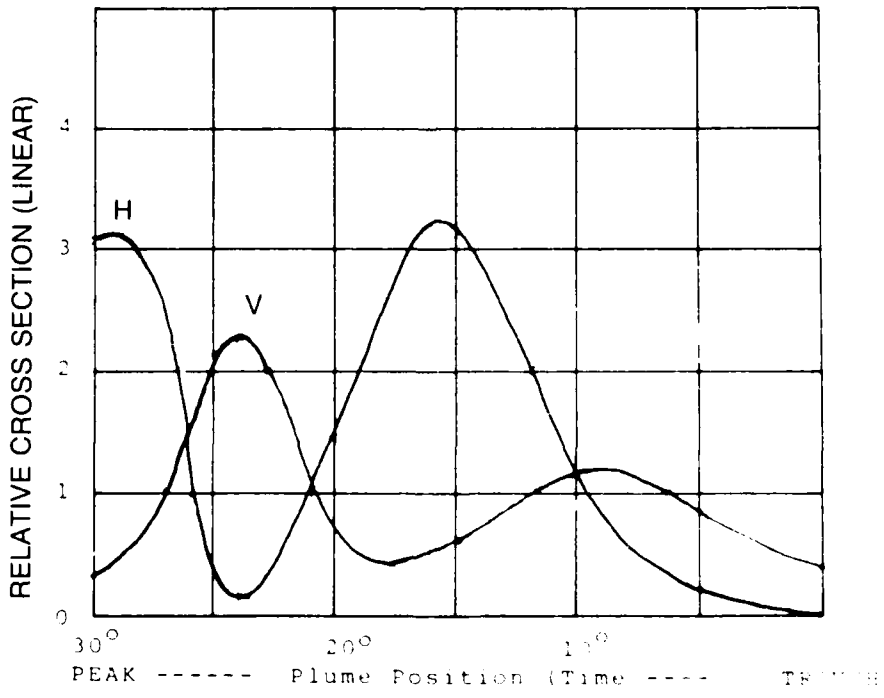


Fig. 31b — Temporal Behavior of V and H-Pol Cross Sections (ka=20)

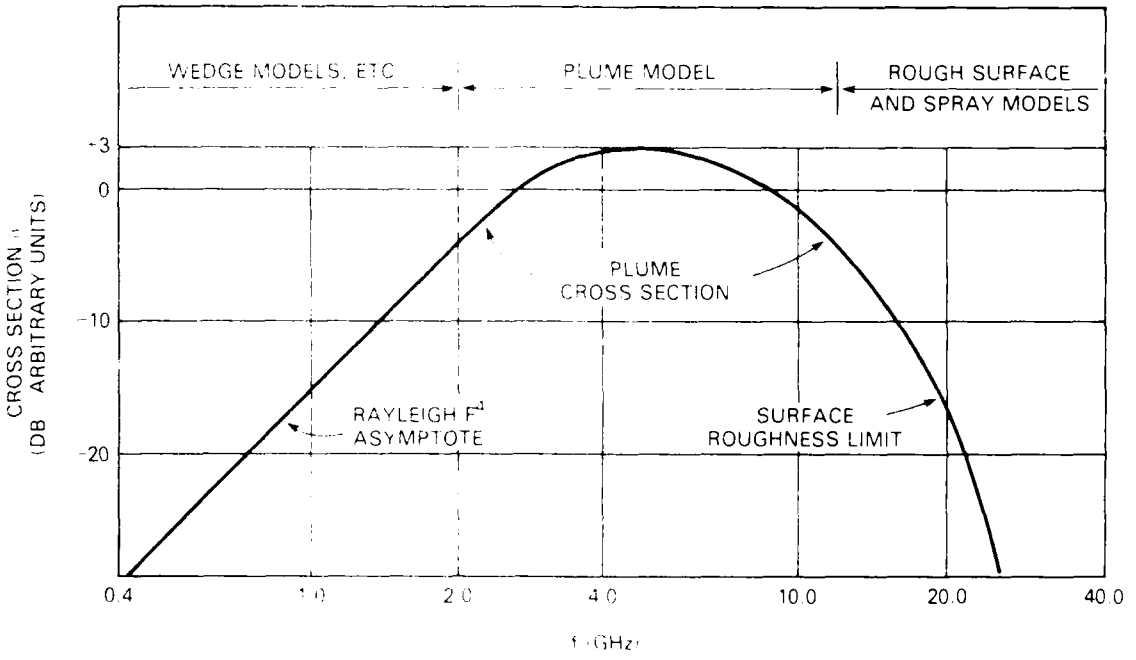


Fig. 32 — Possible Breaker Scattering Mechanisms over the Microwave Spectrum (Wetzel, 1986)